UNIVERSITY OF ROCHESTER
LABORATORY FOR LASER ENERGETICS

Volume 129
October–December 2011
DOE/NA/28302-1046

LLE Review

Quarterly Report

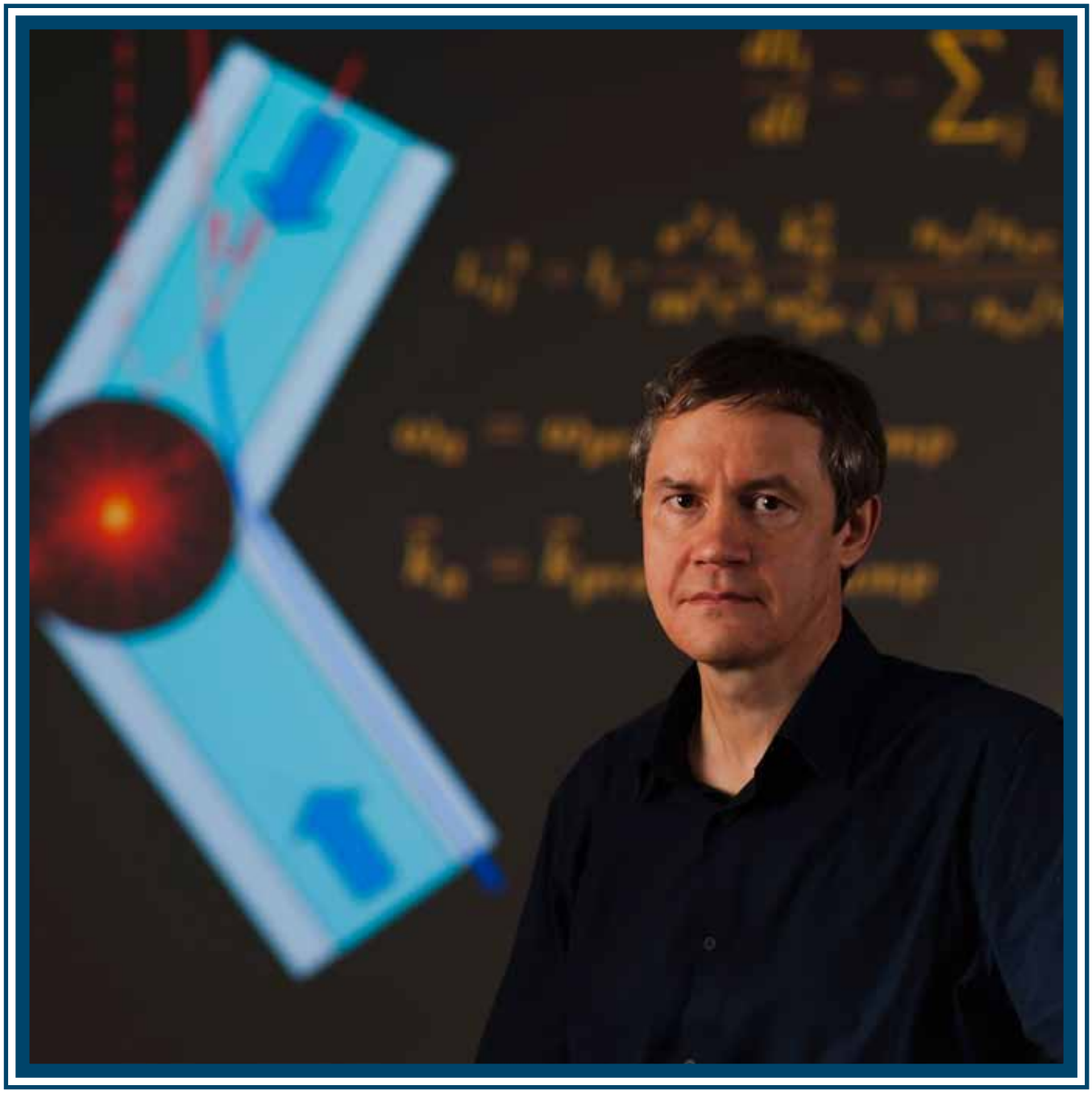

About the Cover:

The cover photo highlights scientist Dr. Igor Igumenshchev presenting his results on the effects of crossed-beam energy transfer (CBET) in directly driven implosions. In the background is a schematic illustration detailing the physics and main equations underlying the CBET process. This process causes the transfer of energy from incoming laser light rays to outgoing rays and results in a reduction of laser coupling and hydrodynamic efficiency during the implosion. Simulations using the CBET model reproduce the reflected light and bang times of a variety of implosion experiments performed on OMEGA. Controlling the effects of CBET in direct-drive implosions is an important consideration for achieving ignition on the National Ignition Facility.

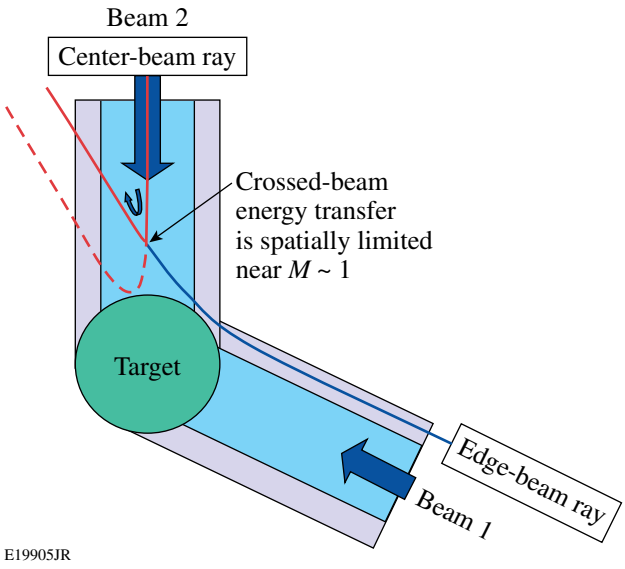

The figure on the left illustrates the CBET process. An incident ray (shown in blue) at the edge of Beam 1 is refracted outward from above the critical radius. As it proceeds away from the target, this ray interacts through a low-gain stimulated Brillouin scattering process with an incoming ray. This process peaks at the high-intensity center of Beam 2 (shown in red) resulting in the transfer of some Beam 2 energy to the outgoing ray. As a result, rays in the center of Beam 2 deliver less energy to the target, reducing the overall laser absorption.

The work described in this volume includes current research at the Laboratory for Laser Energetics, which is supported by New York State Energy Research and Development Authority, the University of Rochester, the U.S. Department of Energy Office of Inertial Confinement Fusion under Cooperative Agreement No. DE-FC52-08NA28302, and other agencies.

Printed in the United States of America
Available from
National Technical Information Services
U.S. Department of Commerce
5285 Port Royal Road
Springfield, VA 22161
www.ntis.gov

For questions or comments, contact Alex Shvydky, Editor
Laboratory for Laser Energetics
250 East River Road
Rochester, NY 14623-1299
(585) 275-9539
www.lle.rochester.edu

UNIVERSITY OF ROCHESTER
LABORATORY FOR LASER ENERGETICS

Volume 129
October–December 2011
DOE/NA/28302-1046

LLE Review

Quarterly Report

UR LLE

Contents

In Brief

This volume of LLE Review, covering October–December 2011, features "Crossed-Beam Energy Transfer in Direct-Drive Implosions" by I. V. Igumenshchev, W. Seka, D. H. Edgell, D. T. Michel, D. H. Froula, R. S. Craxton, R. Follett, J. H. Kelly, T. Z. Kosc, J. F. Myatt, T. C. Sangster, A. Shvydky, S. Skupsky, and C. Stoeckl (LLE); V. N. Goncharov and A. V. Maximov (LLE and Department of Mechanical Engineering, U. of Rochester); L. Divol and P. Michel (LLNL); and R. L. McCrory and D. D. Meyerhofer (LLE and Departments of Mechanical Engineering and Physics, U. of Rochester). In this article (p. 1), direct-drive–implosion experiments on the OMEGA laser [T. R. Boehly *et al.*, Opt. Commun. **133**, 495 (1995)] have shown discrepancies between simulations of the scattered (non-absorbed) light levels and measured ones that indicates the presence of a mechanism that reduces laser coupling efficiency by 10% to 20%. The authors attribute this degradation in laser coupling to crossed-beam energy transfer (CBET)—which is electromagnetically seeded—low-gain stimulated Brillouin scattering. CBET scatters energy from the central portion of the incoming light beam to outgoing light, reducing the laser absorption and hydrodynamic efficiency of implosions. One-dimensional hydrodynamic simulations including CBET show good agreement with all observables in implosion experiments on OMEGA. Three strategies to mitigate CBET and improve laser coupling are considered: the use of narrow beams, multicolor lasers, and higher-Z ablators. Experiments on OMEGA using narrow beams have demonstrated improvements in implosion performance.

Additional highlights of research presented in this issue include the following:

- P. M. Nilson and A. A. Solodov (FSC and LLE); J. R. Davies, R. Betti, and D. D. Meyerhofer (FSC, LLE, and Departments of Mechanical Engineering and Physics, U. of Rochester); and W. Theobald, P. A. Jaanimagi, C. Mileham, R. K. Jungquist, C. Stoeckl, I. A. Begishev, J. F. Myatt, J. D. Zuegel, and T. C. Sangster (LLE) use time-resolved K_α spectroscopy to infer the hot-electron equilibration dynamics in high-intensity laser interactions with picosecond pulses and thin-foil solid targets (p. 15). The measured K_α-emission pulse width increases from ~3 to 6 ps for laser intensities from ~10^{18} to 10^{19} W/cm^2. Collisional energy-transfer model calculations suggest that hot electrons with mean energies from ~0.8 to 2 MeV are contained inside the target. The inferred mean hot-electron energies are broadly consistent with ponderomotive scaling over the relevant intensity range

- D. H. Froula, B. Yaakobi, D. T. Michel, S. X. Hu, J. F. Myatt, A. A. Solodov, R. S. Craxton, C. Stoeckl, W. Seka, and R. W. Short measure the hot-electron generation by the two-plasmon-decay (TPD) instability in plasmas relevant to direct-drive inertial confinement fusion. Density scale lengths of 400 μm at $n_{cr} = 4$ in planar CH targets allows the TPD instability to be driven to saturation for vacuum intensities above ~3.5×10^{14} W/cm^2 (p. 20). In the saturated regime, ~1% of the laser energy is converted to hot electrons. The hot-electron temperature is measured to increase rapidly from 25 to 90 keV as the laser beam intensity is increased from 2 to 7×10^{14} W/cm^2. This increase in the hot-electron temperature is compared with predictions from nonlinear Zakharov models.

- J. Bromage, C. Dorrer, M. Millecchia, J. Bunkenburg, R. Jungquist, and J. D. Zuegel present a design of an ultra-intense optical parametric chirped-pulse–amplification (OPCPA) system at 910 nm (p. 30). Technologies are being developed for large-scale systems based on deuterated potassium dihydrogen phosphate (DKDP) optical parametric amplifiers that could be pumped by kilojoule-class Nd:glass lasers such as OMEGA EP. Results from a prototype white-light–seeded chain of noncollinear optical parametric amplifiers (NOPA's) are reviewed. The development of a cylindrical Öffner stretcher that has advantages over standard stretchers for ultra-intense, high-contrast systems is described. The

front-end development will culminate in demonstrating a mid-scale optical parametric amplifier line (OPAL) that will use scalable technologies to produce 7.5-J, 15-fs pulses with a temporal contrast exceeding 10^{10}.

- C. Stoeckl, G. Fiksel, D. Guy, C. Mileham, P. M. Nilson, T. C. Sangster, M. J. Shoup III, and W. Theobald designed a narrowband x-ray imager for a Cu K_α line at ~8 keV using a spherically bent quartz crystal and implemented it on the OMEGA EP laser (p. 34). The quartz crystal is cut along the 2131 (211) planes for a 2*d* spacing of 0.3082 nm, resulting in a Bragg angle of 88.7°, very close to normal incidence. An optical system is used to remotely align the spherical crystal without breaking the vacuum of the target chamber. The images show a high signal-to-background ratio of typically >100:1 with laser energies ≥1 kJ at a 10-ps pulse duration and a spatial resolution of less than 10 μm.

- J. Kitaygorsky (Kavli Institute of Nanoscience Delft, Delft University of Technology, The Netherlands, Department of Electrical and Computer Engineering, U. of Rochester, and LLE); W. Słysz (Institute of Electron Technology, Poland); R. Shouten, S. Dorenbos, E. Reiger, and V. Zwiller (Kavli Institute of Nanoscience Delft, Delft University of Technology, The Netherlands); and R. Sobolewski (Department of Electrical and Computer Engineering, U. of Rochester, LLE, and Institute of Electron Technology, Poland) propose a new operation regime of NbN superconducting single-photon detectors (SSPD's) by integrating them with a low-noise cryogenic high-electron-mobility transistor and a high-load resistor (p. 39). The proposed SSPD operating scheme makes it possible to distinguish dark pulses from actual photon pulses in SSPD's and therefore gain a better understanding of the origin of dark counts generated by the detector. A statistical analysis of amplitude distributions of recorded trains of the SSPD photoresponse transients is used to obtain information on the spectral characteristics of incident photons and demonstrates that meander-type SSPD's exhibit some photon-number–resolving capability.

- R. Q. Gram, A. She, R. S. Craxton, and D. H. Harding measure the thermal conductivity of solid D_2 by the 3ω method, in which a wire embedded in the medium serves as both a heater and a temperature sensor (p. 48). Accurate values of conductivity are obtained for solid D_2 in the temperature range 13.4 K to 18.6 K. In this temperature range, normal and ortho D_2 are found to have the same conductivity.

Alex Shvydky
Editor

Crossed-Beam Energy Transfer in Direct-Drive Implosions

Introduction

The direct-drive approach to inertial confinement fusion (ICF)[1,2] is based on the implosion, compression, and subsequent ignition of millimeter-diameter cryogenic deuterium–tritium (DT) ice shell targets using high-intensity ($I \sim 10^{14}$ to 10^{15} W/cm^2) laser irradiation [Fig. 129.1(a)]. Direct drive offers the possibility of higher gain than from indirect-drive implosions of the same laser energy.[4] [Reference 3 is cited in the caption of Fig. 129.1(a) below.] To validate physics effects in direct-drive–ignition experiments planned for the National Ignition Facility (NIF),[5] the experiments are carried out on the OMEGA Laser System,[6] which employs 60 laser beams with a total energy of up to 30 kJ [Figs. 129.1(b) and 129.1(c)]. Experiments to study ignition-relevant conditions require a laser energy of ~1 MJ and will be conducted on the NIF in the polar-drive configuration.[7]

High-intensity incident light is absorbed in the corona of direct-drive targets, and the released heat drives the implosions by ablating the outer target surface. The dominant absorption mechanism on the OMEGA and NIF lasers, which operate on a wavelength λ_L = 351 nm, is inverse bremsstrahlung, or "collisional absorption."[8] Laser light is absorbed in a relatively narrow radial region with electron densities n_e from ~0.5 to 1 n_{cr}, where $n_{cr} = \pi c^2 m_e / \lambda_L^2 e^2$ is the critical density, m_e is the electron mass, e is the electron charge, and c is the speed of light. The symmetric illumination of targets with many laser beams, crossing each other at different angles and directions, creates conditions for transferring energy among beams because of electromagnetically seeded, low-gain stimulated Brillouin scattering (SBS).[9] Figure 129.2 illustrates the geometry of crossing rays when the most-efficient energy transfer occurs at the radii outside the highest-absorption region with n_e from ~0.1 to 0.5 n_{cr}. The outgoing edge-beam light in Beam 1 seeds perturbations to the incoming center-beam light in Beam 2 (Fig. 129.2), scattering this light outward. Because of this scattering, the incoming light fails to penetrate into the most-absorbing region of the corona (where $n_e \sim n_{cr}$) and

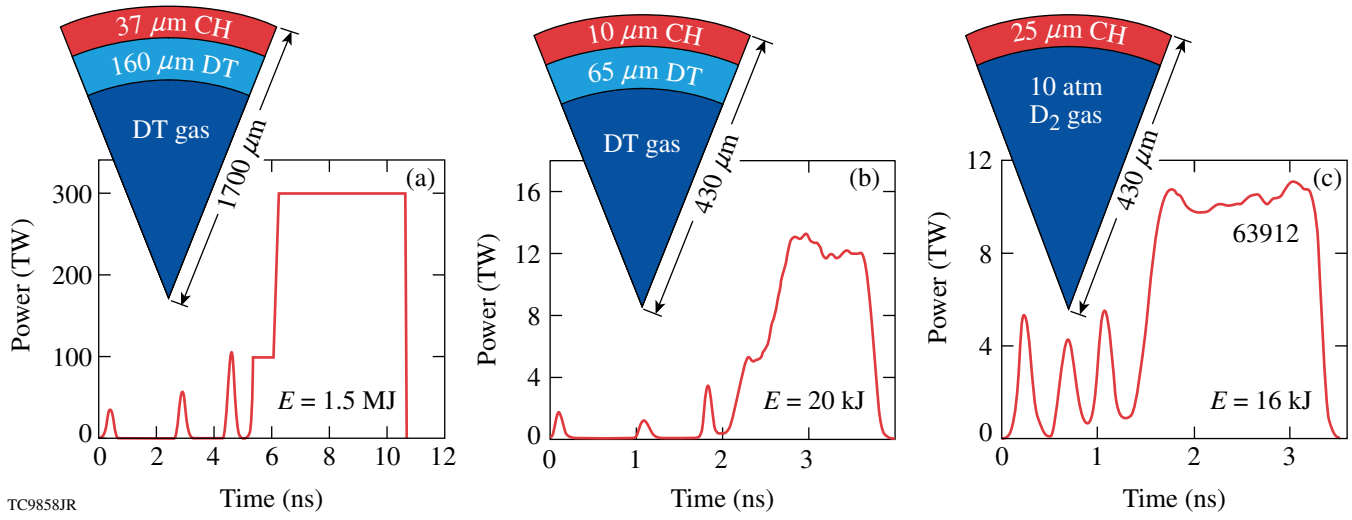

Figure 129.1
(a) A 1.5-MJ direct-drive NIF ignition design.[3] This design utilizes a triple-picket pulse and obtains an energy gain of about 50. (b) Typical cryogenic OMEGA target. This target is a scaled-down version of the design in (a) and is optimized for a laser energy of up to 25 kJ. (c) Example of a warm OMEGA target (shot 63912). Such targets are a less-expensive alternative to cryogenic OMEGA targets. The warm targets are used to study laser coupling, hydrodynamic stability, hot-spot formation, and other aspects of implosion physics.

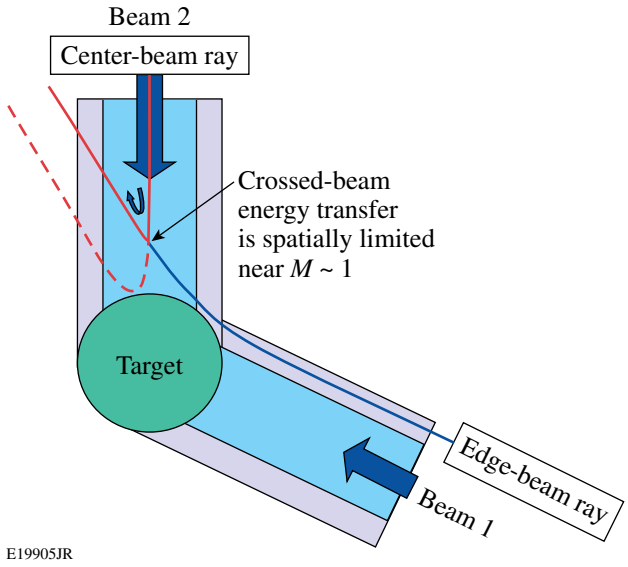

Figure 129.2
Schematic illustration of a laser-ray geometry with the most energetically efficient crossed-beam energy transfer (CBET) in the corona of an implosion target. An incident edge-beam ray (shown in blue) in Beam 1 is refracted and turned outward above the critical radius. On its outgoing trajectory, this ray seeds perturbations to an incoming center-beam ray (shown in red) in Beam 2 that results in energy transfer from the latter ray to the outgoing ray (also shown in red). The energy transfer occurs near the Mach 1 radius, which is typically located at n_e from 0.2 to 0.3 n_{cr}. As the result of CBET, center-beam rays deliver less energy to the maximum absorption region near the critical radius.

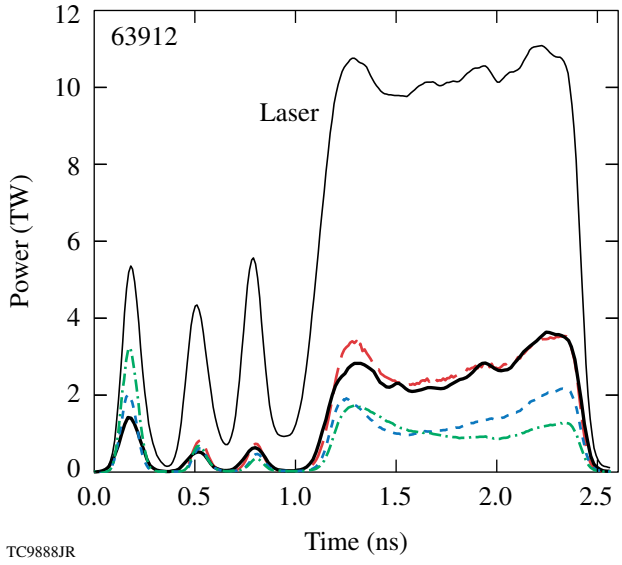

Figure 129.3
Reflected light power history measured (thick black line) and simulated using flux-limited transport (green dashed–dotted line), nonlocal transport (blue dashed line), and nonlocal transport with CBET (red dashed line). The thin black line shows the incident laser power. Note good agreement between the measured power history and the simulated one with CBET.

deposits its energy there, as it does without scattering, reducing laser coupling. Calculations show that crossed-beam energy transfer (CBET) becomes important in OMEGA implosions at intensities $I > 10^{14}$ W/cm^2.

Figure 129.3 illustrates the discrepancy between the modeled scattered-light power without CBET in a plastic-shell (CH) implosion driven at $I = 4.5 \times 10^{14}$ W/cm^2 and experimental observations. The green dashed–dotted and blue dashed lines in Fig. 129.3 show simulated powers using flux-limited (with the flux-limiter parameter $f = 0.06$)[10] and nonlocal[11] heat transport models, respectively. These simulations significantly underestimate and are not able to correctly reproduce the measured power[12] shown by the thick solid black line in Fig. 129.3. The simulations overpredict the measured absorption by about 10%. Simulations of the same implosion but including CBET accurately reproduce the measurements (compare red dashed and solid black lines in Fig. 129.3). Simulations including CBET show good agreement with all observables in implosion experiments using different laser energies, pulse shapes, and targets. Examples of these simulations are discussed in Ref. 13 with more examples discussed below. Good agreement with measurements is obtained only in simulations using CBET and nonlocal transport. Simulations using flux-limited transport with or without CBET fail to consistently reproduce experiments.

The performance of implosions can be improved by mitigating CBET.[13] This article considers three mitigation techniques: One technique uses a laser-beam (or focal-spot) diameter smaller than the target diameter. This can be very efficient in reducing CBET and increasing laser coupling, but on the downside the narrow beams introduce beam-overlap nonuniformities, which can degrade the implosion performance. Experiments on OMEGA have been performed to investigate the optimum beam diameters by balancing CBET with the effects of nonuniformity in low-adiabat implosions. This is discussed below in detail. The second technique employs multicolored laser light, which modifies resonance coupling between beams. Using, for example, a two-color split, CBET can be reduced by a factor of 1/2 for the wavelength separation $\Delta\lambda > 5$ Å of the two wavelengths (for 351-nm light). The third technique uses targets with plastic ablators doped with high-Z elements (e.g., Ge).

The following sections describe the simulation technique for modeling CBET (with details described in Appendices A,

B, and C); discuss CBET in OMEGA implosions, comparing simulations and measurements; and consider the three techniques for mitigating CBET: narrow beams, multicolored lasers, and Ge-doped plastic ablators. The conclusions are presented in the final section.

Modeling CBET

The numerical algorithm for CBET considers pairwise interactions of pump light rays (denoted with index j) with probe light rays (denoted with index i). All possible crossings of the pump rays with the probe light on the path ℓ in a target corona are taken into account. The path ℓ is calculated using Snell's law. The intensity of the probe light along ℓ obeys the equation

$$\frac{\mathrm{d}I_i}{\mathrm{d}\ell} = \xi I_i \sum_j L_{ij}^{-1}, \tag{1}$$

where L_{ij} is the SBS gain length for the rays i and j and ξ is a limiting parameter,[13] $0 < \xi \leq 1$ (see the next section). The spatial gain L_{ij} is estimated in the strong damping limit,[8] which is well satisfied in direct-drive implosions,[14] and given in Appendices A and B for the fluid [Eq. (A2)] and kinetic [Eq. (B8)] models, respectively. A random polarization of the illuminating beams in implosions is accounted for in Eq. (1) by increasing L_{ij} by a factor of 2.

The algorithm uses a simplified assumption of spherical symmetry for both the implosion hydrodynamics and laser illumination. Intensity profiles for laser beams can take an arbitrary shape (e.g., super-Gaussian $n = 4$ in the standard OMEGA setup). The algorithm is incorporated into the laser-absorption package of the one-dimensional (1-D) hydrodynamic code *LILAC*,[15] allowing for a self-consistent calculation of laser deposition with CBET.

Simulations of implosions with $I \gtrsim 4 \times 10^{14}$ W/cm^2 show that the CBET model overpredicts scattered power, indicating the possible presence of additional mechanisms that increase laser coupling. This discrepancy is resolved by introducing a simple model for clamping the ion-acoustic waves.[16] The clamp model was incorporated in *LILAC* and is discussed in Appendix C.

CBET in OMEGA Implosions

OMEGA implosions are used to validate the accuracy of the CBET model, comparing simulations with observables. Laser coupling is characterized by the time-dependent absorption fraction, inferred from scattered-light measurements and scattered-frequency spectra.[12] The hydrodynamic efficiency of simulated implosions can be constrained by bang time (time of rising of the neutron rate)[17] and shell trajectory measurements (inferred from x-ray self-emission images of implosion targets).[18]

Simulations of implosions at $I \gtrsim 4 \times 10^{14}$ W/cm^2 indicate that the CBET model overpredicts measured scattered light and, as a result, shows earlier bang times. The agreement with experiments can be improved by reducing CBET in simulations. This is accomplished by clamping ion-acoustic waves with the clamp parameter $\left(\tilde{n}_\mathrm{e}/n_\mathrm{e}\right)_\mathrm{cl}$ (Appendix C).[16] Simulations using a single clamp value show good agreement for implosions with different pulse shapes and intensities up to $I \approx 6 \times 10^{14}$ W/cm^2 (for higher intensities, see below). Targets with different ablators, however, require different clamping. For example, it was found that $\left(\tilde{n}_\mathrm{e}/n_\mathrm{e}\right)_\mathrm{cl} \approx 0.1\%$ fits data for plastic and 10% fits data for glass (SiO_2) ablators. In the previous study,[13] CBET was reduced assuming $\xi < 1$ in Eq. (1). This approach is less universal, however, because it requires different ξ depending on the laser energy, pulse shapes, and targets.

The fluid and kinetic versions of the CBET model (Appendices A and B, respectively) were compared using implosions of plastic- and glass-shell targets. Small differences between the results of these versions were observed. The differences are typically smaller than deviations of simulations from measurements. The majority of simulation results discussed here were obtained using the fluid version, which is less computationally expensive.

Figure 129.3 compares measured and simulated scattered-light powers for a triple-picket, warm plastic-shell implosion with a main pulse intensity $I = 4.5 \times 10^{14}$ W/cm^2 (OMEGA shot 63912).[19] The simulations employing the fluid CBET model with $\left(\tilde{n}_\mathrm{e}/n_\mathrm{e}\right)_\mathrm{cl} = 0.1\%$ (red dashed line) accurately reproduce the measured time-dependent scattered power (thick solid line).

Figure 129.4 compares measured [Fig. 129.4(a)] and simulated scattered-light spectra with [Fig. 129.4(b)] and without CBET [Figs. 129.4(c) and 129.4(d)] for the same implosion as in Fig. 129.3. The simulated spectra reproduce all basic features of the measured spectrum: time-dependent frequency shifts during pickets and an initial blue shift and later red shift of scattered light during the main pulse. The details and accuracy of reproduction of the measured spectrum depend, however, on the heat-transport model used and the presence of CBET.[20] The simulations using flux-limited transport [Fig. 129.4(c)] underestimate the blue shifts during the first picket and initial part of the main pulse, indicating that the density and velocity

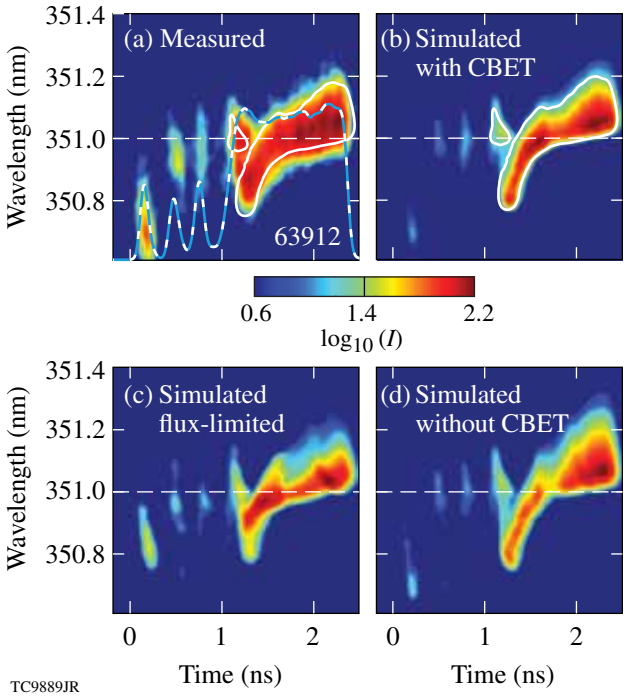

Figure 129.4
(a) Measured and [(b)–(d)] simulated scattered-light spectra for a warm plastic-shell implosion (OMEGA shot 63912). *LILAC* predictions using nonlocal transport and CBET are shown in (b) and simulations without CBET using flux-limited and nonlocal transports are shown in (c) and (d), respectively. The white contours in (a) indicate the shape of the simulated spectrum in (b). The incident light wavelength is represented by the dashed line.

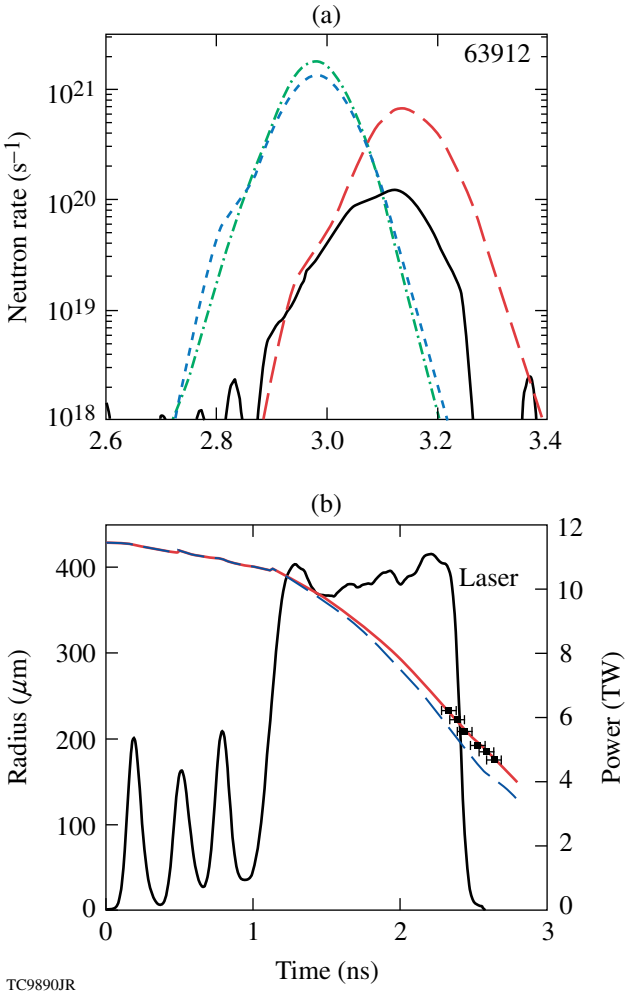

Figure 129.5
(a) Neutron-production history measured (black solid line) and simulated with flux-limited transport (green dashed–dotted line), nonlocal transport (blue dashed line), and nonlocal transport and CBET (red dashed line). The measurements and simulations with CBET show good agreement between bang times, which are estimated as the rise time of the neutron rate. (b) Ablation-front trajectory inferred from x-ray framing camera images[18] (black dots) and the trajectories simulated using nonlocal transport with and without CBET (red solid and blue dashed lines, respectively). The simulations with CBET show good agreement with measurements.

distributions in the target corona are not accurately predicted. The simulations using nonlocal transport without CBET [Fig. 129.4(d)] overestimate the late-time red shift during the main pulse; those with CBET [Fig. 129.4(b)] agree best with the measurements.

The predicted hydrodynamic efficiency of implosions can be verified using measured bang-time and ablation-front trajectories. Figure 129.5(a) shows the measured (solid line) and simulated (blue dashed, green dashed–dotted, and red dashed lines) neutron-production histories for the same implosion as in Fig. 129.3. The experimental bang time for this implosion is about 2.95 ns. The simulations using nonlocal transport and CBET (red dashed line) show bang time coinciding with the measured time within experimental uncertainty. The simulations without CBET, using both flux-limited (green dashed–dotted line) and nonlocal transport (blue dashed line), predict bang times ~200 ps earlier than measured. This is consistent with the higher predicted absorption (or underpredicted scattered-light power) shown in Fig. 129.3.

Figure 129.5(b) shows the measured (squares) and simulated ablation-front trajectories, where the simulations use nonlocal transport with and without CBET (red solid and blue dashed lines, respectively). The trajectory simulated using CBET agrees well with the measured trajectory. The simulations without CBET predict a faster implosion.

Neutron yield is perhaps the most important characteristic of implosions; however, it cannot be directly used to validate the CBET model. This is because the neutron-production

rate strongly depends on temperature and density distributions inside the hot spot.[1] Low-adiabat, warm implosions on OMEGA typically produce yields that are 20% to 25% of *LILAC*-simulated yields. This approximately factor-of-4 yield reduction is unlikely due to inaccuracies in the CBET model and more likely due to asymmetry of implosions. Relative yields, however, are used to study the mitigation of CBET in the **Narrow Beams** section below.

The CBET model was validated using different targets, laser energies, and pulse shapes and shows good and consistent agreement with measurements (see other examples in Ref. 13) up to intensities $I \approx 6 \times 10^{14}$ W/cm^2. At higher intensities of $I \sim 10^{15}$ W/cm^2, the CBET model predicts more scattered light than measured, indicating the presence of an additional absorption mechanism that increases laser coupling. Possible candidates for this mechanism include two-plasmon-decay instability (TPD),[21] which converts incident light into plasma waves with a subsequent dissipation of these waves,[22] and saturation of SBS in intense laser speckles.[23]

Glass-shell implosions were not studied as thoroughly as the plastic-shell implosions discussed above. Only a few implosions were analyzed and were in good agreement with simulations using an appropriate clamp parameter. Figure 129.6 presents an example of a glass-shell implosion that used an 860-μm-diam, 20-μm-thick glass shell filled with 20 atm of D_2 gas. A shaped pulse [the thin solid line in Fig. 129.6(a)] with 26 kJ of energy was used to provide an on-target intensity of $I \approx 10^{15}$ W/cm^2. The best agreement between measured and predicted scattered-light and neutron-production histories [see Figs. 129.6(a) and 129.6(b), respectively] was obtained using simulations with nonlocal transport and CBET, in which $\left(\tilde{n}_e/n_e\right)_{cl} = 10\%$ (compare thick solid and red dashed lines). Simulations without CBET using flux-limited and nonlocal transports [the dashed–dotted and short-dashed lines in Figs. 129.6(a) and 129.6(b)] show significant disagreement with measurements.

Mitigation of CBET

CBET significantly reduces laser coupling in direct-drive implosions. While the laser absorption in a typical OMEGA implosion is reduced by ~10%, the implosion hydrodynamic efficiency is reduced by ~20%. This can be attributed to the laser-deposition area moving outward from the critical surface when CBET is present.[13] Laser coupling can be partially or, in some cases, completely recovered by employing different mitigation techniques for CBET. Three such techniques are considered below. One technique uses narrow laser beams and is extensively tested in OMEGA experiments and simulations. The other two techniques use multicolored lasers and high-Z dopant ablators.

1. Narrow Beams

The idea of using narrow beams to mitigate CBET is illustrated in Fig. 129.2, which shows a ray geometry with the most-efficient energy transfer. By narrowing the beams, one can eliminate edge-beam rays that seed CBET. Figure 129.7 quantitatively illustrates the contribution of different parts of

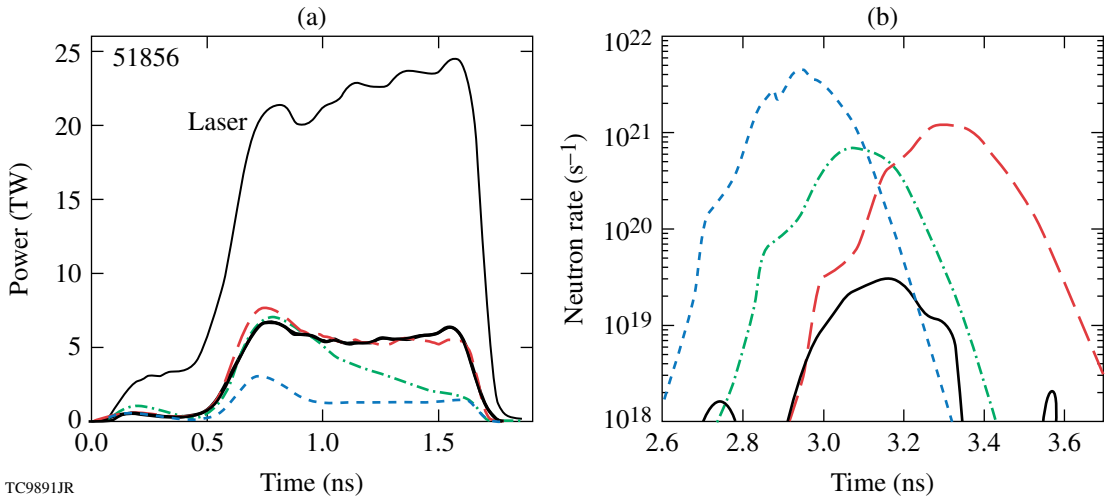

Figure 129.6
(a) Reflected-light power history in a glass-shell implosion (OMEGA shot 51856). (For notations see Fig. 129.3.) (b) Neutron-production history measured and simulated. [For notations see Fig. 129.5(a).] Note good agreement of the measured scattered light and bang time in (a) and (b) with the simulations with CBET and poor agreement with the simulations without CBET.

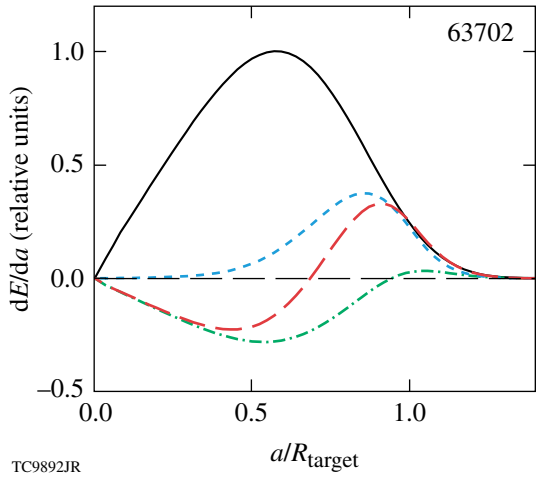

Figure 129.7
Distributions of time-integrated energy transferred between crossing beams as functions of the relative ray impact parameter a/R_{target} in a plastic-shell implosion (OMEGA shot 63702). Distribution of the incident energy is shown by the black solid line. Distribution of the transferred energy for the incoming trajectories is shown by the green dashed–dotted line, for the outgoing trajectories by the blue dashed line, and for whole trajectories (including the incoming and out-going parts) by the red dashed line. The negative dE/da corresponds to energy losses and the positive one to energy gains.

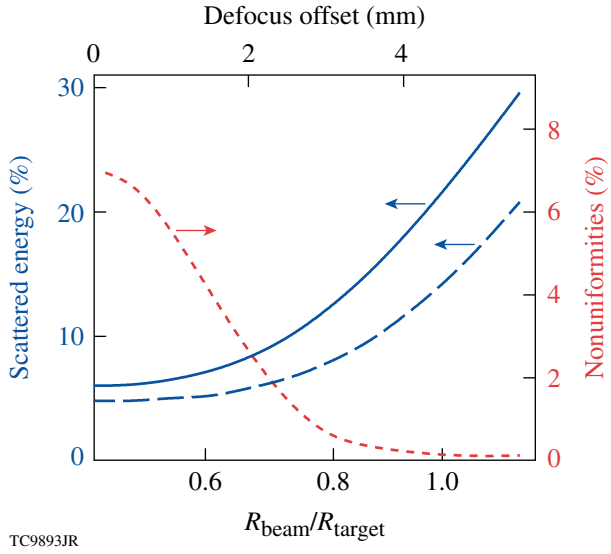

Figure 129.8
Predicted scattered energy and deposition nonuniformities (rms) as functions of R_{beam}/R_{target} in plastic-shell implosions. The scattered energy is normalized to the incident energy. The simulated energies with and without CBET are shown by the blue solid and dashed lines, respectively. The deposition nonuniformities (red dashed line) are calculated using the OMEGA beam-port geometry and time averaging over the whole laser pulse.

beams to CBET. This figure shows the simulated distributions of energy transferred to (when the sign of dE/da is positive) or from (when the sign is negative) light rays with an impact parameter a. The outgoing rays (blue dashed line) always gain energy, and the gain reaches the maximum for rays with a/R_{target} from ~0.7 to 1.1. The incoming rays (green dashed–dotted line) mostly lose energy, transferring it to outgoing rays. This loss takes place for a/R_{target} from 0 to ~0.9 and is peaked at $a/R_{target} \sim 0.5$. The incoming rays with $a/R_{target} \gtrsim 0.9$ gain some energy, but this gain is not significant. The rays with $0.5 \lesssim a/R_{target} \sim 0.9$ lose energy as they travel toward the target and gain it on the way out. The cumulative effect of CBET for the whole ray trajectory (including the incoming and outgoing parts) is shown by the red dashed line in Fig. 129.7. The rays with $a/R_{target} < 0.7$ overall lose energy and the rays with $a/R_{target} > 0.7$ gain energy. This suggests that by eliminating rays with $a/R_{target} > 0.7$, one can completely suppress CBET.

Figure 129.8 shows simulation results for implosions at the same conditions [similar to the one shown in Fig. 129.1(c)] except using different beam radii R_{beam}, which are defined to encircle 95% energy. The beam radius is changed by defocusing beams with an assumed profile $I(r) \sim \exp\left[-\left(r/r_0\right)^{2.1}\right]$, where $r_0 = 135\ \mu$m. The ratio R_{beam}/R_{target} is varied from 0.5 to 1.1. The simulations including CBET (solid line) show a decrease in scattered energy when R_{beam}/R_{target} is decreased. The scattered energy in the simulations without CBET (blue dashed line) is reduced as well. This is because smaller beams provide illumination of the target surface by more-normal incident light. Such light penetrates deeper into the target corona and is absorbed more efficiently. Therefore, the benefits of using smaller beams include two aspects: reducing CBET and increasing absorption as a result of more-normal incident light.

The smaller beams can have a negative effect on implosion performance because of increasing beam-overlap nonuniformities. Two-dimensional (2-D) hydrodynamic simulations using the code *DRACO*[24] predict nearly symmetric implosions and small reduction in neutron yield for R_{beam}/R_{target} from ~1 to 0.8 [see Figs. 129.9(a) and 129.9(b)]. Simulations assuming $R_{beam}/R_{target} \lesssim 0.7$ show significantly distorted targets at maximum compression and reduced neutron yields [by a factor of 2 or more, see Fig. 129.9(c)]. These 2-D results agree with the simple calculations of deposition nonuniformities presented in Fig. 129.8 (red dashed line). The calculations predict a significant increase in the nonuniformities in the range of R_{beam}/R_{target} from 0.8 to 0.7. Therefore, these results suggest

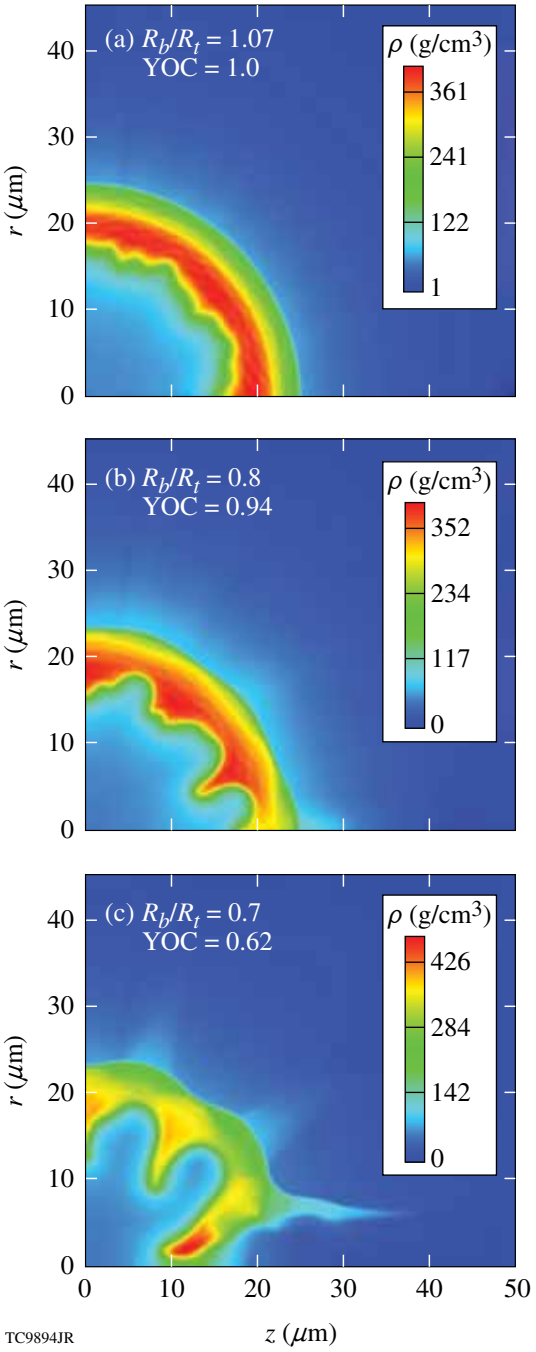

Figure 129.9
Density distributions at maximum compression from 2-D hydrodynamic simulations of implosion targets illuminated by different-sized laser beams: (a) $R_{beam}/R_{target} = 1.07$, (b) 0.8, and (c) 0.7. Beam-overlap nonuniformities in the case of small R_{beam}/R_{target} result in asymmetric implosions and degradation of neutron yield. Each simulation shows yield over clean (YOC, which is the 2-D yield normalized to the 1-D yield).

an optimum $R_{beam}/R_{target} \sim 0.8$ that balances the reduction of CBET and increase of beam-overlap nonuniformities.

Two sets of implosion experiments on OMEGA were performed to investigate the effects of narrow beams. These experiments used triple-picket pulses with a peak overlap intensity $I \approx 4.5 \times 10^{14}$ W/cm^2 that drive targets with an adiabat[a] $\alpha \approx 4$. The primary goal of the first set of experiments is to demonstrate enhanced laser coupling in implosions with narrow-beam illumination.[25] The experiments use fixed-diameter (860-μm) nominal OMEGA targets and variable-diameter beams. The beam diameters are varied by defocusing beams obtained using small distributed phase plates (DPP's).[26] Figure 129.10 shows the measured beam profiles for different defocus offsets corresponding to different R_{beam}/R_{target}.

The experiments with variable beams use a range of R_{beam}/R_{target} from 0.5 to 1.09. Figure 129.11 compares measured and simulated scattered-light spectra for wide and narrow beams ($R_{beam}/R_{target} = 1.0$ and 0.5, respectively). Note the good agreement between the simulated and measured spectra. The implosion with narrow beams and reduced CBET shows the presence of the red-shifted part of the spectrum, which corresponds to light that deeply penetrates inside the target corona.

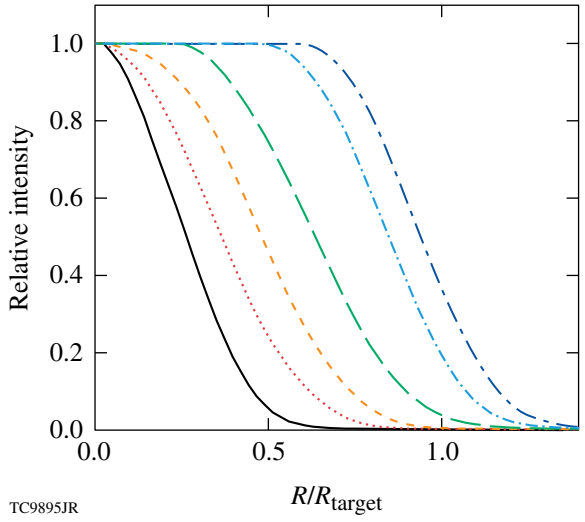

Figure 129.10
Measured profiles of beams with small distributed phase plates (DPP's) at different defocus offsets. The beam profile at best focus is shown by the solid line and wider beams have increasing defocus offsets. These profiles correspond to $R_{beam}/R_{target} = 0.5, 0.65, 0.74, 0.88, 1.0$, and 1.09 (from narrow to wide, respectively).

[a]The ratio of the pressure in an imploding shell to the Fermi-degenerate pressure.

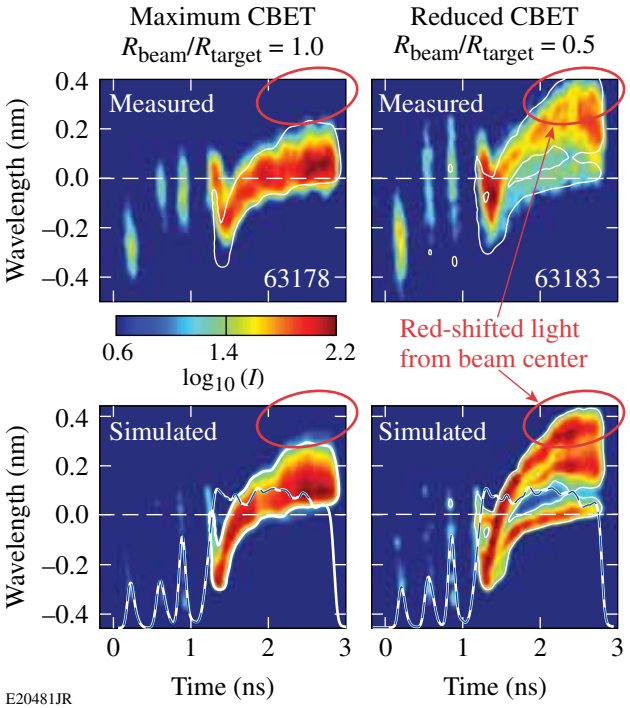

Figure 129.11
Measured and simulated scattered-light spectra for plastic-shell implosions using wide and narrow laser beams (R_{beam}/R_{target}=1.0 and 0.5, respectively). The implosion with narrow beams recovers the red-shifted part of the spectrum (shown by the red ovals), which corresponds to rays that deeply penetrate into the target corona. These rays are not present in the implosion with wide beams $\left(R_{beam}/R_{target} = 1.0\right)$ because of CBET. Note good agreement between measured and simulated spectra.

The implosions with wide beams $\left(R_{beam}/R_{target} = 1.0\right)$ do not show such red-shifted parts, indicating that deeply penetrated light has been scattered.

Figure 129.12 shows the scattered-light fractions in implosions with different R_{beam}/R_{target}. The measured fractions (solid red circles with error bars) are reduced in implosions with narrower beams, in agreement with simulations that include CBET (triangles and solid line). The reduction in scattered light and corresponding increase in absorption result in earlier bang times in implosions with narrow beams. Figure 129.13 summarizes the bang-time measurements and shows good agreement between the measurements (solid circles) and simulations with CBET (triangles).

The earlier bang times correspond to higher-velocity implosions in agreement with the results of the ablation-front trajectory measurements. Figure 129.14(a) shows two examples of trajectories both measured (squares) and simulated with CBET (lines), for R_{beam}/R_{target}=1.0 and 0.75. The targets illuminated with smaller beams clearly demonstrate higher velocity. Figure 129.14(b) compares the implosion velocities inferred from the measured trajectories (squares) and those simulated with and without CBET (triangle and diamonds, respectively).

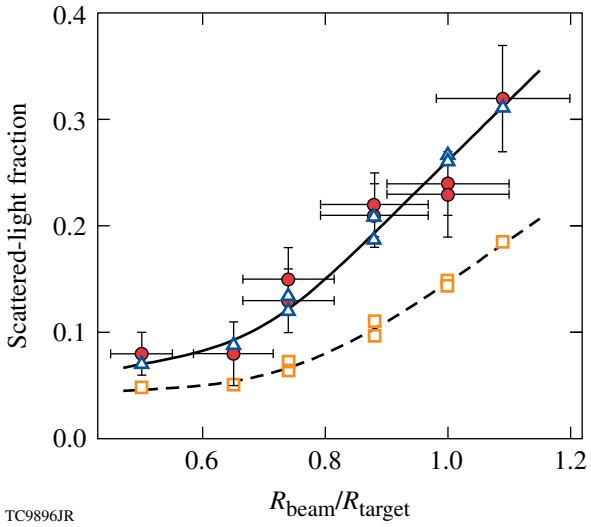

Figure 129.12
Scattered-light fractions in implosion experiments using variable-diameter beams. Measurements corresponding to implosions with different R_{beam}/R_{target} are shown by the solid red circles with error bars. Simulation results with and without CBET are shown by the blue open triangles and orange open squares and approximated by the solid and dashed lines, respectively. The measured fractions are in good agreement with the simulated ones including CBET.

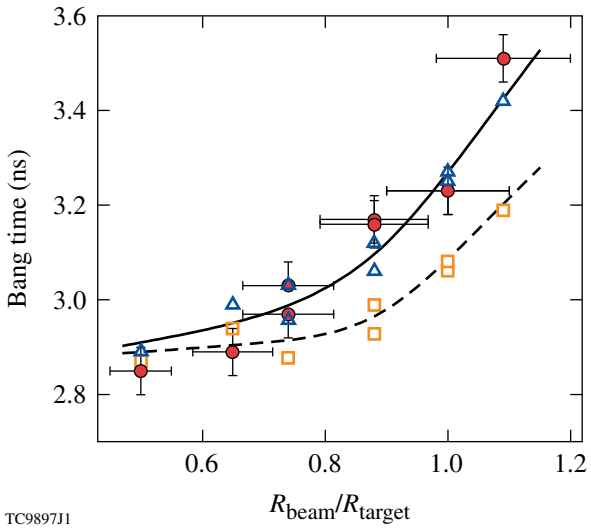

Figure 129.13
Bang times in implosion experiments using variable-diameter beams. (For notations see Fig. 129.12.) The measured bang times are in good agreement with the simulated ones including CBET.

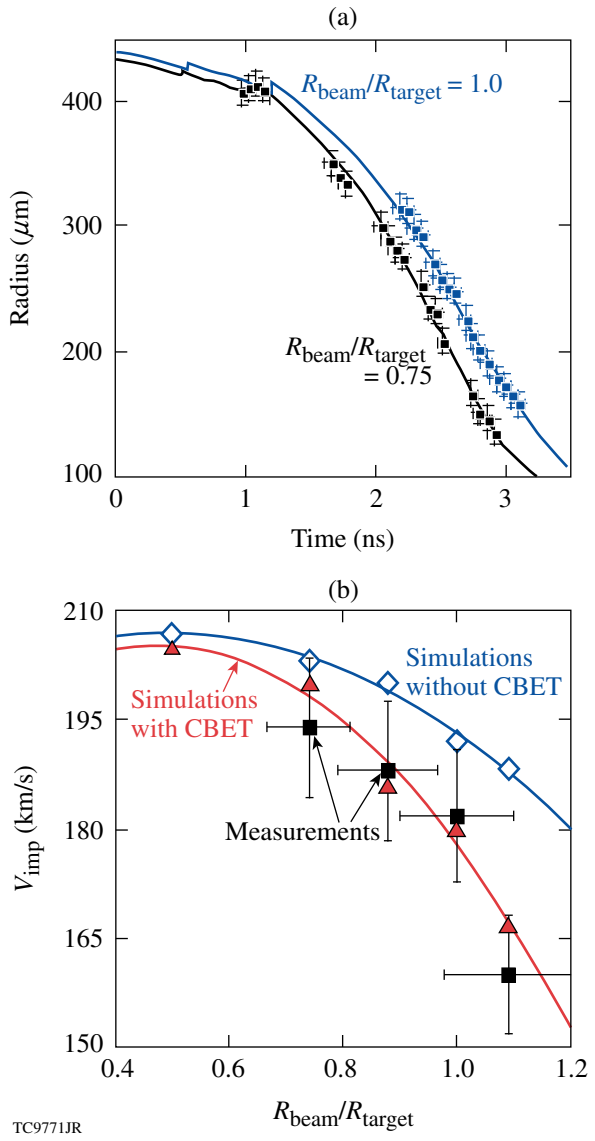

Figure 129.14
(a) Ablation-front trajectories inferred from x-ray framing camera images (squares) and simulated (lines) in implosions with wide and narrow beams (R_{beam}/R_{target} = 1.0 and 0.75, respectively). (b) Measured (squares) and simulated with (red line and triangles) and without (blue line and diamonds) CBET implosion velocities as functions of R_{beam}/R_{target}. Higher implosion velocities are achieved with smaller beams in both measurements and simulations.

Higher implosion velocities are achieved with smaller beams in both measurements and simulations, and the simulations with CBET show good agreement with the measured data (triangles and squares).

The described experiments cannot, however, be used to demonstrate improvements in neutron yield because of the significant level of single-beam nonuniformity (imprint) when using beams smaller than target diameters. As a result, measured neutron yields are reduced by a factor of 5 to 10 with respect to the yields in similar implosions but illuminated with best uniformity. To address the issue of yield improvement, additional experiments employing uniform beams with standard OMEGA SG4 DPP's, polarization smoothing (PS),[27] and smoothing by spectral dispersion (SSD)[28] were performed. The SG4 DPP's with PS and SSD are optimized for the on-target uniformity in the case of 860-μm-diam targets. These experiments vary R_{beam}/R_{target} by changing the target size. The three target diameters used—860, 950, and 1000 μm—correspond to R_{beam}/R_{target} = 0.97, 0.88, and 0.83, respectively. This range of R_{beam}/R_{target} was narrower than that used in the previous set of experiments but covers the important region around $R_{beam}/R_{target} \sim 0.8$, where significant changes in neutron yield are expected because of beam-overlap nonuniformities. To reduce the effects of small-scale single-beam imprinting, the implosions were designed to be robust to Rayleigh–Taylor instability,[29] having relatively low in-flight aspect ratio[1] IFAR ≈ 30, which was about the same for all targets.

Figure 129.15(a) shows measured neutron yields that were normalized to simulations including CBET (circles) as a function of R_{beam}/R_{target}. If all nonuniformity sources are kept constant for different R_{beam}/R_{target}, then expected measured yields normalized to predicted yields should be independent of R_{beam}/R_{target}. This is shown in Fig. 129.15(a) by the dashed line. The data follow this line down to $R_{beam}/R_{target} \approx 0.86$. For smaller R_{beam}/R_{target}, the relative yields drop because of enhanced beam-overlap nonuniformity. Figure 129.15(b) demonstrates the benefit of using narrow beams, showing the same measurements as in Fig. 129.15(a) but normalized to simulations without CBET and assuming R_{beam}/R_{target} = 1. Such a normalization uses "clean" yields without both beneficial effects of narrow beams: reduced CBET and more-normal light illumination. The relative yields in Fig. 129.15(b) show an increase by a factor of ~1.5 for smaller beams with the maximum yield at $R_{beam}/R_{target} \approx 0.88$. Further reduction of R_{beam}/R_{target} results in a reduction in yields, indicating that beam-overlap nonuniformities dominate the target performance. These data demonstrate the beneficial effects of reducing R_{beam}/R_{target} from ~1 down to ≈0.85.

2. Multicolored Lasers

The efficiency of CBET is determined by the SBS gain, which is resonant and sensitive to a wavelength separation $\Delta\lambda$ between interacting beams [see Eqs. (A2) and (B8) in Appendices A and B]. Changing the wavelengths of beams affects the SBS gain and, therefore, increases or decreases CBET. Benefits of a wavelength separation technique were recently demon-

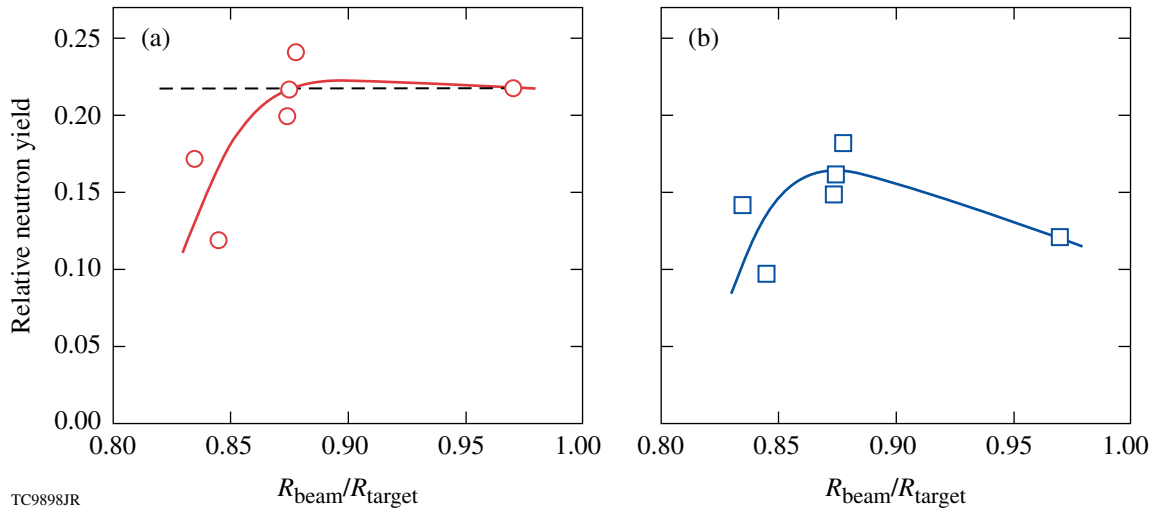

Figure 129.15
Relative neutron yields in experiments using uniform beams and variable-diameter targets. (a) Measured yields normalized to simulations with CBET (circles). (b) The same yields as in (a) but normalized to simulations without CBET and having $R_{beam}/R_{target} = 1$ (squares). The solid lines in (a) and (b) approximate the data points. The dashed line in (a) shows an expected constant relative yield in the case of similar uniformity. The drop of relative yields at $R_{beam}/R_{target} < 0.86$ is due to an increase in beam-overlap nonuniformities at small R_{beam}/R_{target}.

strated in indirect-drive implosions on the NIF.[30] The applied $\Delta\lambda$ in these implosions is relatively small (up to ~3 Å in UV light). Mitigation of CBET in direct-drive implosions requires a larger $\Delta\lambda$ among beams to eliminate the coupling resonances.[13]

To illustrate the CBET mitigation effect in direct-drive experiments, consider the simplest case of a laser system operating on two subsets of lasers with wavelengths separated by $\Delta\lambda$. These wavelengths can be distributed among different beams, or each beam can include both wavelengths (e.g., as a uniform mix, or one wavelength at the center and the other at the edge of a beam). For a large separation,

$$\Delta\lambda \gg \lambda_L\left(c_a/c\right) \sim 5\,\text{Å}, \tag{2}$$

one subset does not "see" the presence of the other and there is no interaction between them [i.e., gain length L_{ij} becomes large, see Eq. (1)]. Here, $c_a = \sqrt{\left(ZT_e + 3T_i\right)/M_i}$ is the ion-acoustic sound speed, Z is the ionization, M_i is the ion mass, and T_e and T_i are the electron and ion temperatures, respectively. In this case of large $\Delta\lambda$, CBET occurs only within each subset and, therefore, the total CBET is reduced by 1/2 with respect to the case of $\Delta\lambda = 0$. [This reduction is equivalent to assuming $\xi = 1/2$ in Eq. (1)]. Figure 129.16 shows simulated absorption fractions (solid line) for a plastic-shell implosion driven by two-color illumination as a function of $\Delta\lambda$. The absorption fraction changes very little for $\Delta\lambda < 3$ Å and increases significantly (by up to 10%) for $\Delta\lambda > 5$ Å. The dashed line in Fig. 129.16 shows the asymptotic limit of 1/2 CBET. In general, an N-color separation can result in the asymptotic reduction of CBET by a factor of $1/N$.

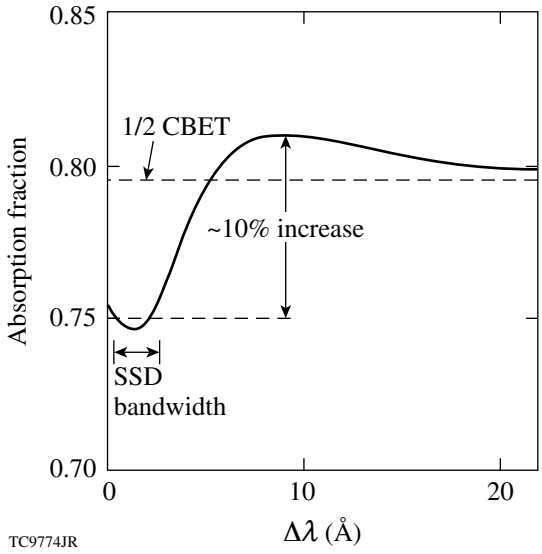

Figure 129.16
Simulated absorption fraction (solid line) as a function of the wavelength separation $\Delta\lambda$ in a plastic-shell implosion using two-color light. The upper dashed line corresponds to 50%-reduced CBET using one-color light.

As a practical application of laser drive using two or more colors distributed among different beams, a uniform spatial mix of these beams is suggested. More beams will provide a better

mixing uniformity, and using more colors is more beneficial in reducing CBET.

The results discussed in this section neglect the effects of TPD instability and laser speckles. The presence of speckles and anomalous absorption resulting from TPD can significantly modify the results shown in Fig. 129.16 that were obtained using a simple linear theory and the planar wave approximation [Eq. (1)]. Implosion experiments on OMEGA suggest that both these mechanisms, TPD and speckles, are not important at intensities $I \lesssim 6 \times 10^{14}$ W/cm^2 (see **CBET in OMEGA Implosions**, p. 3). One can expect that the multicolored technique can work in implosions within this range of intensities, and more theoretical study is required to accurately predict laser coupling at higher intensities.

3. High-Z Dopants

The dependence of CBET on plasma ion charge Z is complex (see Appendices A and B). Ion charge also affects other aspects of implosion physics: in particular, heat transport and hydrodynamics.

Figure 129.17 presents simulation results for implosion plastic shells with the varied dopant concentration of Ge: 0%, 1%, and 4%. The absorption fraction grows with increased Ge concentration in simulations both including (circles) and not including (triangles) CBET. The simulations including CBET show an ~6% larger increase in absorption for 4%-Ge doping. These indicate a reduction of CBET in implosions with doped ablators, which is mainly caused by increased coronal electron temperature in these implosions. On the other hand, because of less-effective heat transport in a higher-Z coronal plasma, the hydrodynamic efficiency of these implosions is reduced. The simulations show that 4%-Ge dopant reduces the hydrodynamic efficiency by ~5% (see diamonds in Fig. 129.17), reducing the overall benefit of using high-Z dopants in direct-drive implosions.

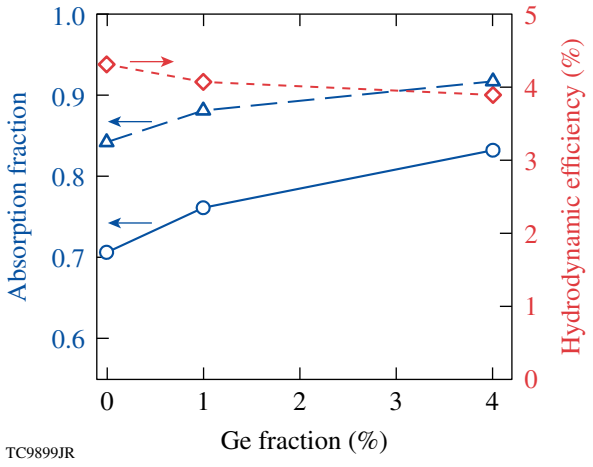

Figure 129.17
Simulated absorption fractions with (solid line and circles) and without (blue dashed line and triangles) CBET for imploded plastic shells with different fractions of doped Ge. The effect of CBET is reduced in implosions with a higher-Ge dopant. Hydrodynamic efficiency in implosions with CBET (red dashed line and diamonds) is decreased with increasing-Ge dopant.

Conclusions

CBET can significantly reduce the performance of direct-drive ICF implosions. It is responsible for about 10% reduction of laser absorption and about 20% reduction of hydrodynamic efficiency in implosion experiments on OMEGA. CBET is observed in time-resolved, scattered-light spectra as a suppression of red-shifted light during the main laser drive. This light is present in simulations without CBET, indicating that CBET mostly scatters the center-beam incoming light, which otherwise would penetrate to higher-density corona regions, where it is reflected with the maximum red shift.

Two models of CBET have been developed and implemented into the laser-absorption package of the 1-D hydrodynamic code *LILAC*: a fluid model (Appendix A) and a kinetic model (Appendix B), assuming spherically symmetric laser illumination of implosion targets. Both models were extensively tested using different OMEGA implosions with varied laser energies, pulse shapes, and target structure and composition. These demonstrated good agreement between model predictions and observables, which include scattered-light spectra and power, bang times, shell trajectories, and neutron yields (see **CBET in OMEGA Implosions**, p. 3). The fluid and kinetic models show quite similar results between each other.

The performance of direct-drive targets can be improved by mitigating CBET. This article considered three mitigation techniques: using narrow beams, using multicolored lasers, and high-Z–doped ablators. The first technique is efficient in improving laser coupling. The implosion experiments on OMEGA show a significant decrease of scattered-light power, earlier bang times, and an increase in implosion velocity (see Figs. 129.12–129.14) when reducing the beam radius. The small beams introduce more beam-overlap nonuniformities that reduce implosion performance by decreasing neutron yields. The experiments on OMEGA suggest an optimum $R_{\text{beam}}/R_{\text{target}} \sim 0.85$ that maximizes the performance by balancing CBET with the effects of beam-overlap nonuniformities (see Fig. 129.15).

Simulations suggest that using multicolored lasers can be another efficient technique to mitigate CBET. By splitting light into N separate colors, CBET can be reduced by a factor of ~1/N. This technique requires, however, relatively large wavelength separations $\Delta\lambda$ [Eq. (2)], which probably cannot be achieved on the OMEGA and NIF lasers. To utilize the multicolored split technique, future direct-drive laser systems should be designed to use subsets of lasers operating at different wavelengths. Such systems can benefit from using the narrow-beam technique discussed above and using many separate beams to reduce beam-overlap nonuniformity.

Test simulations of imploded plastic shells doped with high-Z elements reveal no advantages to using this technique. Unless the simulations show a relative reduction in CBET and improvement in laser coupling in the case of Ge-doped targets, the overall implosion performance suffers because of the reduction in heat transport in a higher-Z coronal plasma (see Fig. 129.17).

ACKNOWLEDGMENT

This work was supported by the US DOE Office of Inertial Confinement Fusion under Cooperative Agreement No. DE-FC52-08NA28302, the University of Rochester, and the New York State Energy Research and Development Authority. The support of DOE does not constitute an endorsement by DOE of the views expressed in this article.

Appendix A: Fluid Equations

The fluid approach for the CBET model is based on the electron-density equation, the equation of motion for ions, and the wave equation for laser light.[8] The steady-state interaction of two light waves of the same linear polarization and an ion-acoustic wave is considered in the strong damping limit. Details of derivation of the equation for the probe-light intensity I_{probe} are given in Ref. 9; this equation can be written as

$$\frac{\mathrm{d}I_{\text{probe}}}{\mathrm{d}\ell} = \frac{I_{\text{probe}}}{L}, \tag{A1}$$

where ℓ is the probe-light path,

$$L^{-1} = \frac{\pi}{\lambda_L}\frac{n_e/n_{cr}}{\sqrt{1-n_e/n_{cr}}} \times \frac{1}{\left[\tilde{\nu}_a^2\eta^2+\left(1-\eta^2\right)^2\right]^{1/2}}\left(\frac{I_{\text{pump}}}{I_{\text{probe}}}\right)^{1/2}\left|\frac{\tilde{n}_e}{n_e}\right| \tag{A2}$$

is the SBS spatial gain rate,

$$\left|\frac{\tilde{n}_e}{n_e}\right| = \frac{e^2\lambda_L^2}{\pi m_e^2 c^3}\frac{Z}{c_a^2}\left(\frac{m_e}{M_i}\right)\frac{\left(I_{\text{probe}}I_{\text{pump}}\right)^{1/2}}{\left[\tilde{\nu}_a^2\eta^2+\left(1-\eta^2\right)^2\right]^{1/2}} \tag{A3}$$

is the relative amplitude of electron-density perturbations in the ion-acoustic wave, and I_{pump} is the pump-light intensity. In Eqs. (A2) and (A3), $\tilde{\nu}_a = \nu_a/k_a c_a$ is the dimensionless damping of ion-acoustic waves.[31] The variable η includes the dependency on geometry and frequency of the interacting waves,

$$\eta = \frac{\left(\mathbf{k}_a\cdot\mathbf{u}\right)}{k_a c_a} - \frac{\omega_a}{k_a c_a}, \tag{A4}$$

where $\mathbf{u}$ is the flow velocity and ω_a and $\mathbf{k}_a$ are the ion-acoustic wave frequency and wave vector, respectively. The interacting waves satisfy the following three-wave matching conditions:

$$\omega_a = \omega_{\text{probe}} - \omega_{\text{pump}} \tag{A5}$$

and

$$\mathbf{k}_a = \mathbf{k}_{\text{probe}} - \mathbf{k}_{\text{pump}}. \tag{A6}$$

The frequency changes in probe and pump light are calculated considering the plasma expansion and Doppler effects.[32] More details of implementation of Eq. (A1) into *LILAC* can be found in Ref. 13.

Appendix B: Kinetic Equations

The electron-density perturbation $\tilde{n}_e$ in an ion-acoustic wave is calculated using the linearized Vlasov equations for electrons and ions and the Poisson equation for the self-consistent electrostatic potential. One gets[33]

$$\tilde{n}_e = \frac{k_a^2\phi_p}{4\pi e}\frac{\chi_e\left(1+\Sigma_i\chi_i\right)}{1+\chi_e+\Sigma_i\chi_i}, \tag{B1}$$

where the summation is taken over all ion species, ϕ_p is the beat ponderomotive potential of interacting light waves, χ_e and χ_i are the electron and ion linear susceptibilities, respectively, which can be written as follows:

$$\chi_e \approx \omega_{pe}^2/k_a^2 v_{T_e}^2, \tag{B2}$$

$$\chi_{\mathrm{i}} = \frac{\omega_{\mathrm{pi}}^2}{k_{\mathrm{a}}^2 v_{\mathrm{T_i}}^2}\left(1 + \frac{x}{\sqrt{\pi}}\int_{-\infty}^{\infty}\frac{e^{-z^2}}{z-x}\mathrm{d}z\right), \tag{B3}$$

and

$$x = \frac{\omega_{\mathrm{a}} + i\nu_{\mathrm{ie}} - \left(\mathbf{k}_{\mathrm{a}}\cdot\mathbf{u}\right)}{\sqrt{2}\,k_{\mathrm{a}} v_{\mathrm{T_i}}}. \tag{B4}$$

In the above equations, $v_{\mathrm{T_e}} = \left(T_{\mathrm{e}}/m_{\mathrm{e}}\right)^{1/2}$ and $v_{\mathrm{T_i}} = \left(T_{\mathrm{i}}/M_{\mathrm{i}}\right)^{1/2}$ are the electron and ion thermal velocities, respectively; ν_{ie} is the ion–electron collisional frequency; and $\omega_{\mathrm{pe}} = \left(4\pi \mathrm{e}^2 n_{\mathrm{e}}/m_{\mathrm{e}}\right)^{1/2}$ and $\omega_{\mathrm{pi}} = \left(4\pi \mathrm{e}^2 Z n_{\mathrm{e}}/M_{\mathrm{i}}\right)^{1/2}$ are the electron and ion plasma frequencies, respectively.

The equation for light waves is

$$\frac{\partial^2 \mathbf{A}}{\partial t^2} - c^2\Delta\mathbf{A} + \omega_{\mathrm{pe}}^2\left(1 + \frac{\tilde{n}_{\mathrm{e}}}{n_{\mathrm{e}}}\right)\mathbf{A} = 0. \tag{B5}$$

Assuming that the probe and pump waves are *s*-polarized, the corresponding component of the vector potential **A** can be expressed as

$$A(\mathbf{r},t) = \frac{1}{2}\Big[A_{\mathrm{probe}}\exp\left(-i\omega_{\mathrm{probe}}t + i\mathbf{k}_{\mathrm{probe}}\mathbf{r}\right) + A_{\mathrm{pump}}\exp\left(-i\omega_{\mathrm{probe}}t + i\mathbf{k}_{\mathrm{probe}}\mathbf{r}\right) + \mathrm{c.c.}\Big]. \tag{B6}$$

Then the potential ϕ_{p} takes the form

$$\phi_{\mathrm{p}} = -\frac{\mathrm{e}}{2m_{\mathrm{e}}c^2}A_{\mathrm{probe}}A_{\mathrm{pump}}^{*}. \tag{B7}$$

Substituting Eq. (B1) into Eq. (B5), and using Eqs. (B6) and (B7), and the definition $A^2 = 8\pi cI/\omega_{\mathrm{L}}^2$, where ω_{L} in the laser frequency, one obtains the equation for the probe light-intensity I_{probe}, similar in form to Eq. (A1), in which

$$L^{-1} = \frac{\pi}{\lambda_L}\frac{n_{\mathrm{e}}/n_{\mathrm{cr}}}{\sqrt{1 - n_{\mathrm{e}}/n_{\mathrm{cr}}}}\frac{\mathrm{Im}(B)}{|B|}\left(\frac{I_{\mathrm{pump}}}{I_{\mathrm{probe}}}\right)^{1/2}\left|\frac{\tilde{n}_{\mathrm{e}}}{n_{\mathrm{e}}}\right|, \tag{B8}$$

$$\left|\frac{\tilde{n}_{\mathrm{e}}}{n_{\mathrm{e}}}\right| = \frac{\mathrm{e}^2\lambda_L^2}{\pi m_{\mathrm{e}}^2 c^3}\frac{k_{\mathrm{a}}^2}{\omega_{\mathrm{pe}}^2}\frac{\left(I_{\mathrm{probe}}I_{\mathrm{pump}}\right)^{1/2}}{|B|}, \tag{B9}$$

and

$$B = \frac{1 + \chi_{\mathrm{e}} + \Sigma_{\mathrm{i}}\chi_{\mathrm{i}}}{\chi_{\mathrm{e}}\left(1 + \chi_{\mathrm{i}}\right)}. \tag{B10}$$

The interacting ion-acoustic and light waves satisfy the matching conditions given by Eqs. (A5) and (A6). Equations (B8) and (B9) substitute the fluid approach equations [Eqs. (A2) and (A3)] in the numerical procedure when the kinetic option is chosen.

Appendix C: The Clamp Model

The amplitude of ion-acoustic waves can experience a nonlinear saturation, depending on the laser intensities and ion composition of a plasma. This saturation can reduce an energy transfer predicted by the CBET model. A simple model for clamping of ion-acoustic waves was proposed[16] that limits the amplitude of electron-density perturbations $\left|\tilde{n}_e/n_e\right|$ defined by Eqs. (A3) and (B9) for the fluid and kinetic models, respectively. Specifically, the corresponding values of $\left|\tilde{n}_e/n_e\right|$ in Eqs. (A2) and (B8) are substituted by

$$\left\langle\frac{\tilde{n}_{\mathrm{e}}}{n_{\mathrm{e}}}\right\rangle = \min\left[\left|\frac{\tilde{n}_{\mathrm{e}}}{n_{\mathrm{e}}}\right|, \left(\frac{\tilde{n}_{\mathrm{e}}}{n_{\mathrm{e}}}\right)_{\mathrm{cl}}\right]. \tag{C1}$$

The clamping parameter $\left(\tilde{n}_{\mathrm{e}}/n_{\mathrm{e}}\right)_{\mathrm{cl}}$ is determined from experiments.

REFERENCES

1. J. D. Lindl, *Inertial Confinement Fusion: The Quest for Ignition and Energy Gain Using Indirect Drive* (Springer-Verlag, New York, 1998). pp. 39 and 61.
2. R. L. McCrory, D. D. Meyerhofer, R. Betti, R. S. Craxton, J. A. Delettrez, D. H. Edgell, V. Yu Glebov, V. N. Goncharov, D. R. Harding, D. W. Jacobs-Perkins, J. P. Knauer, F. J. Marshall, P. W. McKenty, P. B. Radha, S. P. Regan, T. C. Sangster, W. Seka, R. W. Short, S. Skupsky, V. A. Smalyuk, J. M. Soures, C. Stoeckl, B. Yaakobi, D. Shvarts, J. A. Frenje, C. K. Li, R. D. Petrasso, and F. H. Séguin, Phys. Plasmas **15**, 055503 (2008).
3. V. N. Goncharov, T. C. Sangster, T. R. Boehly, S. X. Hu, I. V. Igumenshchev, F. J. Marshall, R. L. McCrory, D. D. Meyerhofer, P. B. Radha, W. Seka, S. Skupsky, C. Stoeckl, D. T. Casey, J. A. Frenje, and R. D. Petrasso, Phys. Rev. Lett. **104**, 165001 (2010).
4. S. Atzeni and J. Meyer-ter-Vehn, *The Physics of Inertial Fusion: Beam Plasma Interaction, Hydrodynamics, Hot Dense Matter*, International Series of Monographs on Physics (Clarendon Press, Oxford, 2004), p. 4750.

5. J. Paisner *et al.*, Laser Focus World **30**, 75 (1994).

6. T. R. Boehly, D. L. Brown, R. S. Craxton, R. L. Keck, J. P. Knauer, J. H. Kelly, T. J. Kessler, S. A. Kumpan, S. J. Loucks, S. A. Letzring, F. J. Marshall, R. L. McCrory, S. F. B. Morse, W. Seka, J. M. Soures, and C. P. Verdon, Opt. Commun. **133**, 495 (1997).

7. S. Skupsky, J. A. Marozas, R. S. Craxton, R. Betti, T. J. B. Collins, J. A. Delettrez, V. N. Goncharov, P. W. McKenty, P. B. Radha, T. R. Boehly, J. P. Knauer, F. J. Marshall, D. R. Harding, J. D. Kilkenny, D. D. Meyerhofer, T. C. Sangster, and R. L. McCrory, Phys. Plasmas **11**, 2763 (2004).

8. W. L. Kruer, *The Physics of Laser-Plasma Interactions*, Frontiers in Physics, Vol. 73, edited by D. Pines (Addison-Wesley, Redwood City, CA, 1988), pp. 46 and 88.

9. C. J. Randall, J. R. Albritton, and J. J. Thomson, Phys. Fluids **24**, 1474 (1981).

10. R. C. Malone, R. L. McCrory, and R. L. Morse, Phys. Rev. Lett. **34**, 721 (1975).

11. V. N. Goncharov, T. C. Sangster, P. B. Radha, R. Betti, T. R. Boehly, T. J. B. Collins, R. S. Craxton, J. A. Delettrez, R. Epstein, V. Yu. Glebov, S. X. Hu, I. V. Igumenshchev, J. P. Knauer, S. J. Loucks, J. A. Marozas, F. J. Marshall, R. L. McCrory, P. W. McKenty, D. D. Meyerhofer, S. P. Regan, W. Seka, S. Skupsky, V. A. Smalyuk, J. M. Soures, C. Stoeckl, D. Shvarts, J. A. Frenje, R. D. Petrasso, C. K. Li, F. Séguin, W. Manheimer, and D. G. Colombant, Phys. Plasmas **15**, 056310 (2008).

12. W. Seka, D. H. Edgell, J. P. Knauer, J. F. Myatt, A. V. Maximov, R. W. Short, T. C. Sangster, C. Stoeckl, R. E. Bahr, R. S. Craxton, J. A. Delettrez, V. N. Goncharov, I. V. Igumenshchev, and D. Shvarts, Phys. Plasmas **15**, 056312 (2008).

13. I. V. Igumenshchev, D. H. Edgell, V. N. Goncharov, J. A. Delettrez, A. V. Maximov, J. F. Myatt, W. Seka, A. Shvydky, S. Skupsky, and C. Stoeckl, Phys. Plasmas **17**, 122708 (2010).

14. J. Myatt, A. V. Maximov, W. Seka, R. S. Craxton, and R. W. Short, Phys. Plasmas **11**, 3394 (2004).

15. J. Delettrez, R. Epstein, M. C. Richardson, P. A. Jaanimagi, and B. L. Henke, Phys. Rev. A **36**, 3926 (1987).

16. P. Michel *et al.*, Phys. Rev. Lett. **102**, 025004 (2009).

17. R. A. Lerche, D. W. Phillion, and G. L. Tietbohl, Rev. Sci. Instrum. **66**, 933 (1995).

18. D. T. Michel, C. Sorce, R. Epstein, N. Whiting, I. V. Igumenshchev, R. Jungquist, and D. H. Froula, "Shell Trajectory Measurements from Direct-Drive Experiments," submitted to Review of Scientific Instruments.

19. P. B. Radha, C. Stoeckl, V. N. Goncharov, J. A. Delettrez, D. H. Edgell, J. A. Frenje, I. V. Igumenshchev, J. P. Knauer, J. A. Marozas, R. L. McCrory, D. D. Meyerhofer, R. D. Petrasso, S. P. Regan, T. C. Sangster, W. Seka, and S. Skupsky, Phys. Plasmas **18**, 012705 (2011).

20. D. H. Edgell, W. Seka, J. A. Delettrez, R. S. Craxton, V. N. Goncharov, I. V. Igumenshchev, J. Myatt, A. V. Maximov, R. W. Short, T. C. Sangster, and R. E. Bahr, Bull. Am. Phys. Soc. **52**, 195 (2007); *ibid.* **53**, 168 (2008); *ibid*. **54**, 145 (2009).

21. W. Seka, D. H. Froula, D. H. Edgell, J. F. Myatt, R. W. Short, I. V. Igumenshchev, V. N. Goncharov, and A. V. Maximov, Bull. Am. Phys. Soc. **56**, 327 (2011).

22. V. N. Goncharov, T. C. Sangster, R. Epstein, S. X. Hu, I. V. Igumenshchev, D. H. Froula, R. L. McCrory, D. D. Meyerhofer, P. B. Radha, W. Seka, S. Skupsky, C. Stoeckl, D. T. Casey, J. A. Frenje, and R. D. Petrasso, Bull. Am. Phys. Soc. **56**, 240 (2011).

23. A. V. Maximov, J. F. Myatt, R. W. Short, I. V. Igumenshchev, D. H. Edgell, and W. Seka, Bull. Am. Phys. Soc. **56**, 328 (2011).

24. D. Keller, T. J. B. Collins, J. A. Delettrez, P. W. McKenty, P. B. Radha, B. Whitney, and G. A. Moses, Bull. Am. Phys. Soc. **44**, 37 (1999).

25. D. H. Froula, I. V. Igumenshchev, D. T. Michel, D. H. Edgell, R. Follett, V. Yu. Glebov, V. N. Goncharov, J. Kwiatkowski, F. J. Marshall, P. B. Radha, W. Seka, C. Sorce, S. Stagnitto, C. Stoeckl, and T. C. Sangster, "Increasing Hydrodynamic Efficiency by Reducing Cross-Beam Energy Transfer in Direct-Drive Implosion Experiments," submitted to Physical Review Letters.

26. Y. Lin, T. J. Kessler, and G. N. Lawrence, Opt. Lett. **20**, 764 (1995).

27. T. R. Boehly, V. A. Smalyuk, D. D. Meyerhofer, J. P. Knauer, D. K. Bradley, R. S. Craxton, M. J. Guardalben, S. Skupsky, and T. J. Kessler, J. Appl. Phys. **85**, 3444 (1999).

28. S. P. Regan, J. A. Marozas, J. H. Kelly, T. R. Boehly, W. R. Donaldson, P. A. Jaanimagi, R. L. Keck, T. J. Kessler, D. D. Meyerhofer, W. Seka, S. Skupsky, and V. A. Smalyuk, J. Opt. Soc. Am. B **17**, 1483 (2000).

29. S. Chandrasekhar, *Hydrodynamic and Hydromagnetic Stability*, International Series of Monographs on Physics (Dover Publications, New York, 1981), p. 428.

30. P. Michel *et al.*, Phys. Plasmas **17**, 056305 (2010).

31. E. A. Williams, R. L. Berger, R. P. Drake, A. M. Rubenchik, B. S. Bauer, D. D. Meyerhofer, A. C. Gaeris, and T. W. Johnston, Phys. Plasmas **2**, 129 (1995).

32. T. Dewandre, J. R. Albritton, and E. A. Williams, Phys. Fluids **24**, 528 (1981).

33. E. A. Williams, B. I. Cohen, L. Divol, M. R. Dorr, J. A. Hittinger, D. E. Hinkel, A. B. Langdon, R. K. Kirkwood, D. H. Froula, and S. H. Glenzer, Phys. Plasmas **11**, 231 (2004).

Time-Resolved Measurements of Hot-Electron Equilibration Dynamics in High-Intensity Laser Interactions with Thin-Foil Solid Targets

High-intensity laser interactions with solid targets generate extreme states of matter[1] with unique energy-transport properties.[2,3] At laser intensities above 10^{18} W/cm^2, high-current electron beams with ~MeV energies are generated,[4–7] heating matter to high thermal temperatures over picosecond time scales.[2,3,8] Understanding the energy partition and its evolution in these highly nonequilibrium plasmas is an important open issue, underpinning applications in high-energy-density science,[1] plasma-based particle acceleration,[9] warm, dense matter,[10] high-peak-power γ-ray generation,[11] and advanced inertial fusion energy concepts, including fast ignition.[12] In these conditions, the hot-electron equilibration dynamics are not completely understood, and accurate time-resolved measurements are required to test energy partition and temperature equilibration models.

The only previous hot-electron equilibration data in this regime are the time-resolved K_α-emission data of Chen *et al.*[13] In these experiments thin-foil targets were irradiated with ~0.5-ps pulses focused to intensities up to 10^{19} W/cm^2, and the K_α-emission pulse width was used to characterize the time scale for energy thermalization ("relaxation") between hot and cold electrons. The data showed K_α-emission pulse widths from ~12 to 16 ps. The data were compared to an electron-energy–transfer model that included ion-front expansion and collisional electron-energy transfer based on the Landau–Spitzer theory.[14] With increasing laser intensity, the model did not reproduce the rise time (~10 ps) or the duration of the measured K_α signals, revealing an incomplete picture of the hot-electron equilibration dynamics.

In this article, ultrafast measurements of the hot-electron relaxation time in high-intensity laser–solid interactions are reported. Thin-foil targets were irradiated with 0.5- to 1-ps pulses focused to intensities from ~10^{18} to 10^{19} W/cm^2 and the hot-electron equilibration dynamics studied with time-resolved K_α spectroscopy. In these interactions, the full width at half maximum (FWHM) of the K_α signal increased with laser intensity from ~3 to 6 ps. These are the first experiments at relativistic laser intensities to show rapid hot-electron relaxation times with K_α-emission pulse widths up to a factor of 4× shorter than in previously reported experiments.[13] To provide insight into the mean energy of the hot electrons contained inside the target, the duration of the measured K_α signals were compared to predictions from a collisional energy-transfer model. Assuming collisional energy transfer dominates, the data suggest that hot electrons with mean energies from ~0.8 to 2 MeV are contained inside the target. The inferred mean hot-electron energies are broadly consistent with ponderomotive scaling[6] over the relevant intensity range.

The experiments were carried out with LLE's Multi-Terawatt (MTW) laser.[15] Figure 129.18 shows a schematic of the experimental setup. The MTW laser delivered 1- to 10-J, 0.5- to 1-ps pulses at a wavelength of 1.053 μm that were focused by an f/3 off-axis parabolic mirror to a spot with a FWHM of ~5 μm, providing vacuum-focused intensities from ~10^{18} to 10^{19} W/cm^2. The laser-intensity contrast was ~10^8 at 100 ps before the peak of the main laser pulse.[16] The laser was focused at normal incidence on 500 × 500 × 20-μm^3 Cu-foil targets mounted on 17-μm-diam silicon carbide stalks.

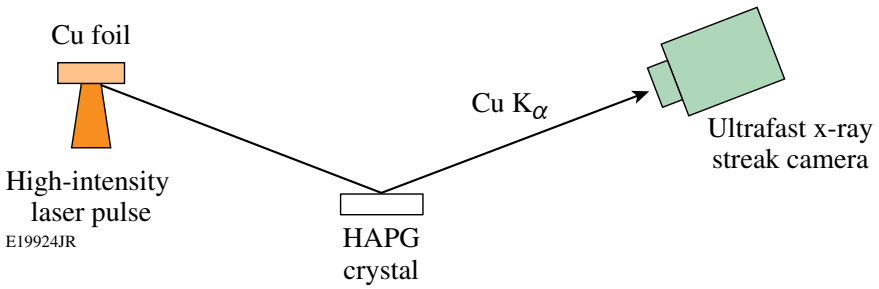

Figure 129.18
Experimental setup. HAPG: highly annealed pyrolytic graphite.

Time resolving the K_α radiation generated in these experiments is a direct technique for inferring the hot-electron relaxation time.[13] K_α radiation emitted from the target was measured with a 2-ps time-resolution x-ray streak camera[17] coupled to a HAPG (highly annealed pyrolytic graphite) crystal spectrometer. The HAPG crystal was toroidally curved and collected radiation from 7.8 to 8.5 keV. This spectral range covers the $2p \rightarrow 1s$ transition in Cu, allowing for time-resolved Cu K_α measurements at 8.05 keV.

The streak camera was independently characterized by direct illumination of the photocathode with a 10-mJ, 0.5-ps pulse of 263-nm light. Figure 129.19 shows a schematic of the setup. By passing half of the UV beam through a quartz plate of known thickness, two pulses were generated, providing a sweep-speed calibration. Figure 129.19(b) shows a typical streak-camera trace for these two pulses. The pulse widths (FWHM) are 1.8±0.1 and 1.9±0.1 ps. Temporal dispersion in the streak camera gives a slightly different impulse response for x-ray illumination. Monte Carlo modeling of the electron optics inside the streak tube shows that this offset is ~0.2 ps, giving an impulse response for x rays of ~2 ps.

Figure 129.20 shows an example of time-resolved plasma x-ray emission data for different high-intensity laser irradiation conditions. Figure 129.20(a) shows the time-resolved K_α emission from a $500 \times 500 \times 20$-μm^3 Cu foil irradiated with a 0.9-J, 0.6-ps pulse focused to 3.6×10^{18} W/cm^2. The pulse width is 3.0±0.2 ps. Figure 129.20(b) shows the K_α emission from a similar target irradiated with an 8.5-J, 0.8-ps pulse focused to 2.9×10^{19} W/cm^2. The pulse width is 5.5±0.1 ps. The K_α emission from these targets was measured as a peaked signal with a sharp rise and a slower decay. The signal rise time did not vary with laser intensity and was determined by the experimental resolution. The signal decay time increased with laser intensity and was sensitive to the hot-electron equilibration dynamics.

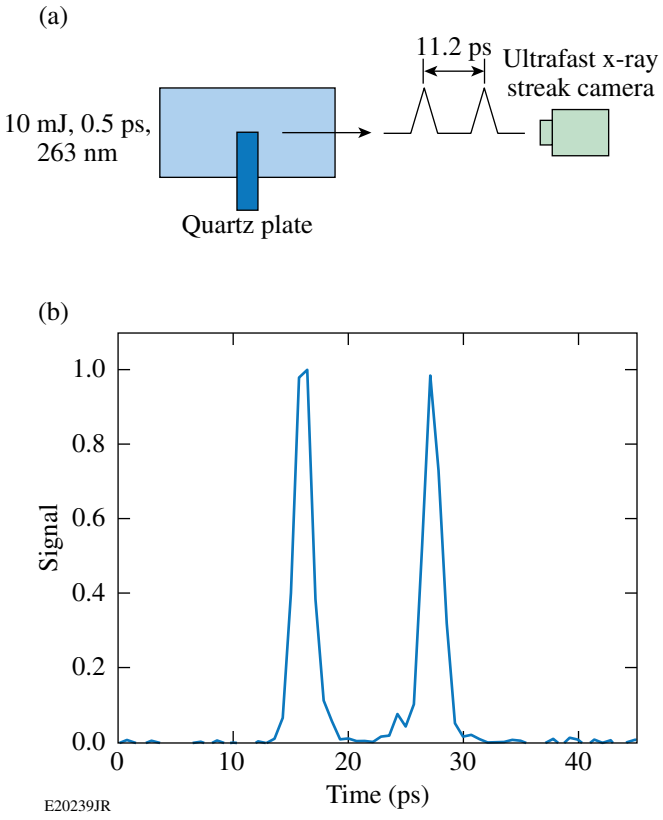

Figure 129.19
(a) Streak-camera calibration setup. (b) Streak-camera response measurement with 0.5-ps, 263-nm pulses showing pulse widths of 1.8±0.1 and 1.9±0.1 ps.

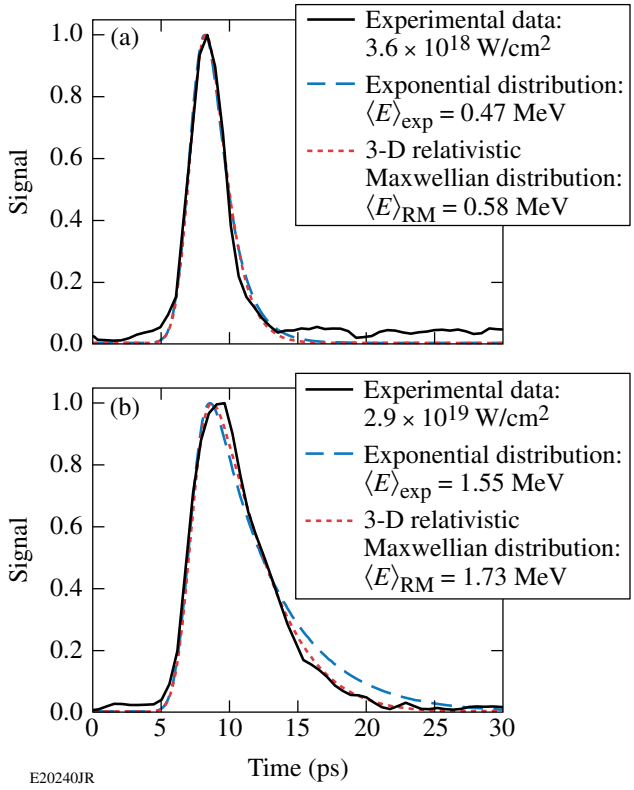

Figure 129.20
Experimental time-resolved K_α emission data from $500 \times 500 \times 20$-μm^3 Cu foils. The targets were irradiated with (a) a 0.9-J, 0.6-ps pulse and (b) an 8.7-J, 0.8-ps pulse. The data are shown with theoretical fits based on a collisional energy-loss model with exponential (blue dashed line) and 3-D relativistic Maxwellian (red dashed line) hot-electron energy distributions.

K_α radiation was generated in these experiments by hot electrons that were confined by target charging.[7,18,19] The thin-foil targets rapidly charge because of the electrostatic potential that develops after the initial loss of a small fraction of high-energy electrons.[18] The remaining hot electrons (>90% of the total laser-accelerated population) make multiple round-trips of the target as they recirculate (reflux) because their collisional range is several hundred microns at solid density.[20]

A collisional energy-loss model for understanding hot-electron relaxation and the time dependence of K_α emission in these targets has been developed. The model calculates the K_α emission rate for a given hot-electron energy distribution, assuming that all of the electrons are trapped inside the foil. The hot-electron energy loss rate is given by[20]

$$\frac{\mathrm{d}E}{\mathrm{d}t} = -\frac{n_\mathrm{e} e^4 L_\mathrm{d}}{4\pi\epsilon_0^2 m_\mathrm{e} v}, \tag{1}$$

where n_e is the electron density for solid Cu (2.46×10^{24} cm^{-3}), E is the hot-electron energy, m_e is the electron rest mass, v is the hot-electron velocity, e is the electron charge, and ϵ_0 is the permittivity of free space. The stopping number L_d (or "log Λ") depends weakly on material and the hot-electron energy, with values for Cu taken from Ref. 21. The time spent by hot electrons outside the target during recirculation is assumed negligible, and energy losses to ion acceleration and self-generated electric fields are not considered in this model.[7,18,19]

K_α-emission pulse widths have been calculated for hot electrons with exponential

$$\left(f_\mathrm{h} \propto e^{-\gamma m_\mathrm{e} c^2 / k_\mathrm{B} T_\mathrm{h}}\right)$$

and three-dimensional relativistic Maxwellian

$$\left[f_\mathrm{h} \propto \gamma\left(\gamma^2 - 1\right)^{1/2} e^{-\gamma m_\mathrm{e} c^2 / k_\mathrm{B} T_\mathrm{h}}\right]$$

energy distributions, where k_B is Boltzmann's constant, T_h is the hot-electron temperature, and γ is the Lorentz factor. Isochoric energy transfer to solid matter in these calculations is assumed. The K_α-emission rate is proportional to the Cu ion density, the time-varying number of hot electrons, and the parameter $\langle \sigma_\mathrm{K} v \rangle$ averaged over the hot-electron energy distribution, where σ_K is the K-shell ionization cross section and v is the hot-electron velocity. The cross section for ionization of K-shell electrons was taken from Ref. 21.

Figure 129.20 shows synthetic K_α streaks that were calculated from this model. The synthetic pulse widths represent a convolution of the calculated K_α-emission rate with the laser pulse duration and the temporal resolution of the x-ray streak camera. In the low-intensity case [Fig. 129.20(a)], the model predicts well the K_α emission pulse shape, independent of the hot-electron energy distribution that was used. The best fit of the experimental data was obtained with the parameters $\langle E \rangle_\mathrm{exp} = 0.47$ MeV for the exponential energy distribution and $\langle E \rangle_\mathrm{RM} = 0.58$ MeV for the three-dimensional (3-D) relativistic Maxwellian energy distribution. In the high-intensity case [Fig. 129.20(b)], the best fit was obtained with the parameters $\langle E \rangle_\mathrm{exp} = 1.55$ MeV and $\langle E \rangle_\mathrm{RM} = 1.73$ MeV. In this case, the K_α-emission pulse shape was better reproduced by model calculations with a 3-D relativistic Maxwellian energy distribution.

Figure 129.21 shows the variation with increasing laser intensity of the measured K_α emission pulse width. An upper estimate of the true K_α-emission pulse width was obtained by accounting for instrumental effects, subtracting the FWHM of the impulse response function from the streak-camera trace in quadrature. Gaussian pulse shapes are assumed. For laser intensities between 2.7×10^{18} and 3.4×10^{19} W/cm^2, the duration of the measured K_α signal increases from ~3 to 6 ps. Over this intensity range, the K_α-emission pulse width increases with

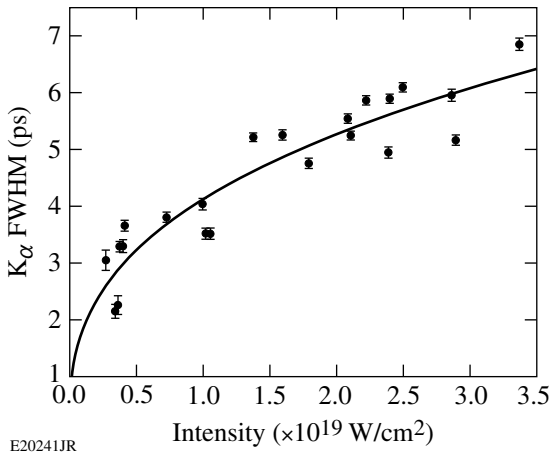

Figure 129.21
Experimental K_α-emission pulse width as a function of laser intensity. The pulse widths have been adjusted to account for the impulse response of the streak camera.

laser intensity and is given by $\tau_{K_\alpha}[\text{ps}] = (4.1 + 0.3) I_{19}^{0.35\pm0.07}$, where I_{19} is the laser intensity in units of 10^{19} W/cm^2.

To obtain a mean hot-electron energy scaling, these data are compared with the collisional energy-loss model. Figure 129.22(a) shows the relationship between the calculated K_α-emission pulse width and the mean hot-electron energy for exponential and 3-D relativistic Maxwellian energy distributions. In these calculations, the K_α-emission rate was convolved with a 0.8-ps FWHM Gaussian pulse that approximated the range of laser pulse durations that were used in these experiments. The synthetic pulse was convolved with a 2-ps FWHM Gaussian instrument response that was removed in quadrature for comparison with the experimental data (Fig. 129.21). Figure 129.22(a) shows that calculations with a 3-D relativistic Maxwellian energy distribution have slightly higher mean hot-electron energies than with an exponential energy distribution for a given K_α-emission pulse width. This offset is ~100 to 200 keV.

Figure 129.22(b) shows the mean hot-electron energies that are inferred from the experimental data based on this model. Two scaling laws were obtained: For an exponential energy distribution, $\langle E \rangle_{\text{exp}}[\text{MeV}] = (1.12\pm0.11) I_{19}^{0.51\pm0.11}$. For a 3-D relativistic Maxwellian energy distribution, $\langle E \rangle_{\text{RM}} = [\text{MeV}] = (1.19\pm0.11) I_{19}^{0.46\pm0.10}$. Assuming collisional energy transfer dominates, these results show that mean hot-electron energies from ~0.8 to 2 MeV are required to generate K_α-emission pulse widths consistent with the experimental observations.

Figure 129.22(c) compares these inferred mean hot-electron energies with ponderomotive scaling.[6] Ponderomotive scaling gives

$$\langle E \rangle = m_e c^2 \left[1 + \left(2U_p / m_e c^2 \right) \right]^{1/2},$$

where $U_p = 9.33 \times 10^{-14} I\,[\text{W/cm}^2]\,(\lambda\,[\mu\text{m}])^2$ is the ponderomotive potential. In general, good agreement was found. The best agreement was found for calculations with an exponential energy distribution. A similar scaling predicting ~100- to 200-keV-higher mean hot-electron energies was found with calculations using the 3-D relativistic Maxwellian energy distribution.

Including the energy-transfer model energy loss to self-generated fields and ion acceleration would increase the inferred mean hot-electron energy and lead to a faster increase in the K_α-emission pulse width with laser intensity since these effects are expected to be greater at higher intensities. In the limit of isochoric energy transfer, additional energy loss mechanisms will increase the mean hot-electron energy required to gen-

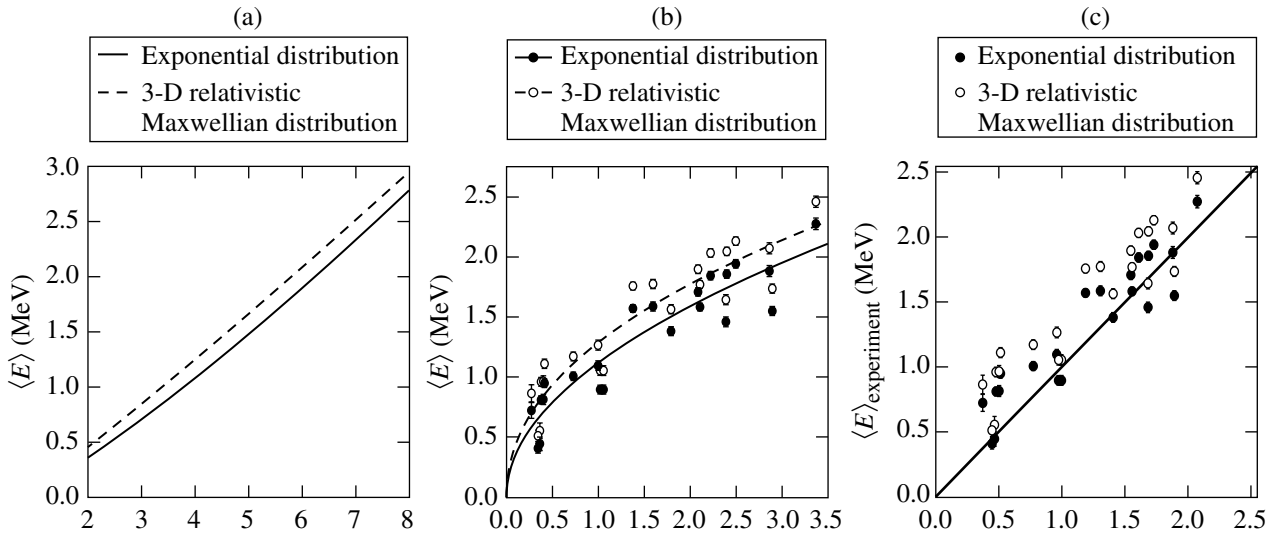

Figure 129.22
(a) Calculated mean hot-electron energy $\langle E \rangle$ as a function of K_α-emission pulse width based on a 0.8-ps laser-pulse duration. (b) Inferred $\langle E \rangle$ as a function of laser intensity, assuming exponential (solid line) and 3-D relativistic Maxwellian (dashed line) hot-electron energy distributions. (c) Comparison of the experimentally inferred $\langle E \rangle$ with ponderomotive scaling.[6]

erate the experimentally observed K_α emission. These results represent a minimum value for the inferred mean hot-electron energy required to generate the experimentally observed K_α-emission pulse widths.

In summary, the hot-electron equilibration dynamics in thin-foil solid targets irradiated with high-intensity laser pulses have been studied. Time-resolved K_α spectroscopy measurements show K_α-emission pulse widths from ~3 to 6 ps for laser intensities between ~10^{18} and 10^{19} W/cm^2. Assuming collisional energy transfer dominates, the experimental data suggest that hot electrons with mean energies from ~0.8 to 2 MeV are contained inside the target. The inferred mean hot-electron energy scaling with laser intensity is broadly consistent with ponderomotive scaling. These findings are important for the understanding of a wide range of high-energy-density physics applications that require a large and fast energy input into matter.

ACKNOWLEDGMENT

This work was supported by the U.S. Department of Energy Office of Inertial Confinement Fusion under Cooperative Agreement No. DE-FC52-08NA28302, the University of Rochester, and the New York State Energy Research and Development Authority. The support of DOE does not constitute an endorsement by DOE of the views expressed in this article.

REFERENCES

1. B. A. Remington *et al.*, Science **284**, 1488 (1999).
2. J. A. Koch *et al.*, Phys. Rev. E **65**, 016410 (2001); K. Eidmann *et al.*, J. Quant. Spectrosc. Radiat. Transf. **81**, 133 (2003); P. Audebert *et al.*, Phys. Rev. Lett. **94**, 025004 (2005).
3. C. R. D. Brown *et al.*, Phys. Rev. Lett. **106**, 185003 (2011).
4. D. F. Price *et al.*, Phys. Rev. Lett. **75**, 252 (1995); H. Chen, B. Soom, B. Yaakobi, S. Uchida, and D. D. Meyerhofer, Phys. Rev. Lett. **70**, 3431 (1993); K. B. Wharton *et al.*, Phys. Rev. Lett. **81**, 822 (1998); K. Yasuike *et al.*, Rev. Sci. Instrum. **72**, 1236 (2001); S. P. Hatchett *et al.*, Phys. Plasmas **7**, 2076 (2000).
5. F. N. Beg *et al.*, Phys. Plasmas **4**, 447 (1997).
6. S. C. Wilks *et al.*, Phys. Rev. Lett. **69**, 1383 (1992).
7. P. M. Nilson, A. A. Solodov, J. F. Myatt, W. Theobald, P. A. Jaanimagi, L. Gao, C. Stoeckl, R. S. Craxton, J. A. Delettrez, B. Yaakobi, J. D. Zuegel, B. E. Kruschwitz, C. Dorrer, J. H. Kelly, K. U. Akli, P. K. Patel, A. J. Mackinnon, R. Betti, T. C. Sangster, and D. D. Meyerhofer, Phys. Rev. Lett. **105**, 235001 (2010).
8. A. Saemann *et al.*, Phys. Rev. Lett. **82**, 4843 (1999); P. Audebert *et al.*, Phys. Rev. Lett. **89**, 265001 (2002).
9. E. L. Clark *et al.*, Phys. Rev. Lett. **84**, 670 (2000); R. A. Snavely *et al.*, Phys. Rev. Lett. **85**, 2945 (2000).
10. P. K. Patel *et al.*, Phys. Rev. Lett. **91**, 125004 (2003).
11. P. A. Norreys *et al.*, Phys. Plasmas **6**, 2150 (1999).
12. M. H. Key, M. D. Cable, T. E. Cowan, K. G. Estabrook, B. A. Hammel, S. P. Hatchett, E. A. Henry, D. E. Hinkel, J. D. Kilkenny, J. A. Koch, W. L. Kruer, A. B. Langdon, B. F. Lasinski, R. W. Lee, B. J. MacGowan, A. MacKinnon, J. D. Moody, M. J. Moran, A. A. Offenberger, D. M. Pennington, M. D. Perry, T. J. Phillips, T. C. Sangster, M. S. Singh, M. A. Stoyer, M. Tabak, G. L. Tietbohl, M. Tsukamoto, K. Wharton, and S. C. Wilks, Phys. Plasmas **5**, 1966 (1998); M. Tabak *et al.*, Phys. Plasmas **1**, 1626 (1994).
13. H. Chen *et al.*, Phys. Rev. E **76**, 056402 (2007).
14. L. D. Landau, Phys. Z. Sowjetunion **10**, 154 (1936); L. Spitzer, *Physics of Fully Ionized Gases*, 2nd rev. ed., Interscience Tracts on Physics and Astronomy (Wiley Interscience, New York, 1962).
15. V. Bagnoud, I. A. Begishev, M. J. Guardalben, J. Puth, and J. D. Zuegel, Opt. Lett. **30**, 1843 (2005).
16. V. Bagnoud, J. D. Zuegel, N. Forget, and C. Le Blanc, Opt. Express **15**, 5504 (2007).
17. C. Stoeckl, W. Theobald, P. A. Jaanimagi, P. Nilson, M. Storm, J. A. Delettrez, R. Epstein, T. C. Sangster, D. Hey, A. J. MacKinnon, H.-S. Park, P. K. Patel, R. Shepherd, J. Green, K. L. Lancaster, and P. A. Norreys, Bull. Am. Phys. Soc. **52**, 67 (2007).
18. J. Myatt, W. Theobald, J. A. Delettrez, C. Stoeckl, M. Storm, T. C. Sangster, A. V. Maximov, and R. W. Short, Phys. Plasmas **14**, 056301 (2007).
19. A. J. Mackinnon *et al.*, Phys. Rev. Lett. **88**, 215006 (2002); Y. Sentoku *et al.*, Phys. Plasmas **10**, 2009 (2003); W. Theobald, K. Akli, R. Clarke, J. Delettrez, R. R. Freeman, S. Glenzer, J. Green, G. Gregori, R. Heathcote, N. Izumi, J. A. King, J. A. Koch, J. Kuba, K. Lancaster, A. J. MacKinnon, M. Key, C. Mileham, J. Myatt, D. Neely, P. A. Norreys, H.-S. Park, J. Pasley, P. Patel, S. P. Regan, H. Sawada, R. Shepherd, R. Snavely, R. B. Stephens, C. Stoeckl, M. Storm, B. Zhang, and T. C. Sangster, Phys. Plasmas **13**, 043102 (2006); S. D. Baton *et al.*, High Energy Density Phys. **3**, 358 (2007); P. M. Nilson, W. Theobald, J. Myatt, C. Stoeckl, M. Storm, O. V. Gotchev, J. D. Zuegel, R. Betti, D. D. Meyerhofer, and T. C. Sangster, Phys. Plasmas **15**, 056308 (2008); P. M. Nilson, W. Theobald, J. F. Myatt, C. Stoeckl, M. Storm, J. D. Zuegel, R. Betti, D. D. Meyerhofer, and T. C. Sangster, Phys. Rev. E **79**, 016406 (2009).
20. H. O. Wyckoff, *ICRU Report*, International Commission on Radiation Units and Measurements, Inc., Bethesda, MD (1984).
21. J. P. Santos, F. Parente, and Y.-K. Kim, J. Phys. B: At. Mol. Opt. Phys. **36**, 4211 (2003).

Experimental Studies of the Two-Plasmon-Decay Instability in Long-Scale-Length Plasmas

Introduction

Direct-drive inertial confinement fusion (ICF) is an encouraging path to high-gain inertial fusion energy.[1] In the direct-drive approach to ICF, high-power, moderate-intensity laser beams ($\sim 7 \times 10^{14}$ W/cm^2) produce and propagate through a high-temperature ($T_e \sim 3.5$ keV), long-scale-length ($L_n \sim 500$ μm) underdense plasma prior to depositing energy near the critical surface of a spherical capsule. A series of shocks are launched that adiabatically compress the nuclear fuel to fusion conditions.[2–4] For the most-efficient compression, the shocks are driven on a low adiabat[5] and ignition is susceptible to preheat; heating of the imploding shell by "hot" electrons increases the implosion adiabat, reducing the compression efficiency.

Electrons can be accelerated to high energies by two-plasmon-decay (TPD) instability[6] in which the incident electromagnetic wave decays into two electron-plasma waves.[7–9] The instability grows rapidly through the resonant coupling of the electric field of the incident laser beam and the longitudinal electrostatic field of the two electron-plasma waves. The dependence of TPD on the hydrodynamic conditions is evident in the convective (intensity) gain exponent for the instability of a single-plane electromagnetic wave [$G_{SB} \simeq 1.9 \times 10^{-2}\, I_s\, (\times 10^{14}\ \mathrm{W/cm^2})\, L_n\, (\mu\mathrm{m}) \big/ T_e(\mathrm{keV})$, where I_s is the single-beam intensity, L_n is the density scale length, T_e is the electron temperature, and all parameters are taken at $n_{cr}/4$, $n_{cr} \simeq 10^{22}$ cm^{-3}] (Ref. 10). Simulations based on a nonlinear Zakharov model[11] that includes test particles, indicate that electrons are stochastically accelerated to high energies (>50 keV) by enhanced electron-plasma waves. Once above threshold, the hot-electron temperature is shown to scale with $I_q L_n / T_e$ (Ref. 12), where I_q is the overlapped intensity at quarter critical.

Early experiments using CO_2 lasers measured the first hot electrons generated by TPD[13] and the associated electron-plasma waves using Thomson scattering.[14] More-recent experiments focusing on TPD in direct-drive–ignition conditions[15] demonstrated that the efficiency of hot-electron generation scaled with overlapped laser-beam intensity.[16] These studies showed a nearly constant electron temperature and saturation of the hot-electron generation at 0.1% of the incident laser energy when plotted as a function of the vacuum laser intensity.[17] This apparent saturation and low level of electron generation were results of the hydrodynamics; the small laser spots used to produce the highest intensities limited the scale length to less than $L_n < 200$ μm.

The work presented in this article uses the large laser spots and high ultraviolet intensities available on OMEGA EP[18] to produce a 400-μm-long-scale-length, 2.5-keV plasma, where $I_q L_n / T_e$ is increased by nearly a factor of 4 when the laser intensity is varied from 1.3 to 7×10^{14} W/cm^2. Over this range in intensities, a rapid increase in the hot-electron temperature (25 keV to 90 keV) is measured and for intensities above 3.5×10^{14} W/cm^2 the hot-electron efficiency generation is saturated at a nearly constant level of ~1% of the incident laser energy.[19] The rapid increase in hot-electron temperature is compared with simulations that use a Zakharov model designed to provide a physics-based predictive capability for TPD at ignition conditions.[20]

Experimental Setup

1. Target and Laser Configuration

The experimental configuration is shown in Fig. 129.23, where the long-scale-length CH plasma was produced by illuminating a 30-μm-thick CH layer deposited on 30 μm of Mo and backed with an additional 30 μm of CH. The CH thickness was chosen to avoid any burnthrough to the Mo layer. This was verified by the fact that no Mo spectral lines were observed except for the inner-shell K lines that were attributed to the TPD hot electrons. The Mo thickness was equal to a range of electrons with a typical energy of ~120 keV, which was confirmed by Monte Carlo simulations that showed that electrons with energies less than 120 keV were stopped within the Mo. This resulted in nearly all of the electrons accelerated by TPD being absorbed in the target.

The 17.5-keV Mo K_α line was sufficiently high in energy to ensure that photoexcitation from the $T_e \simeq 2.5$-keV coronal plasma region did not contribute to the K_α-emission measure-

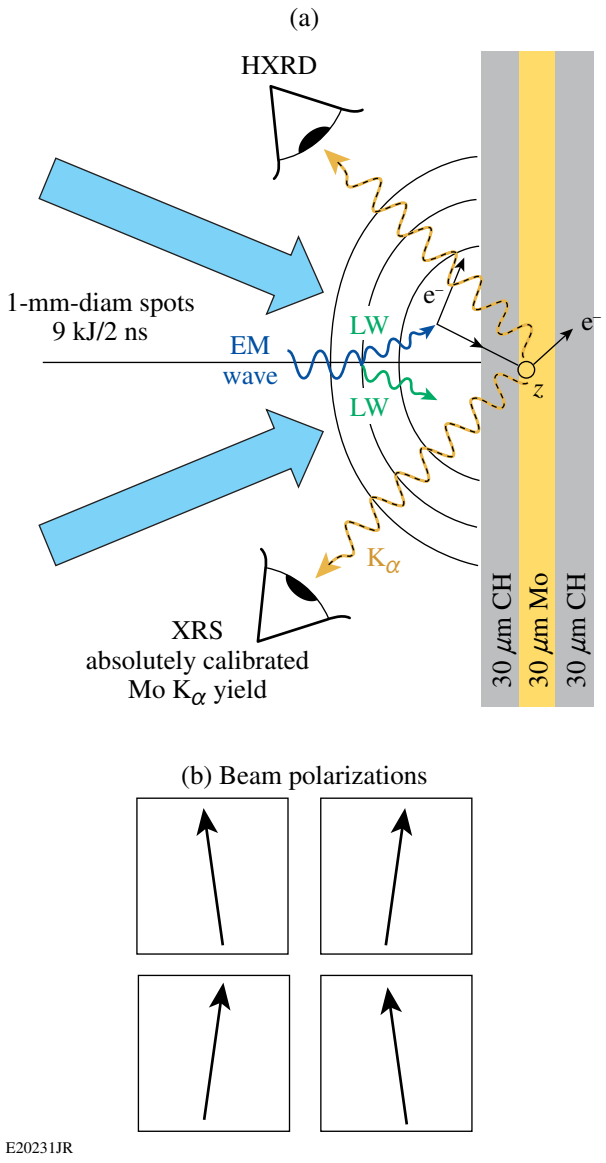

Figure 129.23
(a) The 2-mm × 2-mm target is illuminated by four UV laser beams. The 30-μm-thick Mo is used to capture the majority of the electrons produced by TPD. (b) The polarization of each laser beam is 8° from vertical as shown.

ments. This ensured that the measured K_α emission was a result of K-shell impact and hard x-ray photoionization caused by the hot electrons produced by TPD. This is confirmed by integrating the measured x-ray continuum above the K_α energy [$E(K_\alpha)$ = 17.5 keV] to obtain the total number of x rays (N). Assuming that all x rays are absorbed in the Mo, an upper bound for the contribution of the continuum to the K_α yield is $E_R \cong E(K_\alpha)\,\omega_k N$, where ω_k is the fluorescence yield. Even for the highest laser irradiance, the contribution of the x-ray continuum to the K_α yield is only a few percent of the measured K_α energy; therefore, the radiation contribution is negligible. There is an additional effect of K_α excitation by the bremsstrahlung emitted by the hot electrons; this secondary effect is included in the Monte Carlo–code calculations described in **Diagnostics** (p. 23), which were used to derive the total energy in hot electrons.

For this study, four ultraviolet ($\lambda_0 = 0.35\ \mu$m) beams available from the OMEGA EP Laser System[18] produced the required intensities over a large-diameter laser spot to create 400-μm plasma density scale lengths at $n_{cr}/4$ (Fig. 129.24). A maximum overlapped laser intensity of 7×10^{14} W/cm^2 was achieved using a total energy on target of 8.7 kJ in a 2-ns flattop laser pulse (Fig. 129.24). The four UV beams intersect the target at an angle of 23° with respect to the target normal and are linearly polarized

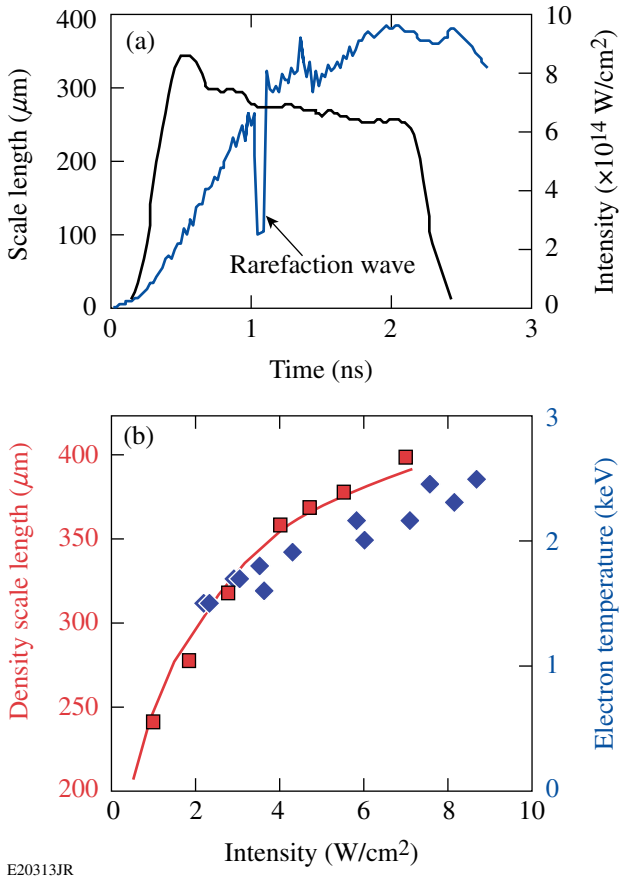

Figure 129.24
(a) The high UV laser power available (P_{max} = 4.5 TW) on OMEGA EP provides the necessary intensity (right axis) over a nearly 1-mm-diam laser spot to produce an electron-density scale length $L_n \simeq 400\ \mu$m. The simulated plasma scale length (left axis) increases to saturation after ~1.5 ns. (b) The maximum simulated density scale length (left axis) and electron temperature (right axis) at quarter critical are shown as a function of the overlapped intensity.

[Fig. 129.23(b)]. Two sets of distributed phase plates (DPP's)[21] were used (840-μm and 890-μm diameter measured at the 1/e intensity points) to produce a combined intensity distribution that has a super-Gaussian profile with a diameter of nearly 1 mm.

Figure 129.25 shows a time-integrated x-ray pinhole image of the focal spot. This radiation is emitted by the laser-heated CH layer and characterizes the interaction region. The x-ray profile in Fig. 129.25(b) has a width (at half-maximum) that is similar to that of the overlapped vacuum laser profile, but the flattop of the latter has been rounded in the x-ray image; this is mainly a result of the lateral heat conduction within the plasma.

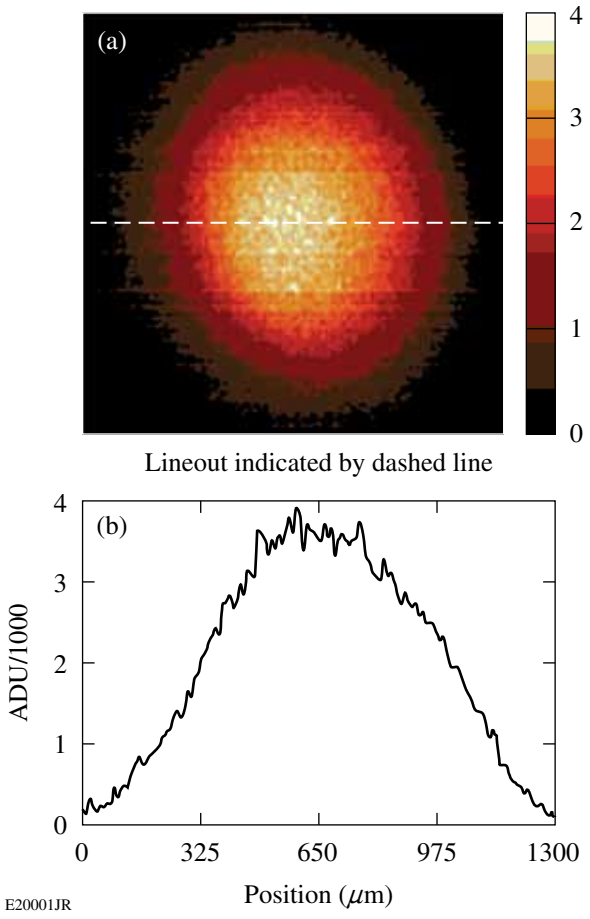

Figure 129.25
(a) X-ray image of the irradiated focal spot at 5×10^{14} W/cm^2 (in the photon-energy range of 2 to 7 keV). (b) This lineout is indicated by the horizontal dashed line in the image in (a).

2. Hydrodynamics

a. Simulations. Two-dimensional hydrodynamic simulations using the codes *SAGE*[22] and *DRACO*[23] show that the maximum-achievable scale length in planar geometry is obtained by maximizing the overlapped-laser-beam intensity while providing enough time for the plasma to reach steady state. Figure 129.24(a) shows that increasing the overlapped-laser-beam intensity increases both the scale length and the electron temperature at quarter critical $\left(L_n/T_e \approx 160\ \mu\text{m/keV}\right)$. Over this intensity range, the hydrodynamic simulations indicate that the intensity of the laser beams at $n_{cr}/4$, where TPD has the largest growth rate, is reduced from the vacuum intensity by ~55%. For the highest laser-beam energies available at 2 ns, the optimal laser spot size is ~1-mm diameter; a further increase in laser-spot size reduces the intensity on target, resulting in a shorter scale length. For the experimental conditions presented here, the scale length reaches a steady state after about 1.5 ns [Fig. 129.24(b)] and the asymptotic scale length is given by $L_n \simeq 250\ \mu\text{m}\ \langle I_{14} \rangle^{1/4}$.

b. X-ray continuum measurements. To check the reliability of the simulations, comparisons were made between calculated and measured plasma conditions at quarter critical and time- and space-integrated x-ray fluence in the energy range of ~5 to 8 keV. This radiation is emitted in the laser-heated CH layer. An example (using *SAGE*) from a shot at an irradiance of 2.7×10^{14} W/cm^2 is shown in Fig. 129.26. No intensity normalization was applied. Even though most of the radiation comes from layers deeper (and colder) than the quarter-critical surface, the ability of the codes to replicate the x-ray fluence in absolute magnitude makes the calculated plasma parameters (such as the TPD threshold below) credible.

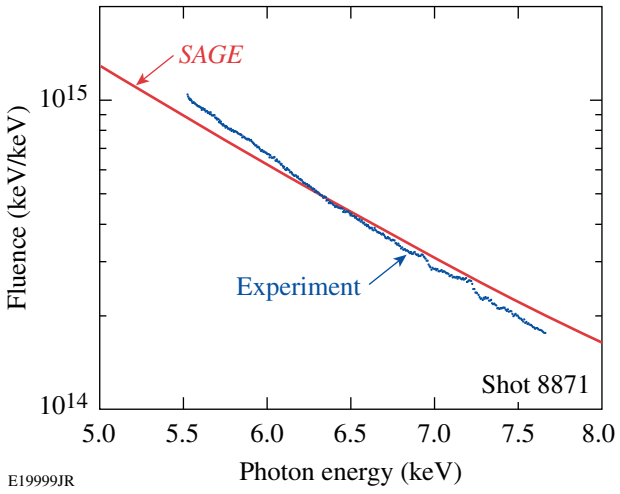

Figure 129.26
SAGE-calculated x-ray fluence from a shot at an irradiance of 2.7×10^{14} W/cm^2. No normalization of intensity was applied.

c. UV Thomson-scattering measurements. A more-rigorous test of the calculated plasma parameters was obtained using

Thomson scattering.[19] Figure 129.27 shows a Thomson-scattering spectrum where the ion-acoustic features are resolved and used to measure the electron and ion temperatures. The measured electron temperature is within a few percent of the simulations [Fig. 129.27(c)].

The rarefaction wave launched from the CH/Mo interface is observed in the Thomson-scattering spectrum 1.11 ns after the laser beams turns on, which is in excellent agreement with the hydrodynamic simulations [Fig. 129.24(a)]. Although the density scale length at quarter critical is not directly measured, the excellent agreement between the measured and simulated time of arrival of the rarefaction wave demonstrates the accuracy of the thermal conduction model and is a strong indication that the calculated density and temperature profiles are accurate.

The Thomson-scattering measurements were obtained on the OMEGA Laser System using the same target platform, pulse shape, and similar laser beam diameters (800-μm FWHM) as used on the OMEGA EP experiments. A 20-J, $\lambda_{4\omega} = 0.26$-μm, *f*/6.7 Thomson-scattering probe beam was focused to a diameter of 60 μm and the Thomson-scattered light was collected from a 60-μm × 75-μm × 75-μm volume located 200 μm from the initial target surface.[24] The Thomson-scattering diagnostic probes ion-acoustic waves propagating nearly parallel to the target [$k_a = 2\, k_{4\omega} \sin(\theta/2)$, where $k_{4\omega} = 2\pi/\lambda_{4\omega}$ and $\theta = 63°$ is the scattering angle].

3. Diagnostics

a. X-ray spectrometer. The determination of total hot-electron energy depends on an absolute calibration of the spectrometers measuring the Mo K_α line (at 17.5 keV). An x-ray spectrometer was used for all shots but checked for consistency on several shots by comparison with a Cauchois-type quartz crystal spectrometer (TCS)[26] and single-hit charge-coupled–device (CCD) array (SPC).[27] The energy in the Mo K_α-emission line (E_{K_α}) was measured using an absolutely calibrated planar LiF crystal spectrometer (XRS) that views the target from the incident laser side at an angle of 63° from the target normal [Fig. 129.23(a)].[28]

The LiF crystal was calibrated by LLE and the quartz crystal at NIST.[29] The CCD array (Spectral Instruments[30] model 800) was calibrated by Maddox *et al.*[31] for several photon energies, including correction for background. XRS and TCS used image plates to record the spectra; calibration data for the same plates and image scanner as used at LLE were published by Meadowcroft *et al.*[32] The results of the three instruments for a single shot at 6.4×10^{14} W/cm^2 are shown in Fig. 129.28. The energy in the Mo K_α line from the XRS and TCS spectra agrees to within 15%; that from TCS agrees with the first two to within 25%. The slightly different spectral resolution of the instruments does not impact the measurement of the total K_α energy. The agreement with the CCD instrument is particularly significant since, unlike the other two spectrometers, it does not use image plates. Figure 129.29 shows that the energy con-

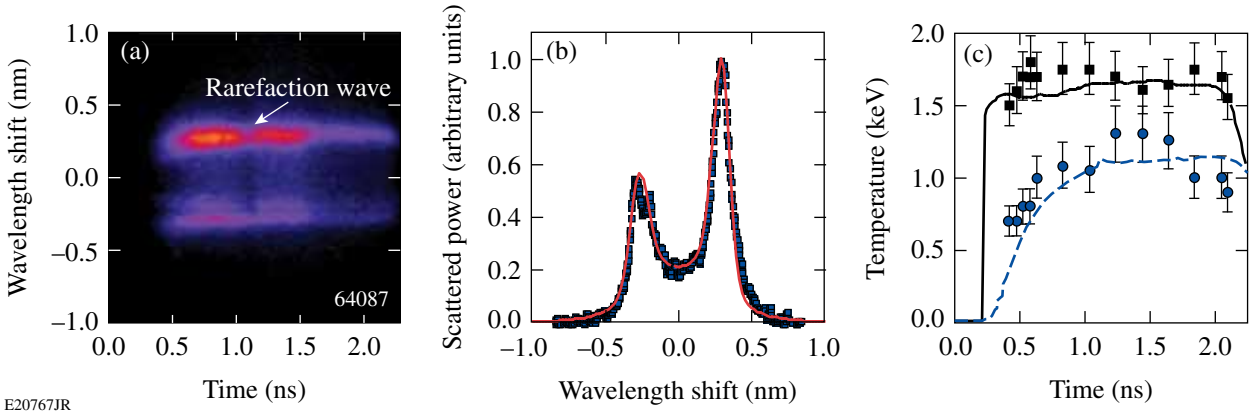

Figure 129.27

(a) Thomson-scattered light from near the quarter critical density for 3ω light is spectrally and temporally resolved to measure the ion-acoustic features. The electron and ion temperatures as a function of time are obtained by fitting the standard dynamic form factor[25] to the measured spectra that are averaged over 50 ps. (b) A best fit (red curve) to the measured spectrum at 0.8 ns (blue) is obtained for $T_e = 1.6$ keV, $T_i = 1.0$ keV. (c) The electron (solid) and ion (dashed) temperatures calculated by *DRACO* compare well to the measurements.

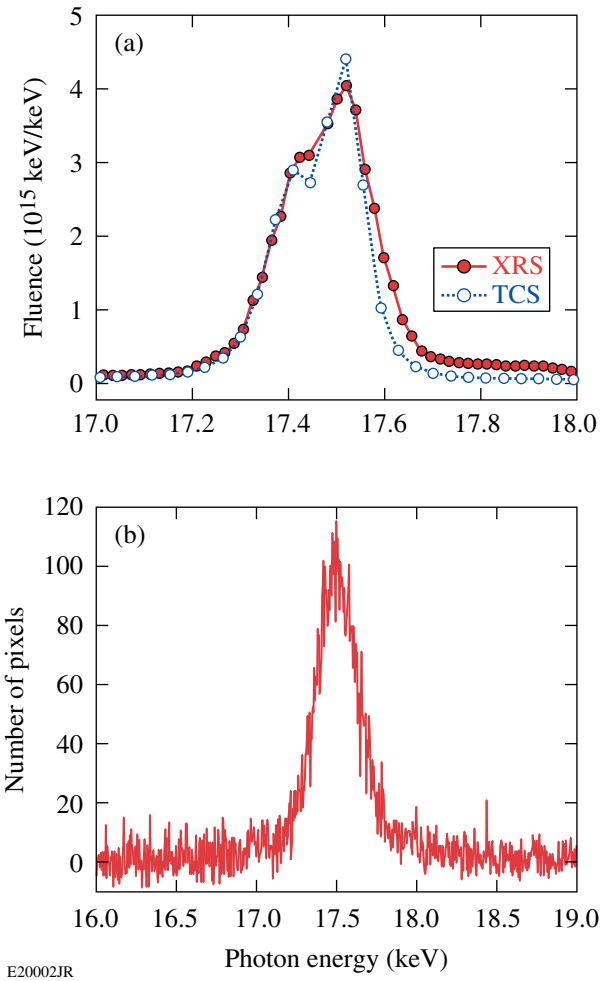

Figure 129.28
An example of the Mo K_α spectra measured on a single shot by three detectors: (a) a planar LiF crystal spectrometer and a Cauchois-type quartz crystal spectrometer and (b) a single-hit CCD array (SPC). The three measurements of K_α energy are consistent.

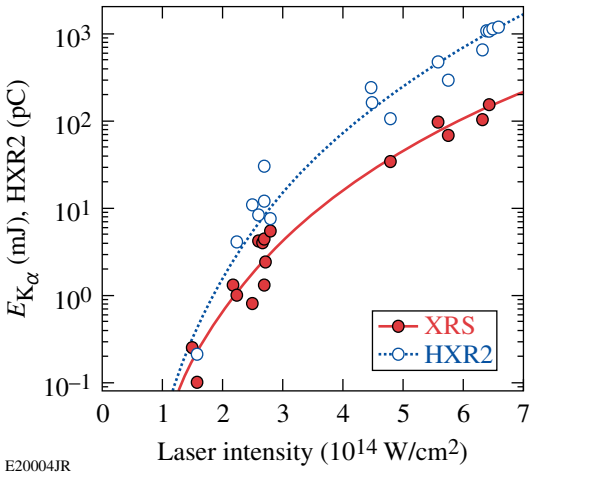

Figure 129.29
Mo K_α and hard x-ray (≳40-keV) yields. Both signals rise rapidly with laser intensity.

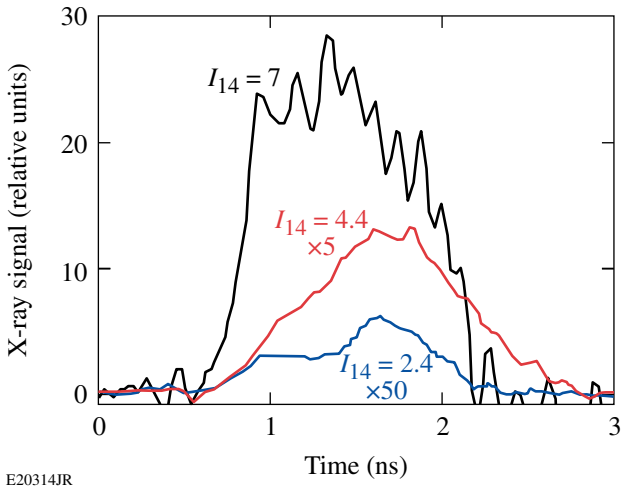

Figure 129.30
The measured hard x-ray emission (>40 keV) is shown for overlapped intensities of 7×10^{14} W/cm^2 (black), 4.4×10^{14} W/cm^2 (red), and 2.4×10^{14} W/cm^2 (blue).

tained within the Mo K_α line scales quasi-exponentially with laser intensity over nearly four orders of magnitude when the vacuum laser intensity is varied from 1.3 to 7×10^{14} W/cm^2.

b. Hard x-ray detector (HXRD). Figure 129.30 shows the hard x-ray emission as a function of time for one of the three x-ray channels used to measure the hot-electron temperature. The hot-electron temperature (T_{hot}) is assumed to be equal to the slope of the hard x-ray radiation that is determined by fitting an exponential decay [$\exp(-E/T_{hot})$] to the measured ratios of the x-ray radiation above ~40 keV, ~60 keV, and ~80 keV obtained using a three-channel scintillator detector (HXRD).[33]

The hard x-ray scaling provides an additional signature of hot-electron generation. Figure 129.29 compares the scaling with laser intensity of the K_α and bremsstrahlung yields. Both signals increase quasi-exponentially by several orders of magnitude, primarily because of the increase in the number of hot electrons. The hard x rays rise faster as a result of the corresponding increase in hot-electron temperature with intensity shown in **Results** (p. 26). This occurs because the bremsstrahlung emission increases with hot-electron temperature, whereas the cross section for Mo K_α excitation decreases with electron energy above ~50 keV.

c. Monte Carlo simulations. Monte Carlo simulations using the code *EGSnrc*[34] are used to relate the measured Mo K_α energy and the HXRD signal to the total energy in hot electrons. For the electron spectra discussed in this article (T_{hot} = 25 to 90 keV), the Monte Carlo simulations indicate that the total electron energy is directly related to the total K_α energy given the hot-electron temperature $E_{electrons}(J) \simeq 150\, E_{K_\alpha}(mJ/sr)/\sqrt{T_{hot}(keV)}$. This relationship is accurate to within 20% over the relevant hot-electron temperature range and is specific to the geometry of the experiment.

The Monte Carlo code calculates both the K_α and the associated bremsstrahlung spectrum (HXR) given an initial electron-beam spectrum. Both the K_α and HXR yields are calculated as functions of the observation angle. To obtain reliable results, 10^7 electrons are typically assumed to be normally incident on the target with a Maxwellian energy distribution at the experimentally determined temperature T_{hot}. The number of calculated K_α photons and HXR photons per energy bin is typically of the order of 10^3; therefore, a statistical precision of a few percent is obtained.

The calculated K_α energy was tested by comparison with experiment. Reference 35 shows extensive measurements of the Cu K_α line from an x-ray tube as a function of emission angle and tube voltage. The corresponding Monte Carlo simulations (assuming a monoenergetic electron beam) agree very closely with Ref. 35. The temperature of the input-electron distribution is taken to be the measured slope of the HXR. Figure 129.31 shows that the two temperatures are essentially the same; for an assumed electron temperature of 80 keV, the HXR slope is 79 keV.

Changing the assumed hot-electron divergence has a small effect on the calculated K_α signal because (a) the range of most electrons is smaller than the Mo thickness, (b) electron scattering changes the initially monodirectional distribution into a quasi-isotropic distribution, and (c) the target is large compared to the focal-spot size. This simplifies the determination of hot-electron generation but also precludes studying the electron divergence, which is important for determining preheat in spherical implosions. A similar situation exists with respect to the HXR radiation. For a low-Z target and unidirectional electrons, the HXR spectrum is peaked in the forward direction. The Monte Carlo–code calculations show that because of electron scattering in the Mo; however, the spectrum becomes quasi-isotropic in intensity and in shape (therefore T_{hot} is uniquely defined). Again, the spectrum is independent of initial electron divergence.

Before comparing the measured and simulated K_α energies, it is necessary to account for the angular dependence of K_α emission. The local emission of K_α is strictly isotropic, but its opacity through the molybdenum creates an angular distribution. Figure 129.32 shows the K_α emission per unit solid angle $\Delta\Omega$ for two hot-electron temperatures. As expected, the distri-

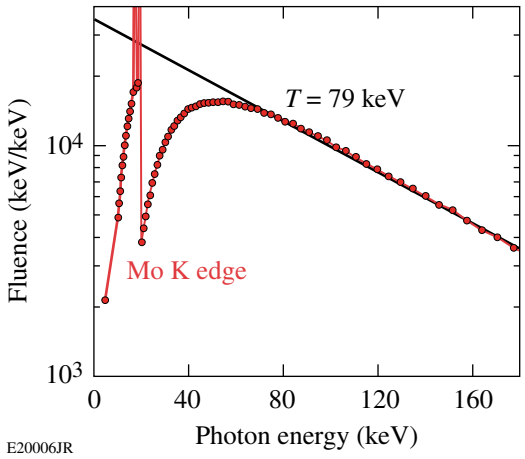

Figure 129.31
Monte Carlo–calculated HXR spectra for 10 million incident electrons. The slope of the HXR continuum (79 keV) is about equal to the hot-electron temperature assumed for the Monte Carlo–code run (80 keV). The smoothness of the curve is an indication of the good statistics obtained with 10 million electrons.

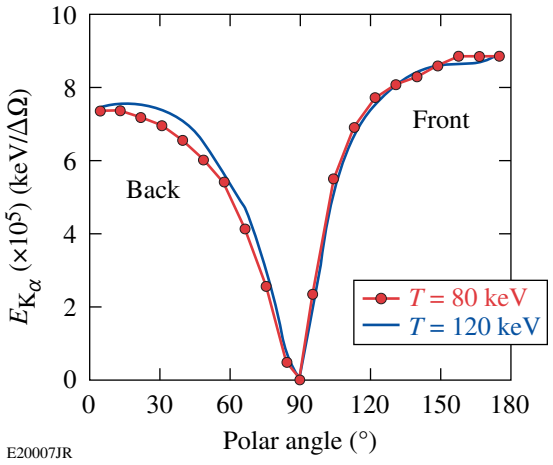

Figure 129.32
Monte Carlo–calculated angular distribution of Mo K_α as function of polar angle θ (relative to the target normal) per unit solid angle. "Back" stands for the back of the target (forward emission).

bution peaks in the forward and backward directions $\theta = 0°$ and $\theta = 180°$, where the K_α opacity is minimal. Figure 129.32 is used to relate the measured K_α emission per unit solid angle to the calculated emission in the direction of the spectrometer. The shape of the angular distribution across the detector is nearly the same for different hot-electron temperatures for the target thickness used in this study.

Based on the K_α yield calculated by the Monte Carlo code, Fig. 129.33 gives the total energy in hot electrons divided by the K_α energy per unit solid angle in the forward direction. Using Fig. 129.33, the measured energy in K_α (Fig. 129.29) can be converted into energy in hot electrons.

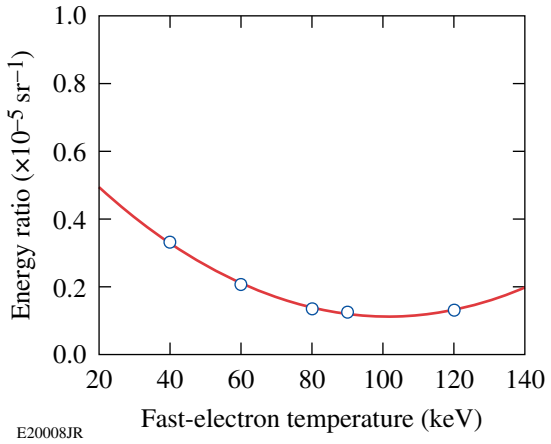

Figure 129.33
Monte Carlo–calculated ratio of the total incident electron energy and the K_α emission per unit solid angle in the target normal direction as a function of the hot-electron temperature. This curve is used to deduce the total energy in hot electrons from the measured Mo K_α energy.

Results

1. Hot-Electron Temperature

Figure 129.34(a) shows that the hot-electron temperature increases from 25 keV to 90 keV as the laser intensity is increased from 2 to 7×10^{14} W/cm^2. These experimental results are compared with calculations from two theoretical models of two-plasmon-decay instability for the exact parameters of the experiment. The open squares are results obtained from the code *ZAK*,[12] which solves the equations of the extended Zakharov model.[36] The saturating nonlinearities included in the model are density-profile modification,[37] Langmuir wave cavitation,[38] and the generation of ion-acoustic turbulence.[12,39] While this plasma fluid model is able to describe the growth and nonlinear saturation of the instability, it does not include kinetic effects responsible for hot-electron generation. An estimate for the hot-electron temperature is obtained from the nonlinearly

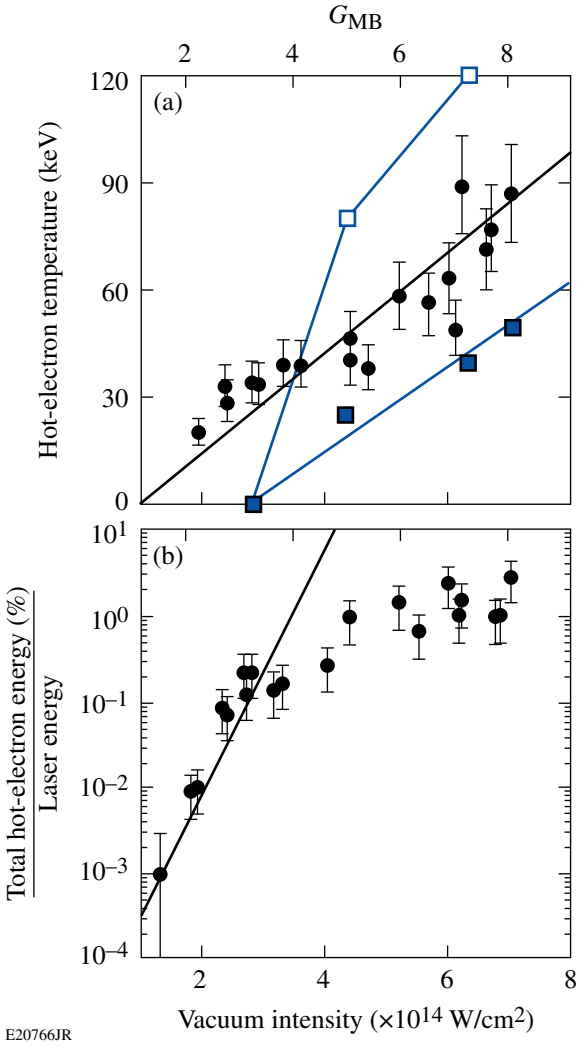

Figure 129.34
(a) The hot-electron temperature inferred from the HXRD measurements (circles) is shown as a function of the vacuum overlapped intensity and the multibeam convective gain. The hot-electron temperature is calculated by *ZAK* (open squares) and *QZAK* (solid squares) using the simulated $n_{cr}/4$ hydrodynamic parameters. (b) The fraction of total laser energy deposited into the hot electrons is plotted as a function of the vacuum overlapped intensity and the multibeam convective gain. An exponential scaling $\sim\exp\left(G_{MB}/0.3\right)$ is shown for comparison (line).

saturated state via the integration of test-electron trajectories in the electrostatic fields associated with the Langmuir turbulence (see Ref. 12 for more details).

The electron-plasma wave spectrum at saturation is found to be very broad, extending from small wave numbers up to the Landau cutoff ($k\lambda_D = 0.25$). When the effect of the turbulent electron-plasma wave spectrum on hot-electron production is investigated by integrating electron test particle trajectories,[12] the heating is found to be diffusive for electrons above a thresh-

old energy corresponding to the smallest phase velocity plasma waves (those at the Landau cutoff, $1/2 m_e v_\phi^2 \sim 20$ to 30 keV). The rate of diffusion (heating) was found to scale with $I_q L_n / T_e$ as a result of the interplay between the root-mean-square plasma-wave amplitudes and the available acceleration length.[12]

The solid squares show the results of a generalization of the *ZAK* model, called *QZAK*,[40] currently under development, where kinetic effects are taken into account self-consistently in the quasilinear approximation. The addition of kinetic effects reduces the amplitude of the electron-plasma waves, reducing the hot-electron temperature for a given $I_q L_n / T_e$. The difference between the two model predictions highlights the difficulty in making predictive calculations of a highly turbulent and complex physical system.

2. Fraction of Hot Electrons

Figure 129.34(b) shows the fraction of laser energy converted into hot electrons, which is estimated using the measured total K_α energy [Fig. 129.30(b)]. The large fraction of energy deposited into the hot electrons and the observed saturation of the TPD instability are direct consequences of the simultaneous high intensity and long scale lengths produced in these experiments.

It appears TPD is only convectively unstable in these experiments. The absolutely unstable electron-plasma waves, which depend only on the single-beam intensity, are well below the absolute intensity threshold (I_{th}) for the highest laser intensities tested;

$$\left\{\eta \equiv \frac{I_s}{I_{th}} = \frac{I_s\left(\times 10^{14}\ \mathrm{W/cm^2}\right) L_n(\mu\mathrm{m})}{230\ T_e(\mathrm{keV})} < 1\right\}$$

(Ref. 41), where I_s is the single-beam intensity at $n_{cr}/4$.

A convective gain for TPD that depends on the overlapped laser-beam intensity is presented in Ref. 42, where multiple laser beams are shown to drive common electron-plasma waves. For the experiments discussed here, the maximum convective gain is

$$G_{MB} \cong 1.5 \times 10^{-2} I_q \left(\times 10^{14}\ \mathrm{W/cm^2}\right) L_n(\mu\mathrm{m}) / T_e(\mathrm{keV}),$$

where I_q is the overlapped laser beam intensity at $n_{cr}/4$.

The multiple-beam gain is significantly larger than the single-beam gain $\left(G_{MB}/G_{SM} \simeq 3\right)$; note that the single-beam gain depends on the single-beam intensity $\left(I_s = I_q/4\right)$ and the intensity at $n_{cr}/4$ is ~55% less than the vacuum intensity. Figure 129.34 shows the experimental results plotted against the multiple-beam gain. A threshold for hot-electron generation is observed at a multiple-beam gain of ~2. It is likely that the actual gain for laser beams with DPP's (i.e., beams with speckles) is 2 to 5 times larger.[43]

At the highest overlapped-laser-beam intensity (7×10^{14} W/cm^2), the TPD gain increases approximately linearly in time over ~1.3 ns to a constant level of $G_{MB} \simeq 8$. When the gain reaches $G_{MB} \simeq 2.3$ ($t = 0.6$ ns), the hard x-ray signal begins to rapidly rise before reaching a nearly constant level [Fig. 129.30]. For the lowest intensities (1.3×10^{14} W/cm^2) where K_α radiation was detected (limited by signal to noise in the detector), the common-wave TPD gain is calculated to be $G_{MB} \simeq 2$, which is consistent with the gain threshold shown in Fig. 129.34.

Summary

This target platform was designed to account for all of the hot electrons generated by TPD. In general, the coupling of hot electrons to a fusion target will be reduced by the electron divergence, the distance between where the electrons are created and where they are absorbed, the electron energy distribution, and other loss mechanisms. The planar nature of these experiments, the fact that the laser beams are at near-normal incidence to the target, and the fact that they are linearly polarized in a common direction without polarization smoothing all tend to maximize the hot-electron generation. The multibeam linear gain depends on the geometry of the beams and their polarizations, which must be taken into account when applying these results to ignition designs.[42]

In summary, the high laser intensities generated over 1-mm-diam laser spots produced plasmas with a density scale length of 400 μm, causing two-plasmon decay to be driven to saturation. The hot-electron temperature is measured to increase rapidly (25 keV to 90 keV) with increasing laser-beam intensity (2×10^{14} W/cm^2 to 7×10^{14} W/cm^2). The total energy in hot electrons generated by TPD is measured to increase exponentially and saturate at a level of ~1% of the laser energy as the intensity is increased above 3×10^{14} W/cm^2. Uncertainties in the coupling of TPD electrons to the imploding shell and an accounting of the geometry and polarization of the laser beams prevent a quantitative assessment of the effect of TPD on direct-drive fusion, but these experiments suggest that maintaining the multibeam convective gain below 5 is a conservative approach to an acceptable level of hot-electron generation in direct-drive–ignition target designs.

ACKNOWLEDGMENT

We acknowledge the OMEGA EP operations team whose efforts provided the increased laser power necessary for these results. This work was supported by the U.S. Department of Energy Office of Inertial Confinement Fusion under Cooperative Agreement No. DE-FC52-08NA28302, the University of Rochester, and the New York State Energy Research and Development Authority. The support of DOE does not constitute an endorsement by DOE of the views expressed in this article.

REFERENCES

1. J. Nuckolls *et al.*, Nature **239**, 139 (1972).
2. R. L. McCrory, D. D. Meyerhofer, R. Betti, R. S. Craxton, J. A. Delettrez, D. H. Edgell, V. Yu Glebov, V. N. Goncharov, D. R. Harding, D. W. Jacobs-Perkins, J. P. Knauer, F. J. Marshall, P. W. McKenty, P. B. Radha, S. P. Regan, T. C. Sangster, W. Seka, R. W. Short, S. Skupsky, V. A. Smalyuk, J. M. Soures, C. Stoeckl, B. Yaakobi, D. Shvarts, J. A. Frenje, C. K. Li, R. D. Petrasso, and F. H. Séguin, Phys. Plasmas **15**, 055503 (2008).
3. T. R. Boehly, V. N. Goncharov, W. Seka, M. A. Barrios, P. M. Celliers, D. G. Hicks, G. W. Collins, S. X. Hu, J. A. Marozas, and D. D. Meyerhofer, Phys. Rev. Lett. **106**, 195005 (2011).
4. J. D. Lindl *et al.*, Phys. Plasmas **11**, 339 (2004).
5. V. N. Goncharov, T. C. Sangster, T. R. Boehly, S. X. Hu, I. V. Igumenshchev, F. J. Marshall, R. L. McCrory, D. D. Meyerhofer, P. B. Radha, W. Seka, S. Skupsky, C. Stoeckl, D. T. Casey, J. A. Frenje, and R. D. Petrasso, Phys. Rev. Lett. **104**, 165001 (2010).
6. H. Figueroa *et al.*, Phys. Fluids **27**, 1887 (1984).
7. M. V. Goldman, Ann. Phys. **38**, 95 (1966).
8. C. S. Liu, M. N. Rosenbluth, and R. B. White, Phys. Rev. Lett. **31**, 697 (1973).
9. B. B. Afeyan and E. A. Williams, Phys. Plasmas **4**, 3827 (1997).
10. M. N. Rosenbluth, R. B. White, and C. S. Liu, Phys. Rev. Lett. **31**, 1190 (1973).
11. D. F. DuBois, D. A. Russell, and H. A. Rose, Phys. Rev. Lett. **74**, 3983 (1995).
12. J. F. Myatt, J. Zhang, J. A. Delettrez, A. V. Maximov, R. W. Short, W. Seka, D. H. Edgell, D. F. DuBois, D. A. Russell, and H. X. Vu, Phys. Plasmas **19**, 022707 (2012).
13. N. A. Ebrahim *et al.*, Phys. Rev. Lett. **45**, 1179 (1980).
14. H. A. Baldis and C. J. Walsh, Phys. Rev. Lett. **47**, 1658 (1981).
15. W. Seka, D. H. Edgell, J. F. Myatt, A. V. Maximov, R. W. Short, V. N. Goncharov, and H. A. Baldis, Phys. Plasmas **16**, 052701 (2009).
16. C. Stoeckl, R. E. Bahr, B. Yaakobi, W. Seka, S. P. Regan, R. S. Craxton, J. A. Delettrez, R. W. Short, J. Myatt, A. V. Maximov, and H. Baldis, Phys. Rev. Lett. **90**, 235002 (2003).
17. An analytical error in the analysis of the HXRD used in Ref. 16 was identified and when corrected, the hot-electron temperature is reduced by ~40%.
18. J. H. Kelly, L. J. Waxer, V. Bagnoud, I. A. Begishev, J. Bromage, B. E. Kruschwitz, T. J. Kessler, S. J. Loucks, D. N. Maywar, R. L. McCrory, D. D. Meyerhofer, S. F. B. Morse, J. B. Oliver, A. L. Rigatti, A. W. Schmid, C. Stoeckl, S. Dalton, L. Folnsbee, M. J. Guardalben, R. Jungquist, J. Puth, M. J. Shoup III, D. Weiner, and J. D. Zuegel, J. Phys. IV France **133**, 75 (2006).
19. D. H. Froula, B. Yaakobi, S. X. Hu, P.-Y. Chang, R. S. Craxton, D. H. Edgell, R. Follett, D. T. Michel, J. F. Myatt, W. Seka, R. W. Short, A. Solodov, and "Saturation of the Two-Plasmon-Decay Instability in Long-Scale-Length Plasma Relevant to Direct-Drive Inertial Confinement Fusion," to be published in Physical Review Letters.
20. *LLE Review Quarterly Report* **127**, 109, Laboratory for Laser Energetics, University of Rochester, Rochester, NY, LLE Document No. DOE/NA/28302-1022 (2010).
21. T. J. Kessler, Y. Lin, J. J. Armstrong, and B. Velazquez, in *Laser Coherence Control: Technology and Applications*, edited by H. T. Powell and T. J. Kessler (SPIE, Bellingham, WA, 1993), Vol. 1870, pp. 95–104.
22. R. S. Craxton and R. L. McCrory, J. Appl. Phys. **56**, 108 (1984).
23. P. B. Radha, V. N. Goncharov, T. J. B. Collins, J. A. Delettrez, Y. Elbaz, V. Yu. Glebov, R. L. Keck, D. E. Keller, J. P. Knauer, J. A. Marozas, F. J. Marshall, P. W. McKenty, D. D. Meyerhofer, S. P. Regan, T. C. Sangster, D. Shvarts, S. Skupsky, Y. Srebro, R. P. J. Town, and C. Stoeckl, Phys. Plasmas **12**, 032702 (2005).
24. D. H. Froula, J. S. Ross, L. Divol. and S. H. Glenzer, Rev. Sci. Instrum. **77**, 10E522 (2006).
25. D. H. Froula, S. H. Glenzer, N. C. Luhmann, and J. Scheffield, *Plasma Scattering of Electromagnetic Radiation: Theory and Measurement Techniques*, 2nd ed. (Elsevier, Burlington, MA, 2011).
26. J. F. Seely *et al.*, Rev. Sci. Instrum. **81**, 10E301 (2010).
27. C. Stoeckl, W. Theobald, T. C. Sangster, M. H. Key, P. Patel, B. B. Zhang, R. Clarke, S. Karsch, and P. Norreys, Rev. Sci. Instrum. **75**, 3705 (2004).
28. B. Yaakobi, P.-Y. Chang, A. A. Solodov, C. Stoeckl, D. H. Edgell, R. S. Craxton, S. X. Hu, J. F. Myatt, F. J. Marshall, W. Seka, and D. H. Froula, Phys. Plasmas **19**, 012704 (2011).
29. U. Feldman *et al.*, Naval Research Laboratory and L. T. Hudson and S. Seltzer, National Institute of Standards and Technology, private communication (2011).
30. Spectral Instruments, Tucson, AZ 85745 (http://www.specinst.com/Products/800s_datasheet.pdf).
31. B. R. Maddox *et al.*, Rev. Sci. Instrum. **79**, 10E924 (2008).
32. A. L. Meadowcroft, C. D. Bentley, and E. N. Stott, Rev. Sci. Instrum. **79**, 113102 (2008).

33. C. Stoeckl, V. Yu. Glebov, D. D. Meyerhofer, W. Seka, B. Yaakobi, R. P. J. Town, and J. D. Zuegel, Rev. Sci. Instrum. **72**, 1197 (2001).

34. I. Kawrakow *et al*., NRC, Ottawa, Canada, NRCC Report PIRS-701 (May 2011); I. Kawrakow, Med. Phys. **27**, 485 (2000).

35. V. Metchnik and S. G. Tomlin, Proc. Phys. Soc. **81**, 956 (1963).

36. D. A. Russell and D. F. DuBois, Phys. Rev. Lett. **86**, 428 (1995).

37. A. B. Langdon, B. F. Lasinski, and W. L. Kruer, Phys. Rev. Lett. **43**, 133 (1979).

38. G. D. Doolen, D. F. DuBois, and H. A. Rose, Phys. Rev. Lett. **54**, 804 (1985).

39. R. Yan, A. V. Maximov, C. Ren, and F. S. Tsung, Phys. Rev. Lett. **103**, 175002 (2009).

40. D. A. Russell, presented at the Workshop on Laser Plasma Instabilities, sponsored by Lawrence Livermore National Laboratory and the University of Rochester's Laboratory for Laser Energetics, Livermore, CA, 3–5 April 2002.

41. A. Simon, R. W. Short, E. A. Williams, and T. Dewandre, Phys. Fluids **26**, 3107 (1983).

42. D. T. Michel, A. Maximov, B. Yaakobi, S. Hu, J. Myatt, A. Solodov, R. W. Short, and D. H. Froula, "Experimental Demonstration of the Two-Plasmon-Decay Common-Wave Process," submitted to Physical Review Letters.

43. H. A. Rose and D. F. DuBois, Phys. Rev. Lett. **72**, 2883 (1994).

A Front End for Ultra-Intense Optical Parametric Chirped-Pulse Amplification

Introduction

Ultra-intense laser systems are being developed that will use the full potential of deuterated potassium dihydrogen phosphate (DKDP) crystals for high-energy optical parametric chirped-pulse amplification (OPCPA).[1,2] Noncollinear pumping of DKDP produces broadband gain for supporting pulses as short as 10 fs. Large DKDP crystals (>400 × 400 mm) enable one to use Nd:glass lasers as kilojoule pump sources. The front ends for these systems must provide broadband pulses centered at ~910 nm to match the gain of DKDP noncollinear optical parametric amplifiers (NOPA's) when pumped at 527 nm. The amplified pulses must be compressible and focusable to maximize the on-target intensity, and the temporal prepulse contrast must be high enough to avoid perturbing the target. Previous front-end demonstrations used the idler from the first amplifier stage to seed subsequent amplifiers in either an angularly dispersed geometry[1] or a chirped collinear geometry.[2] An alternate approach, based on white-light–continuum (WLC) generation in a YAG plate,[3] is described in this article.

Development of a Mid-Scale, All-OPCPA System

Figure 129.35 shows the three phases of development of a 7.5-J, 15-fs optical parametric amplifier line (OPAL) that uses technologies scalable to kilojoule energies. Phase 1 has been completed, Phase 2 is in construction, and Phase 3 is being designed. In Phase 1, the first stages of a prototype front end

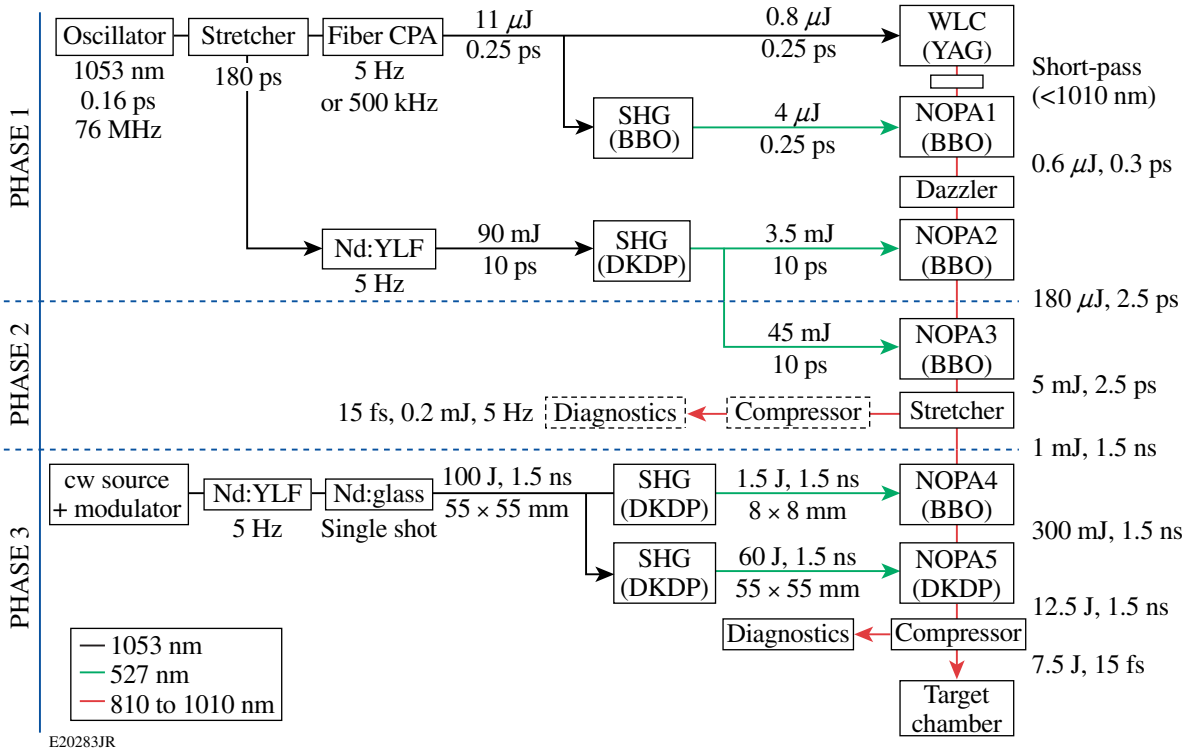

Figure 129.35
Schematic overview of a mid-scale optical parametric amplifier line (OPAL) that is in development. Phase 1 is completed, Phase 2 is in construction, and Phase 3 is being designed.

were developed to produce 180-μJ pulses with 200 nm of spectral support [160-nm full width at half maximum (FWHM)] centered at 910 nm (Fig. 129.36). Seeding the amplifiers with WLC simplifies the requirements for the seed oscillator and pump lasers and removes the need to eliminate the angular dispersion of the idler[1] or precisely set the spectral chirp of the pump.[2] Spectrum and spectral phase measurements made after recompression using a simple prism pair showed that the amplified white-light continuum was compressible to <13 fs, as expected [Fig. 129.36(b)].

Figure 129.37(a) shows a schematic of the nondegenerate NOPA-based cross-correlator[4] that was developed to measure the temporal contrast of the first NOPA stage. Measurements show a detection-limited prepulse contrast of greater than 120 dB up to −10 ps before the pulse [Fig. 129.37(b)].

Determining whether discrete peaks are real prepulses or artifacts caused by gate or pump postpulses is a problem common to all cross-correlators. For a NOPA-based device, however, the value of the peak can be determined from its scaling with the intensity of the pump.[4] By varying the pump-pulse energy before the cross-correlator and measuring the relative magnitudes of each peak, it was determined that all prepulses were caused by pump postpulses.

The second phase of OPAL is under construction. A pulse stretcher for the prototype front end has been developed based

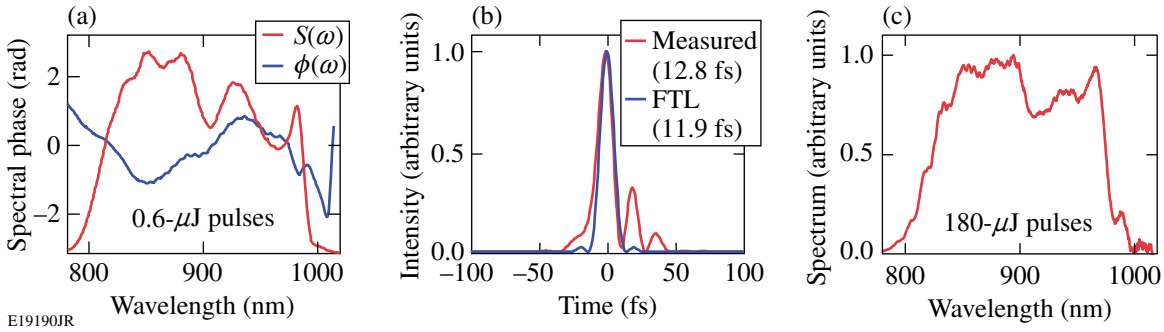

Figure 129.36
(a) Spectrum and spectral phase measurements after prism compression of NOPA1. (b) Calculations of the corresponding temporal intensity. (c) Spectrum after amplification to 180 μJ. FTL: Fourier transform limit.

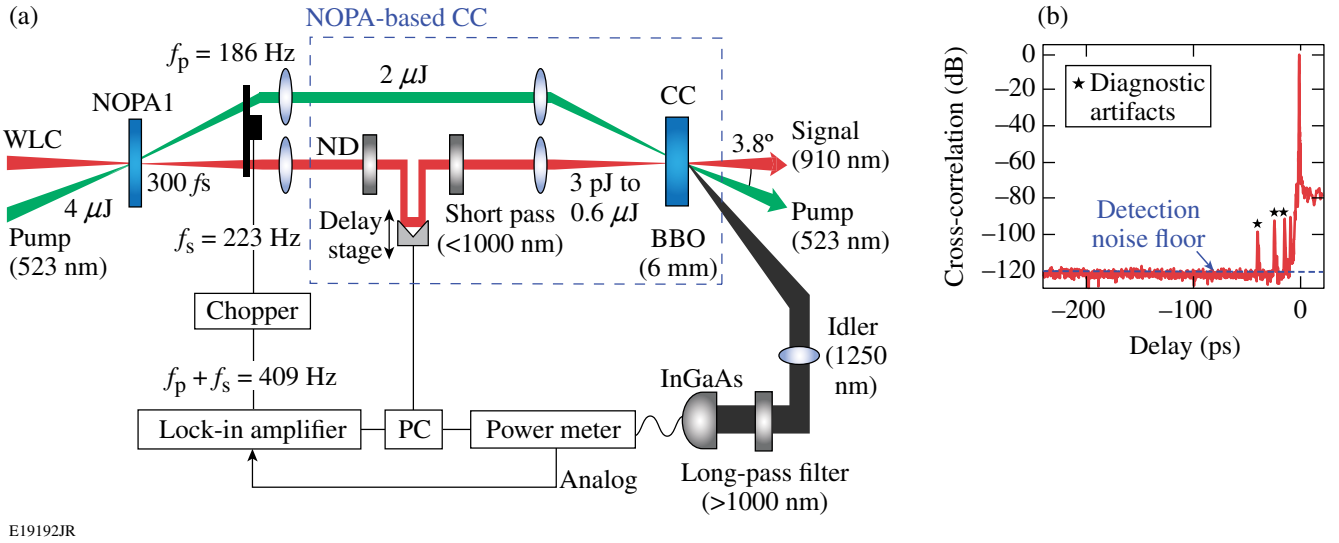

Figure 129.37
(a) Schematic of the NOPA-based cross-correlator for broadband (160-nm), high-sensitivity (39-dB gain), high-dynamic-range (120-dB) measurements of the prepulse contrast. (b) Temporal contrast measurements of the output of NOPA1 (before prism compression). BBO: beta-barium borate; CC: cross-correlator; InGaAs: indium gallium arsenide detector.

on a cylindrical Öffner design that has benefits beyond those originally proposed by Itatani *et al.*[5] Pulse stretchers with stretch ratios large enough for kilojoule systems (~10^5) must introduce minimal chromatic aberrations to ensure a high Strehl ratio at the laser focus.[6] They must permit preamplification using short-pulse–pumped parametric amplifiers to the millijoule level before stretching to improve temporal contrast.[7] Contrast degradation from their optical surface roughness imprinting on the spectral phase of the pulse must be minimized.[8] A cylindrical Öffner stretcher (COS) built to meet these requirements is being tested (Fig. 129.38). Modeling results in Fig. 129.38(b) show that a stretcher with cylindrical Öffner mirrors and two gratings (one at the center of curvature of the two Öffner mirrors) gives significantly better performance in these three areas than the standard spherical Öffner stretcher (SOS) with the same size optics and only one grating. Simulations predict that the mirror-limited temporal contrast is 30 dB better for the COS than a comparable-scale, single-grating SOS with similar surface quality because of the 50×-larger beam size on the secondary mirror.

In the third phase, the front end will seed a mid-scale optical parametric amplifier line (OPAL), which will be constructed next to LLE's Multi-Terawatt (MTW) laser.[9] Narrowband pulses from the MTW Nd:glass amplifier will be frequency doubled to provide up to 65 J for pumping the final beta-barium borate and DKDP amplifiers. OPAL will deliver 15-fs, 7.5-J pulses to an experimental target chamber at a rate of 1 shot/20 min. One stipulation for this system is that all technologies must be scalable to a full-kilojoule-scale OPAL, pumped by OMEGA EP's[10] four long-pulse beamlines, which could deliver 12 kJ of OPCPA pump energy at 527 nm.

Conclusion

OPAL provides a platform for addressing a number of technological challenges for ultra-intense lasers, many of which are shared with other ongoing projects. Areas that will be addressed include developing DKDP amplifiers and broadband and dichroic coatings with high damage thresholds; controlling spatial and spectral phases; relaying and up-collimating broadband, high-fluence beams; attaining high temporal contrast; and diagnosing the laser's single-shot performance.

ACKNOWLEDGMENT

This work was supported by the U.S. Department of Energy Office of Inertial Confinement Fusion under Cooperative Agreement No. DE-FC52-08NA28302, the University of Rochester, and the New York State Energy Research and Development Authority. The support of DOE does not constitute an endorsement by DOE of the views expressed in this article.

REFERENCES

1. V. V. Lozhkarev *et al.*, Laser Phys. **15**, 1319 (2005).
2. Y. Tang *et al.*, Opt. Lett. **33**, 2386 (2008).
3. M. Bradler, P. Baum, and E. Riedle, Appl. Phys. B **97**, 561 (2009).
4. J. Bromage, C. Dorrer, and J. D. Zuegel, in *Advanced Solid-State Photonics*, OSA Technical Digest (CD) (Optical Society of America, Washington, DC, 2011), Paper JWC2.
5. J. Itatani *et al.*, Opt. Commun. **134**, 134 (1997).
6. G. Chériaux *et al.*, Opt. Lett. **21**, 414 (1996).
7. C. Dorrer, I. A. Begishev, A. V. Okishev, and J. D. Zuegel, Opt. Lett. **32**, 2143 (2007).
8. J. Bromage, C. Dorrer, and R. K. Jungquist, "Temporal Contrast Degradation at the Focus of Ultrafast Pulses from High-Frequency

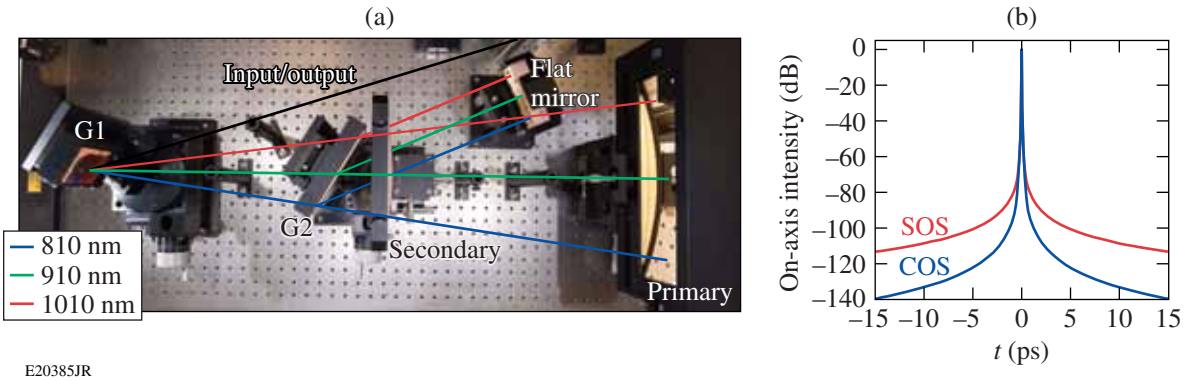

Figure 129.38
(a) Photograph of the cylindrical Öffner stretcher (COS) with an overlaid ray trace. (b) Calculated mirror-limited temporal contrast for the COS and a comparable-scale, single-grating spherical Öffner stretcher (SOS) with similar optical surface quality.

Spectral Phase Modulation," to be published in the Journal of the Optical Society of America B.

9. V. Bagnoud, J. Puth, I. Begishev, M. Guardalben, J. D. Zuegel, N. Forget, and C. Le Blanc, in *Conference on Lasers and Electro-Optics/Quantum Electronics and Laser Science and Photonic Applications, Systems and Technologies 2005* (Optical Society of America, Washington, DC, 2005).

10. J. H. Kelly, L. J. Waxer, V. Bagnoud, I. A. Begishev, J. Bromage, B. E. Kruschwitz, T. J. Kessler, S. J. Loucks, D. N. Maywar, R. L. McCrory, D. D. Meyerhofer, S. F. B. Morse, J. B. Oliver, A. L. Rigatti, A. W. Schmid, C. Stoeckl, S. Dalton, L. Folnsbee, M. J. Guardalben, R. Jungquist, J. Puth, M. J. Shoup III, D. Weiner, and J. D. Zuegel, J. Phys. IV France **133**, 75 (2006).

A Spherical Crystal Imager for OMEGA EP

Introduction

The unique capabilities of a crystal imaging system using spherically bent Bragg crystals are a narrow spectral width [$\lambda/\Delta\lambda$ >1000, (Ref. 1)], a high throughput (up to 100-fold improvement over pinhole imaging because of the larger solid angle), and a potentially high spatial resolution [<2 μm, (Ref. 2)]. Unlike a pinhole imager, a crystal imaging setup used in backlighting mode is insensitive to spatial nonuniformities in the backlighter intensity distribution because of its limited depth of field.[3] The major drawback of crystal imaging is the cost of the crystals and the complexity of the alignment. Crystal imaging has been frequently used on small- to medium-scale facilities, where the target chamber is vented between shots and direct operator access to the target chamber makes the alignment relatively easy.[1,2,4–7] On larger-scale facilities such as OMEGA EP,[8,9] where the target chamber stays at vacuum between shots, fully remote alignment of the crystal imager is required; consequently, only a very limited number of setups can be found in the literature.[3,10]

Experimental Setup

A crystal imaging system that can be remotely aligned and operated has been implemented on OMEGA EP (Fig. 129.39). In the first set of experiments this spherical crystal imaging (SCI) system used a quartz crystal, cut along the 2131 (211) planes for a $2d$ spacing of 0.3082 nm, to image the Cu K_α lines at ~8 keV. The Bragg angle of the quartz crystal for the Cu K_α is 88.7°, very close to normal incidence. The 25-mm-diam, ~150-μm-thick crystal was mounted by means of optical contact on a spherically shaped fused-silica substrate with a curvature radius of $R = 500$ mm. This curvature corresponds to a focal length of $f = R/2 = 250$ mm. The spherically bent crystal was fabricated by the Photonics Products Group, Inc. (PPGI).[11] The crystal is placed at a distance of 276 mm from the target, and the image is recorded on an image plate[12] located ~2.4 m from the target, resulting in a total magnification of ~10.

The SCI system uses two opposing ten-inch manipulators (TIM's) in its shot configuration, one housing the crystal and the other the image-plate detector. The TIM on OMEGA EP is a fully remote controllable three-axis diagnostic insertion system with an air lock, which allows the insertion of diagnostic modules of up to 25 cm in diameter and 50 kg of weight into the target chamber, without breaking vacuum.

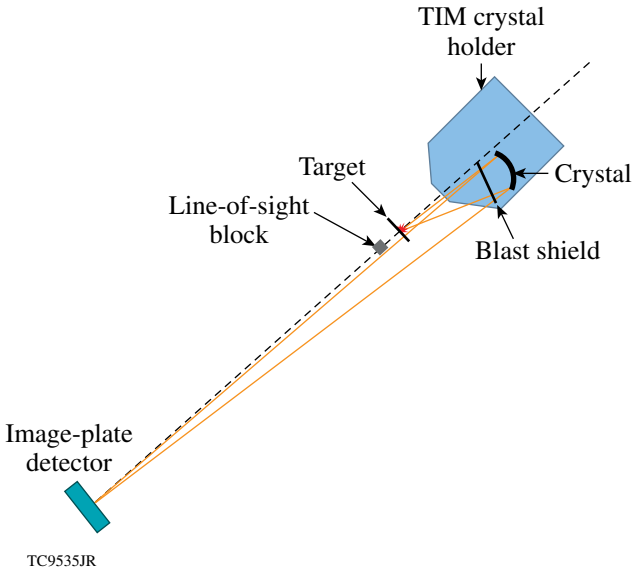

Figure 129.39
Schematic of the spherical crystal imager hardware in shot mode. One ten-inch manipulator (TIM) houses the crystal holder and another houses the image-plate detector. Both TIM's are on a common centerline indicated by the dashed line. A blast shield is placed in front of the spherically bent crystal, which images the target onto the detector. A direct line-of-sight tungsten block is placed opposite the crystal mount beyond the target to protect the detector from x-ray background emitted by the target.

The crystal is mounted on a motorized tip–tilt stage (New Focus 8817-V with PICO motor drive[13]) that sits on a TIM-mounted frame [Fig. 129.40(a)] and is inserted close to the target. A removable blast shield is placed in front of the crystal to protect it from debris. Because of the relatively high energy of the Cu K_α, the material and thickness of the blast shield are not critical even though the x rays must pass it twice. A blast shield of 10 to 20 μm of Al foil or 25 μm of Mylar coated with >100 nm of Al to prevent the scattered laser light from hitting

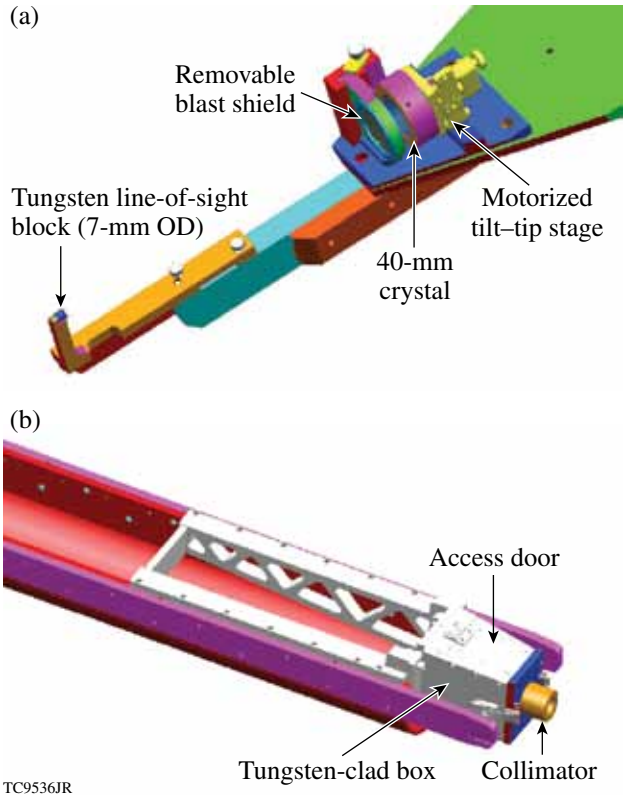

Figure 129.40
(a) CAD design of the crystal holder. The crystal is mounted on a motorized tip–tilt stage. A blast shield protects the crystal from target debris and can be removed for alignment. (b) CAD design of the image-plate holder. A tungsten-clad box houses the image plate, which records the image formed by the spherically bent crystal. An additional collimator is installed to further reduce the background from direct and Compton-scattered x rays. A filter foil is mounted in front of the collimator to optimize the signal level on the image-plate detector.

the crystal was sufficient for all experimental conditions. The blast-shield holder also accepts 1-mm-thick stainless-steel apertures to limit the active area of the crystal and to control the signal level on the detector. A 7.5-mm-thick, 7-mm-diam tungsten block protects the detector from x rays along the direct line of sight. The line-of-sight block is mounted on an arm attached to the crystal holder.

A CAD model of the image-plate detector's housing is shown in Fig. 129.40(b). A well-shielded, tungsten-clad box is mounted in the TIM opposing the crystal holder. An access door affords the operator easy access to insert the image-plate before the shot and remove it after the shot. A tungsten collimator reduces the field of view of the detector to suppress background from Compton scattering and fluorescence from structures in the target chamber. A Cu foil mounted in front of the collimator acts as a K-edge filter[14] to further improve the signal-to-background ratio. This filter is also used to optimize the signal level on the image-plate detector to prevent saturation. Typical filter thicknesses used in experiments range from 10 to 50 μm.

Alignment

The alignment procedure for the SCI system requires a number of steps. A pointer is first attached to the crystal holder hardware, and both the line-of-sight block and the blast shield are removed (Fig. 129.41). The tip of the pointer is optically aligned to target chamber center (TCC). The pointer is designed to set the distance from the crystal to the target to 276 mm, when the target is aligned to TCC. Mechanical alignment features in the pointer mount make a highly repeatable mounting of the pointer relative to the crystal mount possible. The pointer mount was designed not to block the two orthogonal lines of sight of the OMEGA EP Target Viewing and Alignment System. A precision of better than 100 μm can be achieved with this procedure.

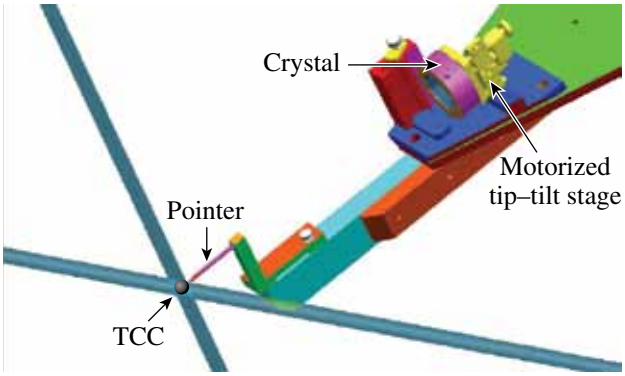

Figure 129.41
CAD design of the crystal holder in its pre-alignment configuration. A pointer is attached to the crystal holder hardware and optically aligned at target chamber center (TCC). The long, thin cylinders indicate the optical paths of the Target Viewing System.

In the next step the TIM coordinates are recorded, the TIM is retracted, and the pointer is removed from the crystal holder. The TIM is inserted again to its prerecorded position. Extensive tests have shown that this retract-and-insert cycle places the crystal back to the prerecorded position to within better than 100-μm accuracy. The tip of a single-mode fiber mounted in a third TIM is placed at TCC using the Target Viewing and Alignment System (Fig. 129.42). Light from an infrared (1053-nm) laser source is injected into the fiber. This light exits the fiber tip in an ~f/2 cone toward the spherically

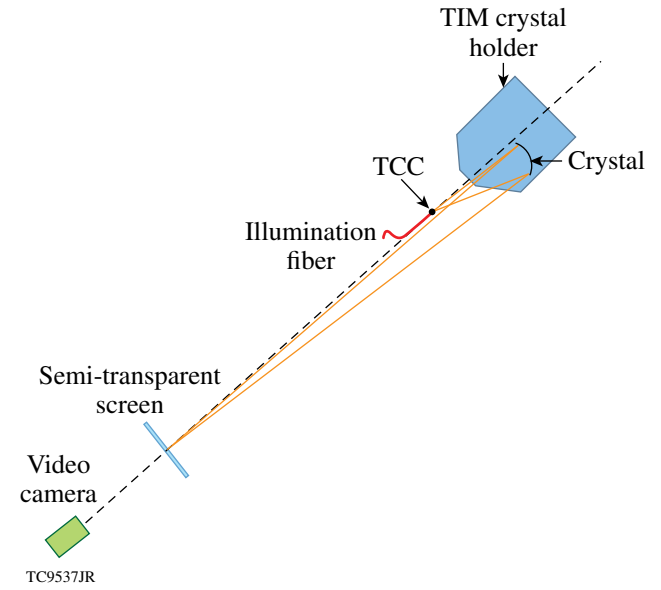

Figure 129.42
Schematic of the spherical crystal imager hardware in alignment mode. An illumination fiber is placed at TCC. Light from the fiber is reflected from the crystal to the semi-transparent screen. A video camera is used to optimize the focal spot on the screen.

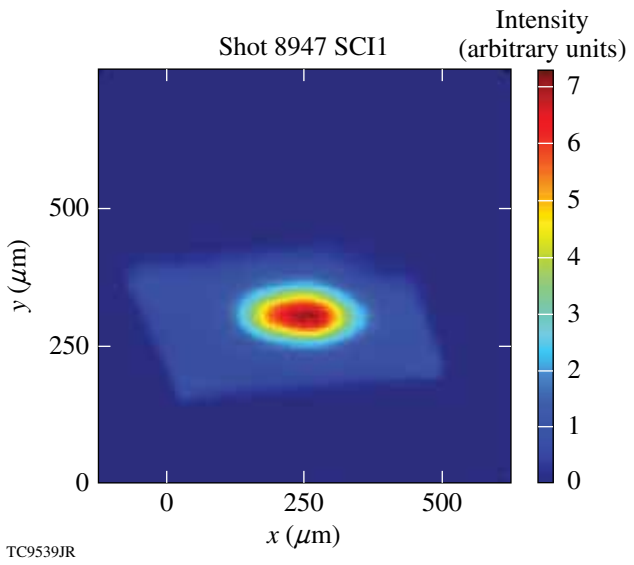

Figure 129.43
K_α image of a 500 × 500 × 20-μm^3 Cu foil, irradiated by an ~1-kJ, 10-ps, ~40-μm-diam OMEGA EP laser pulse. The spatial coordinates are scaled to the object plane.

bent crystal. A fraction of the infrared light is reflected off the crystal surface and sent toward the opposing TIM. The image-plate detector box in the opposing TIM is replaced by a semi-transparent screen, which is placed at the same distance from TCC as the image plate. This screen is viewed by an infrared-sensitive video camera. The motorized tip–tilt stages of the crystal mount are used to position the image formed by the spherical crystal at the center of the screen. Small corrections of the TIM insertion axis are used to optimize the focus of the crystal imager. The wavelength of the alignment source is not crucial. Off-line tests with a 680-nm-wavelength red laser have shown similar results. It is critical to use a single-mode fiber to generate a well-defined object, so that the crystal produces a clean image that can be used to optimize the focus.

Finally, the fiber is removed from its TIM, and the semi-transparent screen is replaced with the image-plate detector box. The crystal holder is retracted, and the blast shield and line-of-sight block are re-installed. The crystal holder is inserted again and the SCI system is ready for shots.

Experimental Data

Figure 129.43 shows one of the first images recorded with the SCI system. A 500 × 500 × 20-μm^3 Cu foil was irradiated by an ~1-kJ, 10-ps OMEGA EP laser pulse. The SCI views the target from an angle of 63° relative to the target normal, which leads to a foreshortening of the image in the vertical direction by a factor of ~2. Even though the laser focal spot is only ~40 μm in diameter, the image shows that the K_α radiation is emitted from the whole target area with an ~100-μm-diam bright spot located roughly where the laser hits the target. This image is consistent with other observations that show that most of the electrons generated in the laser–plasma interactions are confined to the target by strong electric fields set up when the first high-energy electrons leave the target and charge it to a multi-MeV potential.[15–17] The confined electrons flood the target and generate a quasi-uniform emission. The slightly darker area on the top-right corner of the target is due to the fact that the target is attached to a stalk at this corner, which allows the electrons to escape, thereby reducing the K_α emission.

The signal-to-background ratio is evaluated by measuring the average value of the signal on the image plate outside the object and comparing it to the signal measured at the edge of the image and the peak in the center of the image. With a typical background signal of 0.01 photostimulated luminescence (PSL) outside the image, ~1 PSL at the edge, and ~6 PSL at the peak, signal-to-background levels of 100 to 600 are observed.

To assess the spatial resolution of the SCI, lineouts are taken across the edge of the image at different locations (see Fig. 129.44). The rise of the signal from 10% to 90% of its

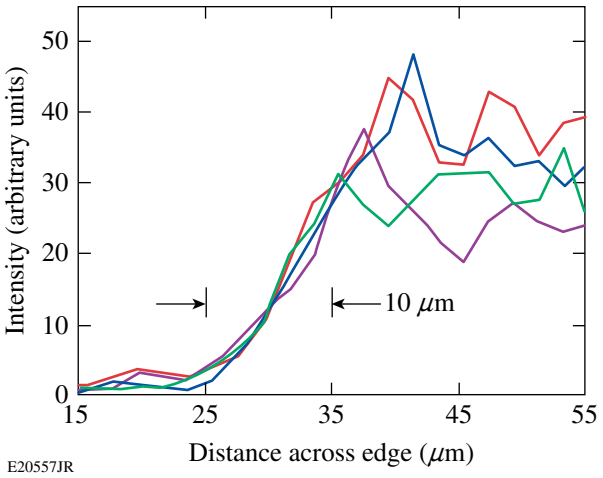

Figure 129.44
Edge lineouts of an image from the SCI at different locations. The signal rises from 10% to 90% of the peak in ~10 μm for the locations where the imager is in best focus.

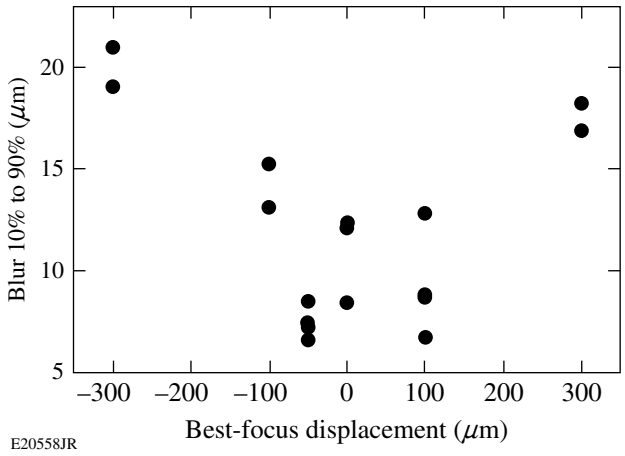

Figure 129.45
Edge rise from 10% to 90% of the peak as a function of defocus in the spherical crystal imager. Zero displacements are defined as the locations of the pre-shot optical alignment.

peak value is taken as a figure of merit for the resolution of the imaging system. This 10% to 90% criterion is a more-stringent measure of resolution, compared to a measurement of the modulation transfer function, where the resolution is usually defined at either a 50% or 10% contrast value. Since the imager has a limited depth of focus and views the object from a steep angle of 63° relative to the target normal, the resolution changes across the edge from ~10 μm, where the object is in best focus, to ~15 μm outside best focus.

A series of experiments were performed to measure the depth of focus of the imaging system by intentionally changing the crystal's distance from the target from the optimal position as determined by the pre-shot optical alignment (see Fig. 129.45). The best resolution of the SCI is observed in these experiments for displacements of <100 μm from the pre-shot alignment. At larger displacements the resolution deteriorates to values of the order of 20 μm at 300-μm displacement.

Summary and Conclusions

A crystal imaging system that can be fully remotely aligned has been implemented on OMEGA EP. A spherically bent quartz crystal is used to image the Cu K_α emission of targets irradiated with up to 1 kJ of laser energy at a 10-ps pulse duration. Experiments performed to map out the depth of focus of the crystal imager showed that the pre-shot optical alignment sets the SCI to its optimum focus condition. A best-focus resolution of ~10 μm, measured as the 10% to 90% rise on the edge of the image, has been achieved. The images show a very high signal-to-background ratio of >100, which indicates that the shielding concepts used in the setup of the SCI are effective and will provide adequate shielding even at the highest planned energies of 2.6 kJ at 10 ps on OMEGA EP. A similar crystal imaging system has been implemented on the OMEGA Laser System. Only minor adjustments to the mechanical layout of this system are required to adapt it to other spectral lines using different crystals and Bragg angles. Designs to modify the SCI to image the Si He_α spectral line are currently underway.

ACKNOWLEDGMENT

This work was supported by the U.S. Department of Energy Office of Inertial Confinement Fusion under Cooperative Agreement No. DE-FC52-08NA28302, the University of Rochester, and the New York State Energy Research and Development Authority. The support of DOE does not constitute an endorsement by DOE of the views expressed in this article.

REFERENCES

1. T. A. Pikuz *et al.*, in *EUV, X-Ray, and Neutron Optics and Sources*, edited by C. A. MacDonald *et al.* (SPIE, Bellingham, WA, 1999), Vol. 3767, pp. 67–78.
2. Y. Aglitskiy *et al.*, Appl. Opt. **37**, 5253 (1998).
3. J. A. Koch *et al.*, Rev. Sci. Instrum. **74**, 2130 (2003).
4. T. Missalla *et al.*, Rev. Sci. Instrum. **70**, 1288 (1999).
5. Ch. Reich *et al.*, Phys. Rev. E **68**, 056408 (2003).
6. S. Le Pape *et al.*, Rev. Sci. Instrum. **79**, 106104 (2008).
7. J. A. King, K. Akli, R. A. Snavely, B. Zhang, M. H. Key, C. D. Chen, M. Chen, S. P. Hatchett, J. A. Koch, A. J. MacKinnon, P. K. Patel,

T. Phillips, R. P. J. Town, R. R. Freeman, M. Borghesi, L. Romagnani, M. Zepf, T. Cowan, R. Stephens, K. L. Lancaster, C. D. Murphy, P. Norreys, and C. Stoeckl, Rev. Sci. Instrum. **76**, 076102 (2005).

8. L. J. Waxer, D. N. Maywar, J. H. Kelly, T. J. Kessler, B. E. Kruschwitz, S. J. Loucks, R. L. McCrory, D. D. Meyerhofer, S. F. B. Morse, C. Stoeckl, and J. D. Zuegel, Opt. Photonics News **16**, 30 (2005).

9. C. Stoeckl, J. A. Delettrez, J. H. Kelly, T. J. Kessler, B. E. Kruschwitz, S. J. Loucks, R. L. McCrory, D. D. Meyerhofer, D. N. Maywar, S. F. B. Morse, J. Myatt, A. L. Rigatti, L. J. Waxer, J. D. Zuegel, and R. B. Stephens, Fusion Sci. Technol. **49**, 367 (2006).

10. K. Fujita *et al.*, Rev. Sci. Instrum. **72**, 744 (2001).

11. Photonics Products Group, Inc., Northvale, NJ 07647.

12. A. L. Meadowcroft, C. D. Bentley, and E. N. Stott, Rev. Sci. Instrum. **79**, 113102 (2008).

13. New Focus, Inc., A Division of Newport Corporation, Irvine, CA 92606.

14. C. Stoeckl, W. Theobald, T. C. Sangster, M. H. Key, P. Patel, B. B. Zhang, R. Clarke, S. Karsch, and P. Norreys, Rev. Sci. Instrum. **75**, 3705 (2004).

15. J. Myatt, W. Theobald, J. A. Delettrez, C. Stoeckl, M. Storm, T. C. Sangster, A. V. Maximov, and R. W. Short, Phys. Plasmas **14**, 056301 (2007).

16. P. M. Nilson, W. Theobald, J. Myatt, C. Stoeckl, M. Storm, O. V. Gotchev, J. D. Zuegel, R. Betti, D. D. Meyerhofer, and T. C. Sangster, Phys. Plasmas **15**, 056308 (2008).

17. K. U. Akli, M. H. Key, H. K. Chung, S. B. Hansen, R. R. Freeman, M. H. Chen, G. Gregori, S. Hatchett, D. Hey, N. Izumi, J. King, J. Kuba, P. Norreys, A. J. Mackinnon, C. D. Murphy, R. Snavely, R. B. Stephens, C. Stoeckel, W. Theobald, and B. Zhang, Phys. Plasmas **14**, 023102 (2007).

Amplitude Distributions of Dark Counts and Photon Counts in NbN Superconducting Single-Photon Detectors Integrated with a High-Electron Mobility Transistor Readout

Introduction

Fast and reliable single-photon detectors (SPD's) have become a highly sought after technology in recent years.[1] Some of the most-interesting applications for SPD's, which include quantum communications and quantum key distribution[2] as well as satellite communications, require devices that can successfully operate at telecommunication wavelengths, namely 1310 nm and 1550 nm. Additional very desirable features for ideal SPD's are their photon-number resolution (PNR) capability,[3,4] e.g., for all-optical quantum computing, and their photon-energy sensitivity (PES),[5] e.g., for spectral observations of so-called photon-starved objects. InGaAs avalanche photodiodes work at telecommunication wavelengths and are commercially available; they do, however, suffer from severe after-pulsing and require time gating, which limits their maximum count rate. Presently, they also lack advanced PNR and PES capabilities.[6,7]

It has already been established that nanostructured, NbN superconducting SPD's (SSPD's) operate based on hot-spot formation and bias-current redistribution in ultrathin (4-nm), ultranarrow (100- to 120-nm), and long (~0.5-mm) meandering NbN superconductive nanostripes.[1,8] NbN SSPD's have been shown to have counting rates exceeding 250 MHz, with reported quantum efficiencies (QE's) up to 57% (Ref. 9) at 1550-nm wavelength and very low, <10-Hz to 10-kHz dark-count rates, depending on the operation bias point.[10]

Typically, the SSPD's are kept at temperatures between 1.7 and 4.2 K (far below the NbN critical temperature T_c) and biased at currents I_{bias} close to the meandering stripe critical current I_c. Once a photon is absorbed by the NbN nanostripe, it breaks a Cooper pair, and, subsequently, a large number of quasiparticles are generated through the electron–electron and electron–phonon interactions, creating a local hot spot, where superconductivity is suppressed or even destroyed. The hot spot expels the supercurrent from its volume and forces it to flow near the stripe edges, where it can exceed the I_c value, leading to the generation of phase-slip centers and the eventual formation of a resistive region (joule heating) across the width of the stripe.

When the SSPD device is directly connected to a transmission line with a characteristic impedance Z_0 equal to, e.g., 50 Ω, the above-mentioned resistive region, which is typically $\gg$50 Ω, forces the bias current to redistribute from the SSPD into the load, which means that the amplitude of the SSPD voltage response is always measured across the constant Z_0. The above conclusion would be true even if the SSPD were simultaneously illuminated by several photons and, consequently, several hot spots were simultaneously generated at various points along the meander. Therefore, in the above experimental arrangement, which is actually typical for the vast majority of published work, the SSPD photoresponse is insensitive to both the number and energy of incoming photons, and the device acts as a simple photon-event counter rather than an energy and/or spectrally sensitive detector.

We need to stress here that a biased SSPD can generate output electrical pulses even when the input light is completely blocked and there are no photons incident on the device. Those so-called dark-count pulses are transient voltage signals, spontaneously generated in a long, current-biased, superconducting nanostripe, and, when the device is connected to an output of a coaxial line, their amplitude is limited by Z_0 despite the fact that the physical origin of dark counts is different from that responsible for photon counts. In the case of dark counts, the transient resistive state across the SSPD nanostripe is actually caused by the current-induced generation and propagation of free vortex–antivortex pairs.[11,12] Therefore, in experimental studies of the SSPD performance, it would be very important to be able to distinguish the photon counts from the dark counts.

The goal of this work is to show that, with our recently developed new readout scheme that implements a low-noise, cryogenic, high-electron-mobility transistor (HEMT) and a high-load resistor next to the detector,[13] we are able, albeit not in real time, to resolve the difference between the SSPD dark- and photon-count events by collecting histograms of the output-pulse distributions and, subsequently, comparing their mean amplitudes and distribution widths. We also present our early findings that demonstrate that the same readout approach

can lead to some PNR functionality in SSPD's, as predicted in Ref. 14. We stress that although the research presented here is rather preliminary, it does represent an important step toward making SPD's true photon sensor-type devices with energy resolution.

This article begins with a brief description of the SSPD fabrication process and presents our experimental setup based on the high-input-impedance HEMT readout circuit. Next, we introduce a simple equivalent circuit of the SSPD, based on the fixed-equivalent-resistance hot-spot model and discuss its practical limitations, namely, the conditions that are needed to fulfill the requirement that the readout input impedance is always the dominant factor. Our experimental data are, subsequently, presented and consist of long, real-time SSPD traces collected either under photon illumination or in the dark. A statistical approach is used for the data analysis to calculate the corresponding distributions functions. The comparison between the distributions' mean amplitudes and widths enables one to quantitatively distinguish photon absorption events from dark counts. The presented analysis demonstrates how experimental data collected by an SSPD directly connected to the high-impedance readout can either shed light on the average photon number of the incident ultraweak flux of monochromatic light or provide some spectral characterization of multicolor pulses. Finally, a summary and concluding remarks are presented.

Device Description and Experimental Setup

SSPD's were patterned from epitaxial-quality NbN films, deposited by dc reactive magnetron sputtering onto sapphire substrates.[15] The films were characterized by a sheet resistance between 400 and 500 Ω/sq at room temperature, with T_c between 10 and 11 K, and the critical current density $J_c \approx 10^6$ A/cm^2. The meander patterning was done by e-beam lithography and reactive-ion etching. It is important to note here that while the films were deposited at the Moscow State Pedagogical University, they were patterned at Delft University of Technology. Apparently, slight differences in geometry or in the patterning method were responsible for the fact that the SSPD's in this work had 3×- to 4×-lower I_c's (~5 to 10 μA) than the typical Moscow devices.[15] The QE's, however, were on a par with the standard 10×10-μm^2 SSPD's, with the devices measured in this work having QE ≈ 3% to 5% at λ = 800 nm.

The standard SSPD operation setup is shown in Fig. 129.46(a). The device was wire bonded to a 50-Ω microstrip transmission line, coupled to a multimode optical fiber, and immersed in liquid helium.[16] The microstrip was then connected to a semi-rigid coaxial cable and, at room temperature, connected to a custom-made, wideband bias-tee (0.08- to 26-GHz bandwidth). The bias-tee enabled us to simultaneously amplify the transient photoresponse signal using a tandem of two broadband amplifiers (0.08- to 8.5-GHz bandwidth, 22-dB gain) and to dc bias both the SSPD and HEMT. The amplified output signals, corresponding to photon counts and/or dark counts, were recorded by using either a Tektronix digital single-shot oscilloscope (6-GHz bandwidth) or a pulse counter. As a photon source, we used a train of 100-fs-wide, 800-nm-wavelength pulses, generated by a mode-locked Ti:sapphire laser at a rate of 82 MHz. The pulses were heavily attenuated to precisely control the average number of photons per pulse. For dark-count measurements, the detector was blocked from all incoming radiation, i.e., shielded inside the Dewar by a metallic enclosure.

An equivalent electrical model of the SSPD photoresponse is shown in Fig. 129.46(b). Kinetic inductance L_k is in series with a parallel arrangement of a hot-spot resistance R_{hs}, and a switch S represents the photodetection (switching) event in the SSPD.[17] The detector is then connected to a dc bias source and a readout circuit, which, in this case, consists of a transmission line with input impedance Z_0 = 50 Ω. In the simulations presented on p. 41, we also took into account [not shown in Fig. 129.46(b)] a small, parasitic on-board capacitance and a bandpass filter representing the bandwidth of an outside (room-temperature) amplifier. Finally, V_{out} is the experimentally observed transient voltage pulse during photodetection.

Initially, the switch is closed and there is no voltage drop. Once a photon is absorbed by our nanostripe, the switch opens, and as R_{hs} grows to a value much larger than Z_0, most of the

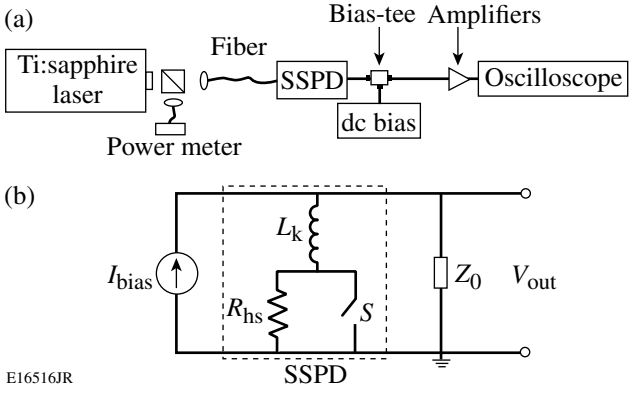

Figure 129.46
(a) Experimental setup and (b) standard electrical photoresponse model of SSPD (superconducting single-photon detector).

current redistributes into Z_0, and the resultant voltage pulse amplitude is simply $V_{out} \approx Z_0(I_{bias} - I_{ret})$, where I_{ret} is the value of current flowing through the device at the highest value of R_{hs} (Ref. 17). Therefore, independent of the number or energy of the absorbed incident photons, V_{out} always has the same value for a given I_{bias} for the circuit shown in Fig. 129.46(b).

Our high-impedance readout scheme, presented in Fig. 129.47, was first described in Ref. 13 and, as already outlined there, it implements a commercial HEMT, operated cryogenically, and mounted next to (on the same board) the SSPD. The HEMT acts as an infinite-impedance element to separate the 50-Ω output transmission line from the SSPD. Because the HEMT input impedance is very high, a 500-Ω load (or shunt) resistor R_L is also used in parallel with the detector and the HEMT, as shown in Fig. 129.47. As mentioned previously, both the SSPD and HEMT were biased through the same custom-made, wideband bias-tee. Such an integrated arrangement enables one to bias the devices using R_{bias} = 150 kΩ, mounted on the board together with the rest of the components and, simultaneously, to read out the ac photoresponse voltage signal.

By applying the detector transient response to the gate of the HEMT, one can read out the drain voltage, which should, ideally (for $R_L \gg R_{hs}$), be proportional to the hot-spot resistance and equal to V_{out}. If the number of photons simultaneously absorbed in the SSPD meander happens to be larger than 1, the photons are likely to form separate hot spots and their resistances will add up in series. The HEMT output voltage in this simplest case should be $V_{out} \approx (I_{bias} - I_{ret})nR_{hs}$, where n is the number of absorbed photons per pulse (actually, the number of created hot spots). Therefore, for relatively small n's, and in the case of $nR_{hs} < R_L$, the output-pulse height of our setup is proportional to n, effectively leading to PNR, as was theoretically discussed and modeled in Ref. 14.

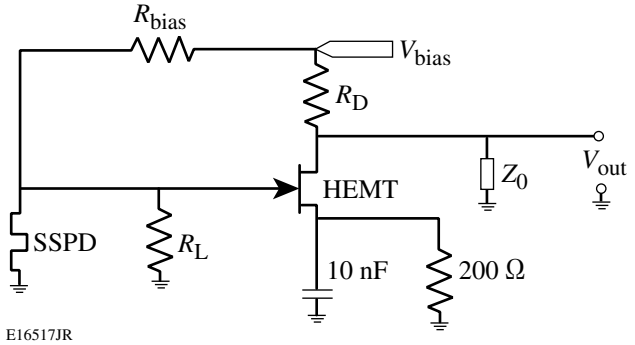

Figure 129.47
Circuit schematics implementing a HEMT (high-electron-mobility transistor) amplifier and 500-Ω load resistor R_L. The 10-nF capacitor sets the maximum ac gain and the 200-Ω resistor sets the dc current for the HEMT; R_{bias} and R_D are the biasing and pull-up resistors, respectively.

Based on an intrinsic difference in the physics mechanisms of the generation of photon and dark-count transients in SSPD's discussed above, the HEMT setup should also enable one to distinguish pulses generated in response to either a single-photon absorption event (photon count) or a spontaneous voltage transient (dark count). In the case of dark counts, one can expect only a single localized resistive region, created by the vortex–antivortex pair's (VAP's) motion across the stripe,[12] with the effective resistance different than R_{hs}, resulting in a somewhat different value of V_{out}. In the full analogy, it is expected that photons of different energies should produce hot spots with different R_{hs} values, so our SSPD with the HEMT readout should possess PES functionality.

Readout Circuit Simulations and Model Limitations

Our HEMT approach takes advantage of the simple fact that the greater the R_L, the more sensitive the readout in terms of either PNR or PES. Unfortunately, this cannot be easily accomplished since the large R_L values lead to an underdamped circuit behavior (see Fig. 129.48) because of a very large value of the indicator ($L_k \sim 400$ nH) of our SSPD[17] in parallel with R_L. Figure 129.48(a) shows the PSpice[a]-simulated pulses for different values of R_L. Critical damping yields R_L = 270 Ω (red curve) in Fig. 129.48(a), and it can be seen that for R_L = 500 Ω (green curve), the circuit is already slightly underdamped since a small, damped oscillation follows the main pulse. Figure 129.48(b) shows an experimental voltage pulse (black line) obtained using our HEMT readout approach, as well as a simulated one (red dashed line). The slow, damped oscillations behind the measured main pulse are caused by some second-order, capacitive effects from the HEMT circuit and/or stainless-steel coaxial line. An associated small parasitic capacitance (not shown in Fig. 129.47) has been estimated to be 2 to 3 pF, by looking at the oscillation frequency of the underdamped pulse.

Our tested SSPD's typically exhibited $I_c \approx 5\ \mu$A, leading to the roughly estimated R_{hs} value to be between 600 and 1000 Ω. Therefore, based on the behavior observed in Fig. 129.48, we selected R_L = 500 Ω for all our experiments as a compromise between the optimal value (minimal oscillations) from the

[a]PSpice (currently available from OrCAD Corp. of Cadence Design Systems) is a PC version of SPICE, originally developed at the Electronics Research Laboratory of the University of California, Berkeley (1975).

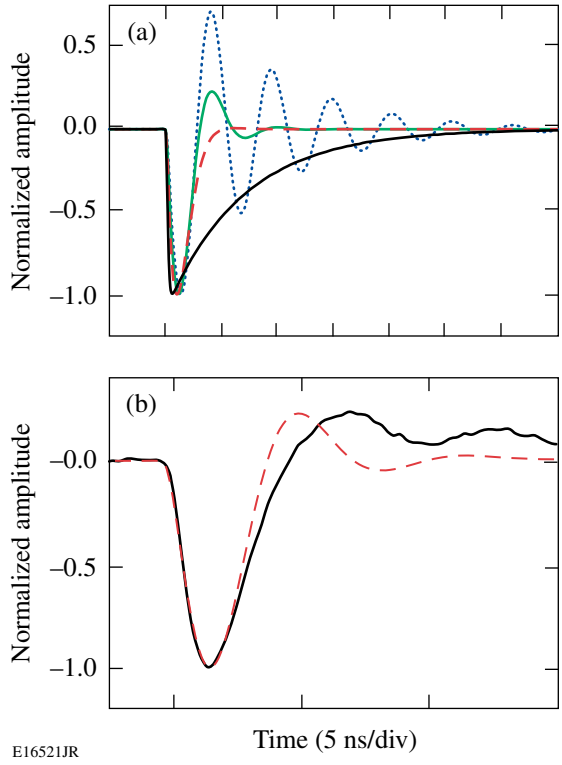

Figure 129.48
(a) PSpice simulations of voltage transients at different values of R_L: 50 Ω (black curve), 270 Ω (red dashed curve), 500 Ω (green curve), and 2 kΩ (blue dotted curve); (b) measured photoresponse (black curve) and simulated photoresponse (red dashed curve) for R_L = 500 Ω.

circuit point of view and the need to have R_L as large as possible to achieve PNR functionality. Since R_L = 500 Ω is at best comparable to R_{hs}, the experimentally measured V_{out} readout signal amplitude is proportional to a parallel connection of R_L and R_{hs}, limiting the ability to fully quantitatively distinguish between the different types of SSPD counting events. Therefore, the experimental observations presented here are mainly qualitative. In addition, since real-time analysis has been inconclusive, it was decided to use a statistical approach to analyze our experimental data.

Our approach of an SSPD integrated with an HEMT readout with a fixed R_L = 500 Ω value can work satisfactorily, as will be shown later, but only for devices with rather small I_c and, consequently, typically, low QE. In large-QE SSPD's biased close to I_c, as shown in Ref. 18, the R_{hs} can be as large as 5.5 kΩ, mainly because of joule heating. Joule heating of the nanostripe turns it completely resistive and occurs in parallel with the hot-spot cooling process and current redistribution.[18] The latter can be well illustrated looking at the time-domain evolution of the photoresponse transient. Based on the electrical model shown in Fig. 129.47, the difference in amplitude for different hot-spot resistances stem from variations in the time interval it takes for the current initially biasing the device to redistribute into the readout circuit. In other words, for a given R_L, current redistribution time decreases with increasing R_{hs}. For the hot spot to stop growing and the cooling mechanism to take over, the current through the device must drop to a value below approximately 20% of I_c (Ref. 19). When the SSPD photoresponse is modeled such that R_{hs} is a simple resistor, the fall and rise time constants of the transient V_{out} are simply $\tau_{fall} = L_k/(R_{hs} + R_L)$ and $\tau_{rise} = L_k/R_L$ (Ref. 17), respectively. On the other hand, if R_{hs} progressively increases during the current redistribution, the entire process becomes nonlinear and the transient decay cannot be modeled by a simple exponential function. From the readout circuit point of view, this is a very challenging problem since even if it were possible to find a cryogenic amplifier with large enough R_L, the readout scheme would not work because the current would not be able to redistribute into the load fast enough to prevent a runaway heating effect that would cause the device to simply latch.

We believe the best approach to restrict the uncontrolled growth of R_{hs} and, consequently, suppress the heat runaway effect is to significantly improve the heat transport between the superconductor and the substrate (single-crystal sapphire for "standard" SSPD's), either by using substrates, which are a better acoustic-phonon match to NbN, or by changing the nanostripe material. In the latter case, the ferromagnet/superconductor nanostructured bilayers are very promising because, as has recently been shown, they exhibit much-faster electron–phonon dynamics, as compared to plain Nb or NbN.[20,21]

Results and Discussion

During the course of our experiments, we have collected very long (millions of pulses) real-time traces by continuously recording either photon-count events or dark counts. In the latter case, the voltage response was measured when an SSPD was completely isolated from the outside world. Figures 129.49(a) and 129.49(b) present randomly selected, short sections of photon-count traces of output pulses (after amplification) recorded in time-domain when an SSPD was connected either according to the conventional 50-Ω scheme [Fig. 129.46(b)] or a scheme with an HEMT readout (Fig. 129.47), respectively. The incident laser intensity was adjusted in such a way that nearly every photon pulse was registered by the detector (for an SSPD with QE ≈ 5% that corresponds to ~500 photons per pulse). These plots are intended to illustrate a qualitative difference in the recorded photoresponse signals, since even from such short "snapshots," it can clearly be seen that while in the

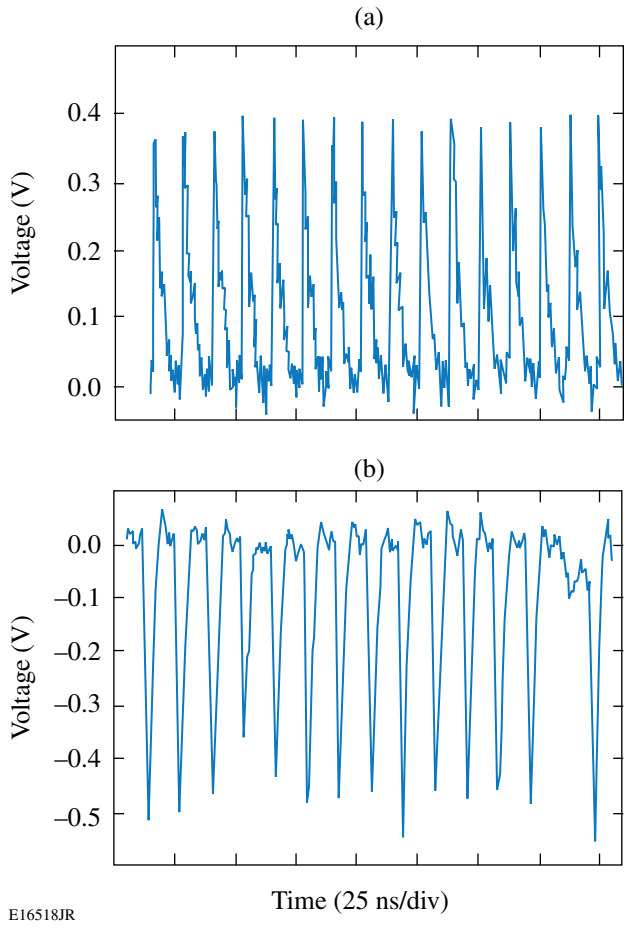

Figure 129.49
Comparison of live oscilloscope time-domain traces for (a) a traditional scheme and (b) an HEMT readout scheme, taken at similar laser intensities, such that $n \leq 1$ (HEMT is an inverting amplifier; therefore the pulses are negative). Here, n is the number of absorbed photons per pulse. The laser repetition rate is 82 MHz.

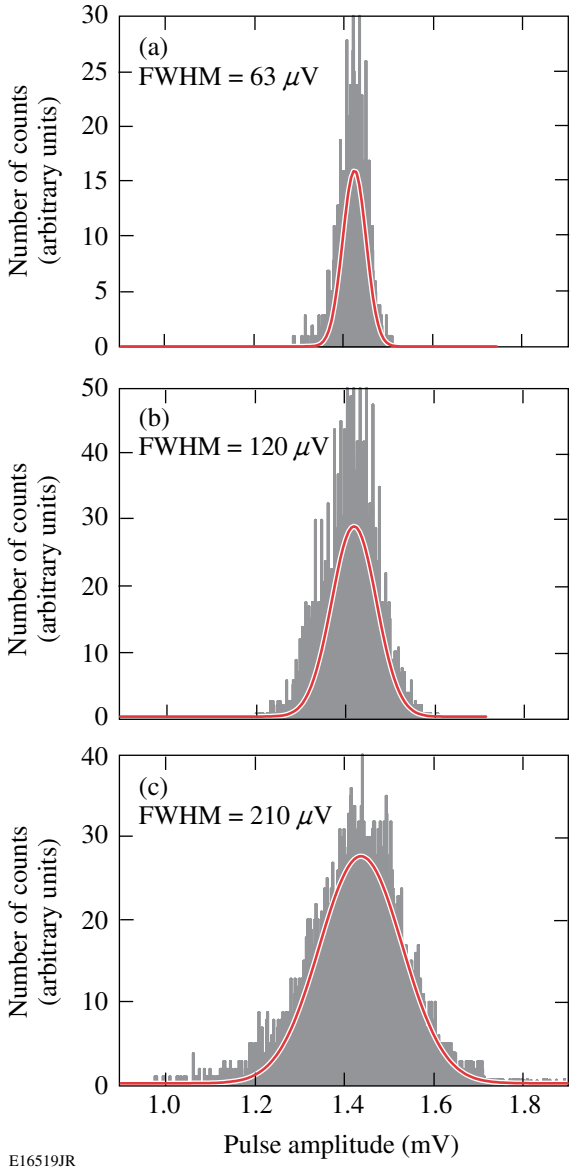

Figure 129.50
(a) Pulse-amplitude histograms of dark counts, (b) photon counts in the single-photon regime $n \sim 1$, and (c) multiphoton regime $n \geq 1$. All measurements performed the HEMT readout at 4.2 K and at $I_{bias} = 0.9\ I_c$. The SSPD output-voltage amplitudes are divided by the amplifier gain.

case of the conventional biasing technique, pulse amplitudes remain essentially constant, the HEMT readout allows one to record at least some quantitative differences between the different SSPD counting events.

For a more-quantitative analysis, a statistical approach was used to compute the distribution functions of amplitudes of pulses recorded under different experimental conditions. Figure 129.50 shows histograms that compare pulse-amplitude distributions of dark counts [Fig. 129.50(a)], as well as the photon counts collected at two different laser intensities [Figs. 129.50(b) and 129.50(c)]. All data were taken using the HEMT readout and in each case the SSPD was biased using $I_{bias} = 0.9\ I_c$. All histograms were fitted with a simple Gaussian function and it is clear that the dark counts [Fig. 129.50(a)] exhibit the narrowest full-width-at-half-maximum (FWHM) distribution. For the photon counts, we observe a widening of the Gaussian distribution as we move from the single-photon regime [$n \sim 1$; Fig. 129.50(b)] to the multiphoton case [$n \geq 1$; Fig. 129.50(c)]. In principle, the observed increase in the width of the Gaussian distribution for the photon counts could have resulted from excess shot noise. To verify this hypothesis, we have additionally recorded a histogram (Fig. 129.51) of output pulses collected when the SSPD was operated under the same

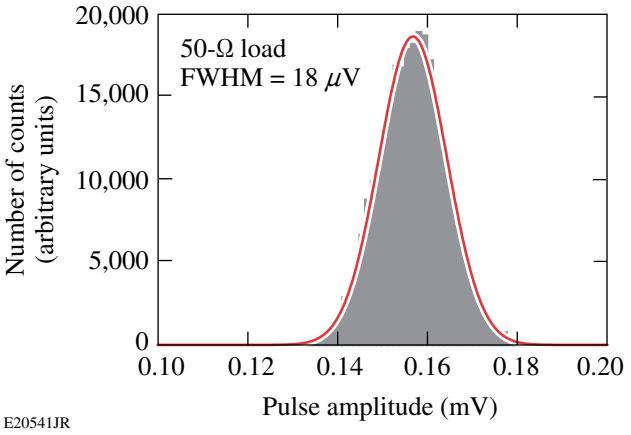

Figure 129.51
Pulse-amplitude histogram of photon counts in the single-photon regime ($n \sim 1$), when the SSPD was directly connected to the 50-Ω output coaxial line (no HEMT readout). All measurements were performed at 4.2 K and $I_{bias} = 0.9\, I_c$. The SSPD output-voltage amplitudes are divided by the amplifier gain.

conditions as in Fig. 129.50(b), namely, in the single-photon regime; however, in that case, our detector was directly connected to the 50-Ω output line. We note that the histogram shown in Fig. 129.51 exhibits almost a perfect Gaussian distribution with a very narrow, noise-delimitated width. Therefore, the impact of the shot noise is negligible and we can conclude that, indeed, the HEMT readout allows one to get at least a quantitative insight on the amplitude variations of the SSPD voltage output pulses, when the device is operated under different experimental conditions, e.g., the different incident photon flux levels.

A large number of histograms of the type presented in Fig. 129.50 have been collected under different SSPD biasing and optical illumination conditions. The correlation between the photon flux (average number of photons per pulse) incident upon the detector and the FWHM of the resulting distribution of the response pulse amplitudes was very reproducible and is summarized in Fig. 129.52, where the FWHM of the signal amplitude histograms versus the SSPD normalized current bias I_{bias}/I_c is presented, for both the dark counts (open squares) and the photon counts corresponding to the multiphoton ($n \geq 1$, closed triangles), single-photon ($n \sim 1$; open triangles), and heavily attenuated ($n \ll 1$; closed circles) illumination. We see that the dark-count signals exhibit the narrowest FWHM, which, in addition, is independent of the bias. Substantial differences also exist between the FWHM values corresponding to different incident photon fluxes. The general trend is that the distribution width increases with increasing I_{bias}/I_c, which is caused by the increased SSPD sensitivity in the $I_{bias} \approx I_c$

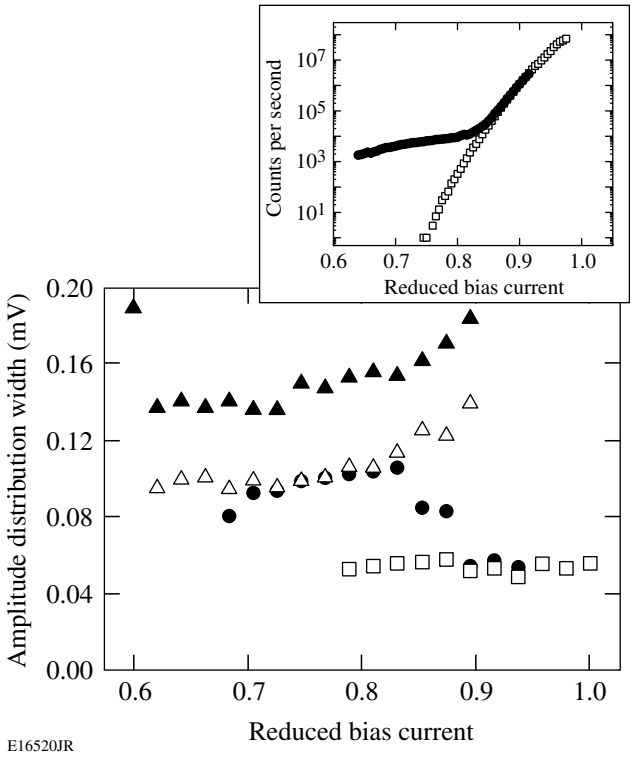

Figure 129.52
Amplitude distribution width (FWHM of Gaussian fits) for dark counts (open squares), $n \ll 1$ (closed circles), $n \sim 1$ (open triangles), and $n \geq 1$ (closed triangles). The inset shows the counting rate as a function of bias current for dark counts (open squares) and $n \ll 1$ (closed circles).

biasing regime, where even photons hitting the edges of the nanostripe are likely to be counted.[22] On the other hand, for a very low photon flux ($n \ll 1$; closed circles in Fig. 129.52), the amplitude distribution FWHM starts to drop around $I_{bias} = 0.83\, I_c$, eventually overlapping (open squares) at $I_{bias} > 0.9\, I_c$, as the dark counts dominate over the photon counts. The latter behavior agrees very well with our earlier observation[11] of the near-exponential dependence of the rate of dark counts in SSPDs on the I_{bias}/I_c ratio and their dominance in the $I_{bias} \approx I_c$ limit, as shown in the inset in Fig. 129.52.

The significant difference (a factor of several) in the FWHM values of the histograms for the dark- and photon-count events collected for the SSPD with the HEMT readout must have come from the intrinsic difference in the physics of triggering those counts. As demonstrated in Ref. 12, when a current-biased SSPD is blocked from all incoming radiation (shielded by a metallic enclosure) and placed in liquid helium, the spontaneous transient voltage pulses, or dark counts, are primarily caused by topological excitations. The thickness of the NbN stripe is 4 nm and the width is ~100 nm, which puts

the SSPD nanostripe in a two-dimensional (2-D) superconductor regime because its thickness is smaller, but the width is much larger than the NbN Ginsburg–Landau coherence length (~6 nm at $T = 0$ K). In 2-D systems in general, true long-range superconducting order is not possible, and in an ultrathin film, topological excitations come in the form of VAP's.[23] At typical SSPD operating temperatures far below T_c and in the absence of I_{bias}, all VAP's are bound and there is no dissipation in the NbN stripe. Once I_{bias} is applied, it exerts a Lorentz force on the VAP's, and at I_{bias} close to I_c, this force is strong enough to exceed the VAP binding energy and to break them. The latter effect creates free vortices and antivortices—analogue to excited electrons and holes in semiconductors—and allows them to move in opposite directions toward the edges of the NbN stripe, causing dissipation and resulting in the resistive state.[24] Since the VAP breaking events originate exclusively at the "weakest" (narrowest and/or localized) constriction spots of the SSPD meander, the normal region produced from these events is going to have only minimal variations in the resistance and, consequently, the histogram of the corresponding voltage pulses is expected to exhibit a very narrow distribution.

The fact that the photon-count amplitude distributions have FWHM's consistently wider than those corresponding to the dark counts (even in the single-photon regime) can be well understood based on the hot-spot–driven photon-detection events. Photon absorption and resulting hot-spot formation can happen at any point along the meander, leading to natural variations in the size of the resistive state.[22] Since the device I_c is determined by the narrowest and thinnest section(s) of the stripe, fabrication-related fluctuations in the stripe's cross section (variations in the width and/or thickness of the NbN stripe very likely to occur in our relatively low-QE SSPD's) must lead to the R_{hs} variations, which, in the case of our HEMT readout scheme, will be detected as the amplitude spread of photon-count responses. Finally, when the light intensity is relatively high ($n \geq 1$), multiphoton-absorption events are likely to happen, especially for I_{bias} approaching I_c, as more sections of the SSPD meander are activated. As a result, we should observe enhanced fluctuations in the response pulse amplitudes and, correspondingly, to the widest distribution FWHM, as, indeed, is presented in Figs. 129.50(c) and 129.52.

Toward Photon-Number Resolution

As mentioned before and predicted in Ref. 14, the integrated, cryogenic HEMT readout should not only allow one to distinguish dark counts from photon counts but also enable one to achieve PES and PNR in SSPD's. According to Ref. 14, a clear, real-time resolution between, e.g., the single- and two- or three-photon events, requires $R_L \gg R_{hs}$. Since in our HEMT readout R_L is fixed and equal to 500 Ω, the latter condition is not fulfilled in our experiments, as already discussed in **Device Description and Experimental Setup**, p. 40, and we have to restrict ourselves to the statistical, post-processing analysis. Such an approach is obviously not practical for, e.g., optical quantum computing but can find extended applications in spectral characterization of unknown ultraweak light sources in astronomical observations.

We have already successfully implemented the statistical approach to demonstrating the SSPD PES capability in conventionally biased devices, where, by measuring the SSPD system's detection efficiency at different bias currents, we were able to resolve the wavelength of the incident photons with a resolution of 50 nm (Ref. 5). Using the statistical method, we have also demonstrated earlier that SSPD's operating in the HEMT readout configuration are able to distinguish photons of different energies.[13] Therefore, here we focus on the PNR capability of an SSPD connected directly to HEMT.

As stressed before, in the case of devices with $I_c \approx 5\ \mu$A and the HEMT $R_L = 500\ \Omega$, one should still be able to distinguish, at least qualitatively, between the single- and multiphoton events. Indeed, when the laser intensity and I_{bias} were increased so that the detector started to register nearly every incident light pulse while the dark counts were still low, one could observe that, in time-domain traces of the photoresponse counts, some pulses exhibited visibly higher amplitudes than the rest. Figure 129.53 shows an example of such a real-time trace, which although convincing, is absolutely insufficient to conclude that these large pulses were indeed caused by double-photon events, instead of, e.g., a single-photon event arriving close in time to a dark-count event, or even resulting from a large inhomogeneity of the meandering stripe. It was, therefore, again necessary to look at the statistics of the pulse-amplitude distributions. This time, both the intensity of laser pulses and I_{bias} were varied for each case, and amplitudes of several million pulses were collected. Ultraviolet photons (frequency-tripled Ti:sapphire beams) were used to increase the photon-detection efficiency of the SSPD.

The results are presented in Fig. 129.54. When $I_{bias} \approx 0.7\ I_c$, the amplitude distribution can be fit with a simple Gaussian function, as shown in Figs. 129.54(a) and 129.54(b). Once I_{bias} reached $0.9\ I_c$, however [as shown in Figs. 129.54(c) and 129.54(d)], one could see a spreading of the distribution, which now had to be fit with two Gaussians. Although the two-Gaussian distribution can be explained as a result of

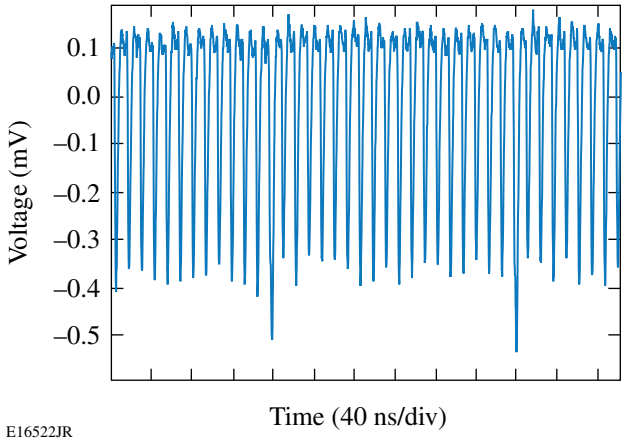

Figure 129.53
Live oscilloscope time-domain trace, showing higher amplitudes of some pulses.

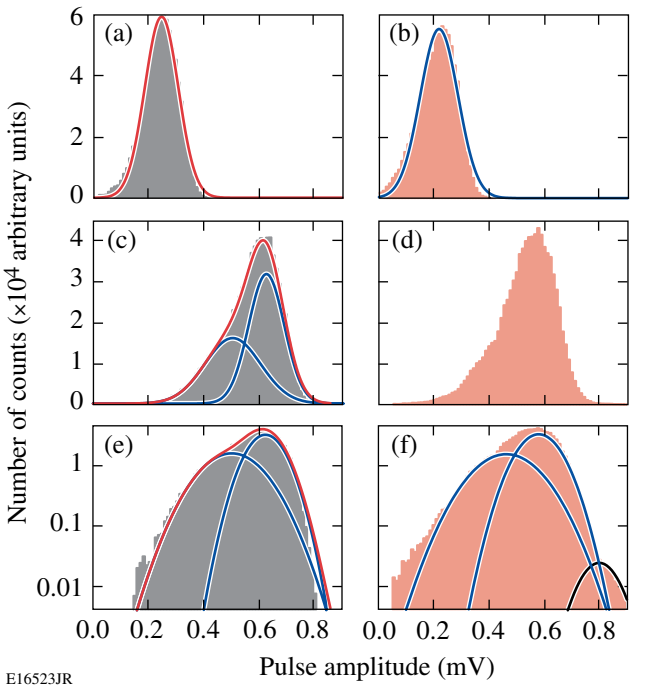

Figure 129.54
Pulse-amplitude histograms for (a) $n \ll 1$, $I_{bias} = 0.7\ I_c$; (b) $n \leq 1$, $I_{bias} = 0.7\ I_c$; (c) $n \ll 1$, $I_{bias} = 0.9\ I_c$; (d) $n \leq 1$, $I_{bias} = 0.9\ I_c$; (e) semi-log plot of (c); and (f) semi-log plot of (d). Gray histograms indicate the same incident photon flux for the $n \ll 1$ regime; red histograms indicate the same incident photon flux for the $n \leq 1$ regime.

significant nonuniformity variations of the NbN stripe rather than the PNR phenomenon, a more-detailed analysis of the presented plots favors the PNR interpretation. Figures 129.54(e) and 129.54(f) show the same data as Figs. 129.54(c) and 129.54(d), respectively; however, they are replotted on a semi-log scale. In Fig. 129.54(f) one can notice that, in the single-photon $n \leq 1$ regime, there is actually a third small Gaussian peak. This peak, however, is completely absent in the $n \ll 1$ regime [Fig. 129.54(e)], as well as when I_{bias} is far below I_c [Figs. 129.54(a) and 129.54(b)]. This third peak also cannot be a result of dark counts since the dark counts are most pronounced in the case of $n \ll 1$ illumination, as demonstrated in Fig. 129.52. Taking into account that the mean amplitude of this third Gaussian peak is the largest, the most-reasonable, although tentative, explanation is that it is indeed a result of the SSPD detection of multiphoton events. Further analysis is needed, however, to either support or disprove this conclusion.

Conclusion

In conclusion, we were able to observe the difference between dark counts and photon counts generated in our meander-type NbN SSPD's by utilizing an HEMT readout technique and, subsequently, examining distribution widths of the histograms of amplitudes of the collected in real-time dark- and photon-count signals. The distribution width for the dark count events was very narrow and independent of the bias current, while the FWHM of the distribution in the case of photon counts was up to 4× wider and was directly related to the photon flux (the average number of photons per pulse) incident on the SSPD. The differences in the measured FWHM values of the output-pulse distributions could be satisfactorily explained by the different physical origin of the dark-count events (VAP breaking and Lorentz-force dissipation) and the photon-count events (photon-induced hot-spot formation). It has also been demonstrated that the HEMT readout offers a promise of PNR functionality in SSPD measurements. The next step in this direction is likely to come from implementing ferromagnet/superconductor bilayer nanostripes (e.g., NiCu/NbN heterostructures), which are not only characterized by picosecond quasiparticle-phonon relaxation dynamics but also exhibit almost an order-of-magnitude larger superconductor critical-current densities.[25]

ACKNOWLEDGMENT

The authors thank Prof. G. Gol'tsman and his group at the Moscow State Pedagogical University for their assistance in the sample preparation and Prof. H. Mooij for very helpful discussions. Research in Warsaw was supported by the Polish Ministry of Science under Project No.4426/B/TO2/2007/33. R. S. thanks the Spanish Ministry of Education and the University of Salamanca for their financial support and hospitality during his one-semester-long research visit in Salamanca, Spain.

REFERENCES

1. W. Słysz, M. Węgrzecki, J. Bar, P. Grabiec, M. Górska, V. Zwiller, C. Latta, P. Böhi, A. J. Pearlman, A. S. Cross, D. Pan, J. Kitaygorsky, I. Komissarov, A. Verevkin, I. Milostnaya, A. Korneev, O. Minayeva, G. Chulkova, K. Smirnov, B. Voronov, G. N. Gol'tsman, and R. Sobolewski, J. Mod. Opt. **54**, 315 (2007).

2. C. Bennett and G. Brassard, in *International Conference on Computers, Systems, and Signal Processing* (IEEE Computer Society, IEEE Circuits and Systems Society, and Indian Institute of Science, Bangalore, India, 1984), pp. 175–179.

3. E. Waks, A. Zeevi, and Y. Yamamoto, Phys. Rev. A **65**, 052310 (2002).

4. E. Knill, R. Laflamme, and G. J. Milburn, Nature **409**, 46 (2001).

5. E. Reiger, S. Dorenbos, V. Zwiller, A. Korneev, G. Chulkova, I. Milostnaya, O. Minaeva, G. Gol'tsman, J. Kitaygorsky, D. Pan, W. Słysz, A. Jukna, and R. Sobolewski, IEEE J. Sel. Top. Quantum Electron. **13**, 934 (2007).

6. Y. Kang *et al.*, Appl. Phys. Lett. **85**, 1668 (2004).

7. G. Ribordy *et al.*, J. Mod. Opt. **51**, 1381 (2004).

8. G. N. Gol'tsman, O. Okunev, G. Chulkova, A. Lipatov, A. Semenov, K. Smirnov, B. Voronov, A. Dzardanov, C. Williams, and R. Sobolewski, Appl. Phys. Lett. **79**, 705 (2001).

9. K. M. Rosfjord *et al.*, Opt. Express **14**, 527 (2006).

10. J. Kitaygorsky, J. Zhang, A. Verevkin, A. Sergeev, A. Korneev, V. Matvienko, P. Kouminov, K. Smirnov, B. Voronov, G. Gol'tsman, and R. Sobolewski, IEEE Trans. Appl. Supercond. **15**, 545 (2005).

11. A. Engel *et al.*, Phys. Stat. Sol. C **2**, 1668 (2005).

12. J. Kitaygorsky, I. Komissarov, A. Jukna, D. Pan, O. Minaeva, N. Kaurova, A. Divochiy, A. Korneev, M. Tarkhov, B. Voronov, I. Milostnaya, G. Gol'tsman, and R. Sobolewski, IEEE Trans. Appl. Supercond. **17**, 275 (2007).

13. J. Kitaygorsky, S. Dorenbos, E. Reiger, R. Schouten, V. Zwiller, and R. Sobolewski, IEEE Trans. Appl. Supercond. **19**, 346 (2009).

14. M. G. Bell *et al.*, IEEE Trans. Appl. Supercond. **17**, 289 (2007).

15. G. N. Gol'tsman, K. Smirnov, P. Kouminov, B. Voronov, N. Kaurova, V. Drakinsky, J. Zhang, A. Verevkin, and R. Sobolewski, IEEE Trans. Appl. Supercond. **13**, 192 (2003).

16. W. Słysz, M. Węgrzecki, J. Bar, P. Grabiec, M. Górska, V. Zwiller, C. Latta, P. Bohi, I. Milostnaya, O. Minaeva, A. Antipov, O. Okunev, A. Korneev, K. Smirnov, B. Voronov, N. Kaurova, G. Gol'tsman, A. Pearlman, A. Cross, I. Komissarov, A. Verevkin, and R. Sobolewski, Appl. Phys. Lett. **88**, 261113 (2006).

17. A. J. Kerman *et al.*, Appl. Phys. Lett. **88**, 111116 (2006).

18. J. K. W. Yang *et al.*, IEEE Trans. Appl. Supercond. **17**, 581 (2007).

19. A. VI. Gurevich and R. G. Mints, Rev. Mod. Phys. **59**, 941 (1987).

20. T. Taneda, G. P. Pepe, L. Parlato, A. A. Golubov, and R. Sobolewski, Phys. Rev. B **75**, 174507 (2007).

21. D. Pan, G. P. Pepe, V. Pagliarulo, C. De Lisio, L. Parlato, M. Khafizov, I. Komissarov, and R. Sobolewski, Phys. Rev. B **78**, 174503 (2008).

22. A. Pearlman, A. Cross, W. Słysz, J. Zhang, A. Verevkin, M. Currie, A. Korneev, P. Kouminov, K. Smirnov, B. Voronov, G. Gol'tsman, and R. Sobolewski, IEEE Trans. Appl. Supercond. **15**, 579 (2005).

23. J. E. Mooij, in *Percolation, Localization, and Superconductivity*, edited by A. M. Goldman and S. A. Wolf, NATO ASI, Series B, Vol. 109 (Plenum Press, New York, 1984), pp. 325−370.

24. A. M. Kadin, J. Appl. Phys. **68**, 5741 (1990).

25. N. Marrocco, G. P. Pepe, A. Capretti, L. Parlato, V. Pagliarulo, G. Peluso, A. Barone, R. Cristiano, M. Ejrnaes, A. Casaburi, N. Kashiwazaki, T. Taino, H. Myoren, and R. Sobolewski, Appl. Phys. Lett. **97**, 092504 (2010).

Thermal Conductivity of Solid Deuterium by the 3ω Method

Introduction

Targets for inertial confinement fusion (ICF) require layers of solid D_2 or DT that have been formed and smoothed by sublimation and recondensation.[1] This "layering" process,[2,3] which typically takes hours, can result in a variety of internal structures in the layer that constitute departures from the desired uniformity of the layer. Knowing the thermal conductivity of the layer and how changes in structure may alter the conductivity are important to modeling the layering process.[4] Although the layering process is most easily accomplished at a temperature just below the triple point, optimizing the internal gas density of the target for ICF requires a temperature ~1.5 K below the triple point.[5] Lowering the temperature after obtaining a uniform layer can result in significant thermal contraction of the layer. This contraction can produce stresses and cracks because the solid D_2 is not free-standing but is attached to a plastic spherical surface.

A critical requirement for ICF experiments is achieving a uniformly thick shell of ice inside a spherical capsule. Analysis of the crystalline structure shows this ice layer to be hexagonally close-packed.[6] In this ice configuration heat is conducted radially out of the sphere along the *a* plane of the crystal over most of the sphere, and along the *c* axis over the remainder of the sphere. Should the thermal conduction along the *c* axis and the *a* plane be significantly different, the ice layer would have an intrinsic limit as to how uniform it could be.

In the 3ω method of measuring thermal conductivity, a wire or strip line whose resistivity is a strong function of temperature is employed as both the heater and the temperature sensor.[7–11] A sinusoidal current with angular frequency $\omega = 2\pi f$ passes through a wire or strip line that is embedded in or thermally anchored to the medium whose thermal conductivity is to be measured. Heat generated in the wire is proportional to the square of the current and therefore has a frequency component at 2ω in addition to a steady-state component, resulting in a temperature with an oscillating component at 2ω. If the wire is a high-purity metal such as Pt, its resistance varies strongly with temperature (for the wire used here, the resistance variation is 5% to 7% per K). Accordingly, the resistance also has an oscillating component at frequency 2ω. The resulting voltage between two points on the wire (the product of current at frequency ω and resistance) therefore has a component of amplitude V_ω at frequency ω and a small component of amplitude $\tilde{V}_{3\omega}$ at frequency 3ω. [See Eqs. (6)−(9) of Ref. 8.] The component $\tilde{V}_{3\omega}$ is expressed as a complex amplitude to take into account the phase shift (with respect to the fundamental, after tripling its frequency) resulting from thermal inertia in the wire and in the medium. It is straightforward to show that the amplitude $\tilde{T}$ of temperature variation in the wire is proportional to $\tilde{V}_{3\omega}$,

$$\tilde{T} = 2\frac{\tilde{V}_{3\omega}}{V_\omega}\frac{R}{\mathrm{d}R/\mathrm{d}T}, \tag{1}$$

where R is the resistance of the wire (between the voltage leads) at the ambient temperature T. Equation (1) is equivalent to Eq. (12) of Cahill (as corrected in the erratum)[7] and is implicitly given in Eq. (9) of Birge *et al.*[8] This equation is valid even if there is a small temperature variation along the wire and, in that case, gives the average temperature amplitude. Since the temperature amplitude $\tilde{T}$ depends strongly on the amount of heat conducted away by the medium, it can be used as a measure of the thermal conductivity of the medium. By making the wire one arm of a bridge circuit, sensitivity to V_ω is minimized and $\tilde{V}_{3\omega}$ can be amplified and measured with a lock-in amplifier. In this work, the principal source of error is noise in the first stage of amplification, which is partially overcome by using the lock-in amplifier to achieve a narrow bandwidth and a long averaging time.

Cahill introduced the useful concept of "thermal penetration depth," which gives an estimate of the distance that a temperature oscillation penetrates into the medium. This quantity is given by $\left[\kappa/(2\rho\omega C)\right]^{1/2}$, where κ is the thermal conductivity in the medium, ρ is the density, and C is the specific heat.[7] This indicator of how far the wire must be from other parts of the apparatus is in agreement with temperature distributions in the medium calculated by the numerical model described in **Numerical Model**, p. 51.

A more-conventional method for measuring thermal conductivity is imposing a thermal gradient on a bulk sample and measuring the resulting heat flow. A drawback to this method for D_2 is the shrinkage (a 14% increase in density upon solidification and an additional 3% upon cooling from the triple point to 10 K) pulling the medium out of contact with one of the heating or sensing elements. This problem was discussed by Collins *et al.*[12] and Souers.[13] Daney[14] overcame this problem by observing the rate of ice growth on a cooled rod immersed in liquid and inferring the thermal conductivity from that rate. In the method used here, the solid forms around a wire of very small diameter (15 μm). Shrinkage upon further cooling may produce stresses in the solid D_2, but it is not expected to pull the D_2 away from the wire. This expectation is confirmed by observation [see later in Fig. 129.60(c)]. Conventional measurements of the thermal conductivity of liquid are subject to errors caused by convection. The high-frequency method used here should be virtually immune to convection issues.

Some proposed targets for ICF use solid D_2 or DT inside low-density polymer foam. Liquid D_2 soaks readily into such foams,[15] and it was found (using silica aerogel foam) by Daney and Mapoles[16] that the thermal conductivity of liquid in foam is very close to that of liquid by itself. When the liquid solidifies, voids may develop that affect both the thermal conductivity and the performance of ICF foam targets. The presence of a sizeable void content could be confirmed by embedding a wire in the foam and measuring its thermal conductivity by the 3ω method.

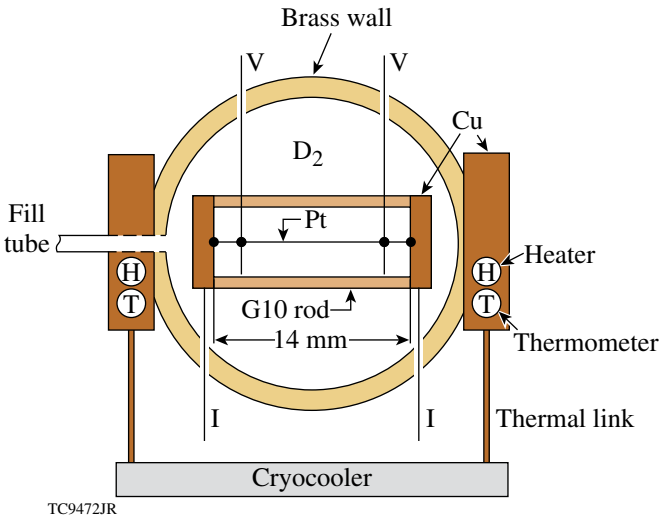

Figure 129.55
Apparatus employed to measure the thermal conductivity of D_2. Glass windows parallel to the plane of this figure allow one to observe the condensation and solidification process. The Pt wire is 1.0 mm from one window, 1.8 mm from the other window, and 2.8 mm from the G10 rods. Copper blocks on either side of the brass chamber have heaters (H) and thermometers (T) that allow one to impose a thermal gradient during the solidification process. Thermal links to the cryocooler are sized to provide adequate cooling, while allowing for a sufficient thermal gradient during the solidification process. The voltage leads (V) and current leads (I) exit the chamber through vacuum feedthroughs.

Experimental Setup

The active element used in this work is a 15.0±0.2-μm-diam Pt wire (measured by a scanning electron microscope). The wire is annealed and is of 99.99% purity.[17] As shown in Fig. 129.55, the Pt wire is soldered to Cu blocks 14 mm apart and attached to voltage leads (25-μm-diam stainless steel). The Cu blocks are held apart by G10 rods (insulating polymer-glass composite) that also provide support for the voltage leads. The voltage leads are attached to points on the Pt wire ~10 mm apart, either with solder or electrically conductive epoxy. Care is taken to avoid flexing or stretching of the Pt wire and to minimize the mass of the connection to the voltage leads. To minimize stresses on the Pt wire, a three-axis positioner is used to mount the Pt wire and to solder the voltage leads to it. After assembly, the distances between the attachment points are precisely measured using a micrometer stage under a microscope. Although the stainless steel of the voltage leads is more thermally conductive than the D_2 (by a factor of ~6 for solid D_2 at the triple point), its heat capacity is small and its thermal conductivity is a factor of ~30 smaller than that of the Pt. The voltage leads are assumed not to be a significant thermal perturbation to the experiment.

The resistance R of the Pt wire was measured as a function of temperature (T), since an accurate knowledge of $R/(\mathrm{d}R/\mathrm{d}T)$ is required to determine the temperature amplitude. A third-order polynomial provides a good fit to the resistance as a function of temperature, as seen in Fig. 129.56. Of five Pt wires used at different times, three agreed in resistance per unit length over the experimental temperature range (11 K to 26 K), while two wires showed slightly greater resistance. It is likely that mechanical flexing and stretching in the course of mounting these delicate wires sometimes resulted in increased resistance. In one instance, the wire was noticeably deformed by the rapid melting of solid D_2 and thereafter exhibited increased resistance. The thermal conductivity of the Pt wire as a function of temperature is obtained from the Metalpak program of Arp,[18] based on the residual resistance ratio (RRR) of the Pt wire (i.e., the ratio of resistance at 273 K to the resistance at a temperature ≤4 K). The value of RRR was determined by measuring the ratios of resistance at 294 K to the resistance values in the range 14 K to 18 K and comparing these ratios to the corresponding ratios given by Ref. 18. This procedure

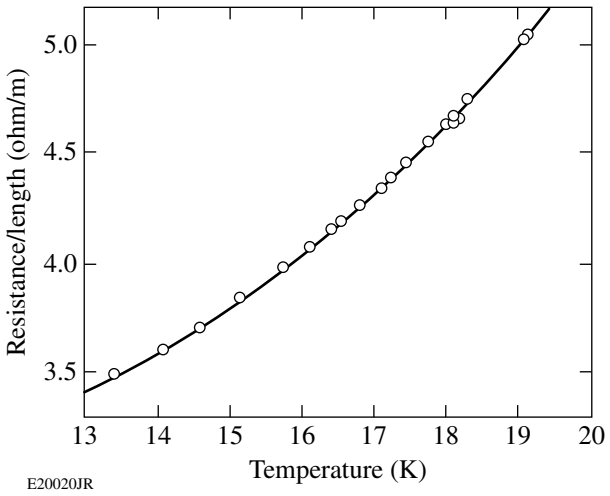

Figure 129.56
Resistance per unit length of a Pt wire as a function of temperature. The measured data are fit with a third-order polynomial.

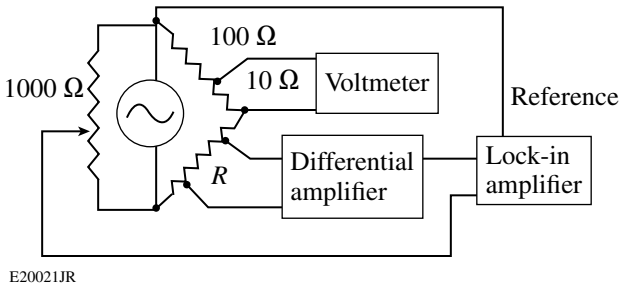

Figure 129.57
Circuit for measuring thermal conductivity. The voltmeter monitors current through the Pt-wire sample resistance *R*. The bridge is balanced with the lock-in amplifier set to detect the fundamental frequency, and the output of the oscillator (which is internal to the lock-in amplifier) is attenuated. After balancing the bridge at a single frequency, the lock-in amplifier is reset to detect the third harmonic. A LabVIEW program collects and averages data at a series of frequencies. No bandwidth limitations are imposed in amplification since these would produce phase shifts. The differential amplifier is Stanford Research Systems model SR560, and the lock-in amplifier (which also uses a differential input) is model SR830.

yields RRR = 186 to 196 and Pt conductivity values ranging from 350 W/(m K) at 18 K to 410 W/(m K) at 14 K. The range of values for RRR produces ≤2% uncertainty in the Pt thermal conductivity values and does not add any uncertainty to the thermal conductivity values obtained for solid D_2.

The chamber in Fig. 129.55 consists of a vacuum-tight brass cylinder with electrical feedthroughs soldered in and glass windows sealed to the chamber by compression of indium gaskets. The windows allow one to backlight and image the D_2 liquid or solid. Materials were chosen that would provide the thermal gradients necessary to fill the chamber with solid deuterium. Copper blocks of high purity on each side of the brass cylinder have very high thermal conductivity compared with the brass and glass (by a factor of >10) and facilitate establishing and measuring the thermal gradient. The experimental chamber is thermally linked to the cold finger of the cryostat. The thermal links are somewhat weak to allow one to impose a thermal gradient, using heaters. After the heaters are turned off and temperatures stabilize, a small thermal gradient of ~0.2 K/cm remains in the region of the apparatus containing the Pt wire. This gradient is a consequence of the necessary weakness of the thermal links to the cold finger and not a significant source of experimental error. The experimental chamber is surrounded by a copper radiation shield at 40 K. Windows in the radiation shield are coated with ~10 nm of Au to reduce thermal radiation coming into the chamber.

The electrical configuration is shown in Fig. 129.57. After stabilizing the temperature in the D_2, the resistance of the Pt wire between the voltage leads is determined. The bridge circuit is then balanced by manually adjusting the variable resistor, while the lock-in amplifier is set to detect the fundamental frequency of the sine-wave oscillator. A single frequency is used to determine resistance and balance the bridge; these functions are found to be insensitive to the choice of this frequency. The oscillator, internal to the lock-in amplifier, is of high spectral purity, with harmonic distortion of −80 dB (Ref. 19). It is assumed that any component of distortion at frequency 3ω is partially removed by balancing the bridge. Replacing the Pt wire by a Cu wire at room temperature with a similar resistance demonstrates that the influence of oscillator distortion is insignificant. Some measured values of $\tilde{V}_{3\omega}$ for solid D_2 at <17 K are as small as 17 nV (rms), which is 96 dB below the value of V_ω, i.e., 1.1 mV (rms).

To obtain a value of thermal conductivity, the third-harmonic voltage $\tilde{V}_{3\omega}$ is measured as a function of frequency. Each value of voltage is recorded as a complex number, the values in phase or out of phase with the driving current. Holding the ambient temperature constant, data are taken at a series of frequencies increasing at logarithmic intervals from ~1 Hz to >1000 Hz. This scan typically takes 2 to 20 min and is repeated to ensure that the state of the solid D_2 has not changed. The data at each frequency are averaged, after an initial settling time that is governed by the time constant selected on the lock-in amplifier. Some scans are rejected after finding that the state of the solid D_2 has apparently changed between the first and second scans. Non-repeatable scans are found to be especially likely if there is a visible crack or cavity somewhere in the solid D_2.

In such a case, heat generated in the Pt wire hollows out a new cavity around the wire itself, and the gas that is generated is able to find a path to the original cavity and recondense there. When large enough, a cavity around the wire becomes visible through a microscope with an attached video camera. When a cavity develops around the wire, there is a sudden rise in the in-phase temperature amplitude, and the data are rejected.

Data are fitted with the two-dimensional (2-D) numerical model described in **Numerical Model**, which includes, as input parameters, the dimensions of the wire and the medium, the density, specific heat and thermal conductivity of Pt,[18] and the density,[20] specific heat,[21,22] and thermal conductivity of D_2. The latter five parameters are highly temperature dependent. The only fitting parameter is the thermal conductivity of the D_2 since the other parameters are presumed to be known to sufficient accuracy. At the temperatures employed here, the heat capacity per unit volume of the liquid or solid D_2 is a factor of 4 to 7 greater than that of the wire. These ratios, much greater than those often found with other materials at higher temperatures, facilitate the measurement by overcoming the loss of sensitivity resulting from the very small wire resistance. If the voltage leads are located sufficiently far from the ends of the wire, the numerical model yields results very close to the analytical solution [Eq. (21)] of Chen *et al.*[9] for a one-dimensional (1-D) problem where it is assumed that the wire is infinitely long (i.e., no heat flow in the direction of the axis of the wire) and that the wire has a much greater thermal conductivity than the surrounding medium.

To maintain purity of the D_2 against possible contamination by air or other gases, impurities are removed with each cryogenic cycle. Between uses, the D_2 is stored as a room-temperature gas at ~1 atm. After condensing the D_2 in the experimental chamber and taking data, the chamber is warmed to ~30 K, evaporating the D_2, but leaving residual air (if any) frozen. After isolating the D_2 and warming the apparatus, the contaminants are pumped away.

For some of the data, the D_2 was converted from normal D_2 to ortho D_2 using a catalyst. To achieve this conversion, the D_2 was first condensed into a separate chamber of volume 5 cm^3 containing 2 g of hydrated iron oxide[23] (catalyst grade, 30/50 mesh). Prior to cooling, the catalyst was baked in vacuum (150°C for ~2 h, until the outgassing rate became small). The D_2 was kept in this chamber for several days as liquid just above the triple point, while the adjacent experimental chamber was kept several K higher to prevent any condensation there. After several days, it was presumed that all the D_2 had been converted[24] to ortho D_2. Some of the D_2 was then distilled into the experimental chamber (volume 0.9 cm^3) by reversing the relative temperatures of the two chambers.

Numerical Model

A computer program modeled this experiment to relate the measured temperature amplitude to the thermal conductivity in the medium. The model takes into account the 2-D geometry of the experiment and includes thermal conduction along the wire, as well as conduction in the medium both perpendicular and parallel to the wire. This model has been used to determine the significance of 2-D effects and to provide improved accuracy over 1-D numerical solutions, which ignore heat flow in the direction of the wire axis.

The 2-D domain used by the model is shown in Fig. 129.58. The model assumes a cylindrically symmetric (r,z) geometry consisting of the wire, the medium, and surrounding heat baths. While the distance from the wire to the boundary varies from 1 to 3 mm in the experiment (see Fig. 129.55), the cylindrical geometry is valid for all but the lowest frequencies because the oscillating temperature T falls to zero within distances significantly less than 1 mm. The radius of the wire (7.5 μm) is small when compared with the radial width of the outer boundary (1 mm); therefore, a variable-size grid was implemented in the medium, wherein the radial widths of the cells increase geometrically with their distance from the wire. The cell widths in z are kept uniform for all media. The model is similar to that presented in Jacquot *et al.*,[25] who performed

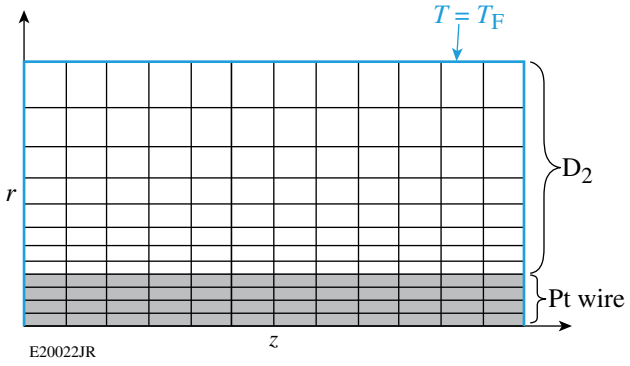

Figure 129.58
Schematic of the 2-D domain used by the numerical code. The Pt wire (shaded region) is fine zoned in the radial direction, matched to variable zoning in the D_2. Azimuthal symmetry is assumed with a fixed temperature $T = T_F$ specified on each of the three boundaries. An oscillatory current is applied uniformly through the wire. The code solves a 2-D diffusion equation for the complex 2ω temperature component.

initial-value heat-flow calculations in a different geometry for a 3ω experiment using a rectangular metal strip as the heater placed on top of the sample.

To achieve accurate solutions, 50 uniformly spaced cells were used in the axial direction, with >400 uniformly spaced radial cells in the wire and 1300 geometrically spaced cells in the medium. The large number of radial cells in the wire was required to ensure continuity of cell size across the wire–medium boundary. Small cells in the medium close to the wire are required to resolve the spatial variations at high frequencies. The average of the Pt and D_2 conductivities is used at the Pt–D_2 boundary. There is no heat flux across the lower boundary of the Pt wire (the z axis). The temperature T is fixed on the three sides of the domain that are heat baths. The heat source is nonzero only for in Pt cells.

For each cell

$$\rho C \frac{\partial T}{\partial t} + \nabla \cdot Q = W \tag{2}$$

is solved, where the heat flux Q is given by $Q = -\kappa \nabla \mathrm{T}$ and W is the heat deposited in the wire per unit volume. The code can solve Eq. (2) as an initial-value problem using a conventional finite-difference technique. Energy conservation is ensured by expressing the heat flux between two cells as a quantity proportional to the difference in temperature between the cells. Implicit differencing of Eq. (2) leads to a matrix equation for the new temperature T of the form $MT = S$, where M is a five-diagonal matrix and S is a vector evaluated at the previous time step. The matrix equation is solved using Kershaw's incomplete Cholesky conjugate gradient (ICCG) method.[26] Details of the numerical implementation are given in Ref. 27. Since it would be excessively time consuming to solve the initial value problem for the present experiment, where the asymptotic second-harmonic response to the oscillating current is required, an alternative approach is used that yields the oscillating temperature amplitude $\tilde{T}(r,z)$ directly. Assuming that the current varies as $\cos(\omega t)$, the heat deposition W may be written as

$$W(t) = W_0 + \frac{1}{2}\left(\tilde{W} e^{i2\omega t} + \tilde{W} e^{-i2\omega t}\right), \tag{3}$$

where W_0 is the time-averaged deposition and $\tilde{W} = W_0$. The asymptotic temperature is then given by

$$T(r,z,t) = T_0(r,z) + \frac{1}{2}\left[\tilde{T}(r,z) e^{2i\omega t} + \tilde{T}^{*}(r,z) e^{-2i\omega t}\right], \tag{4}$$

where $T_0(r,z)$ is the steady-state solution satisfying $-\nabla \bullet (\kappa \nabla T_0) = W_0$. Inserting Eqs. (3) and (4) into Eq. (2), one finds

$$i\omega\rho C\tilde{T} - \frac{1}{2}\nabla \cdot \kappa \nabla \tilde{T} = \tilde{W}. \tag{5}$$

This equation is differenced as for the initial value solution, and $\tilde{T}(r,z) = 0$ is imposed on the physical boundaries. A similar five-diagonal matrix equation is obtained, but the central diagonal of the matrix contains complex numbers and the solution $\tilde{T}(r,z)$ is complex. It has been found[27] that Kershaw's ICCG method generalized to operate with complex numbers converges to provide the complex solution $\tilde{T}(r,z)$. Noting that the resistivity of the wire (which is linear in temperature over small-enough temperature excursions) has a second-harmonic component proportional to $\tilde{T}(r,z)$ and the resistance along the wire combines in series, it is easy to see that the third-harmonic voltage $\tilde{V}_{3\omega}$ is that given in Eq. (1), where $\tilde{T}$ is the average value of $\tilde{T}(r,z)$ between the two voltage leads. In practice, because of the high thermal conductivity and small radius of the Pt wire, the r dependence of $\tilde{T}(r,z)$ in the wire is very small and it is the z variations of $\tilde{T}(r,z)$ that determine the average.

By solving the initial value problem, it is found that the time taken for the wire to reach a constant ambient temperature in vacuum is <40 ms. Longer times are required for solid D_2, but over the several-minute averaging time of the measurement, transient effects are negligible. Figure 129.59 illustrates the use of the numerical model to obtain the spatial distribution of the temperature amplitude in the wire and in the medium. In Figs. 129.59(a) and 129.59(b), it is seen that thermal conduction along the wire reduces the temperature amplitude near the end of the wire, but that locating the voltage leads ~2 mm from the ends places them in a region of constant temperature amplitude. This constant amplitude is found to be the same (within 0.5%) as that calculated by the 1-D model [Eq. (21)] of Ref. 9. In Figs. 129.59(c) and 129.59(d), the radial temperature distribution in the wire and in the solid D_2 is shown [(c) in phase and (d) out of phase], starting from the mid-point of the wire. In Fig. 129.59(e) the in-phase temperature amplitude in the wire is magnified at a single frequency to show a 1-μK temperature drop between the center and the edge at 7.5 μm.

To understand departures of the experimental data from the numerical model, particularly at frequencies >1 KHz, two modifications were introduced. Neither of these yielded an improved fit to the observed data, but they are mentioned here as strategies available to users of the 3ω method. A thin layer of frozen air on the wire was added to the model but failed to

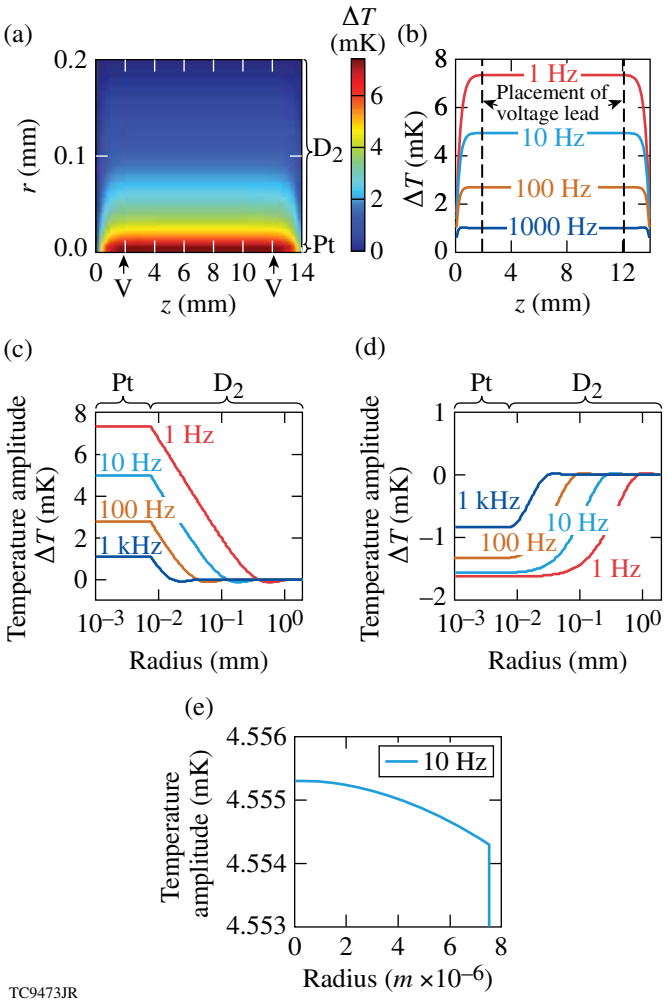

Figure 129.59
Illustrative results of the 2-D model. (a) Calculated contour plot of temperature amplitude (the in-phase component) in and around the Pt wire embedded in solid D_2 at 18 K. A sinusoidal current at 1 Hz results in dissipation of 45 μW between the voltage leads, labeled V. (b) In-phase temperature amplitude as a function of distance along the wire. (c) In-phase and (d) out-of-phase temperature amplitudes as a function of radial distance from the center of the wire starting at the mid-point of the wire. (e) Magnification of (c) showing a 1.0-μK drop in the temperature amplitude between the center and edge of the wire at 10 Hz.

improve the fit. Surface irregularities on the 1-μm level were added to the Pt wire but also failed to improve the fit.

Results

Before measurements on solid D_2 are undertaken, significant effort is required to obtain solid D_2 free of obvious cavities and cracks. The chamber is observed visually while liquid is condensing and then while solidification proceeds in the presence of an imposed thermal gradient. The solid grows slowly (over several hours) from the cold side to the warm side, with the liquid in the fill tube being the last to solidify. Because of the 14% increase in density upon solidification of the liquid D_2, gas cavities can easily be trapped in the solid. If this happens, the warm side is reheated until the cavities are filled with liquid, and the solidification process is then resumed. If cavities are allowed to remain, they can cause the thermal conductivity measurement to fail because they gradually move (by sublimation on the warm side of the cavity and recondensation on the cold side) in response to residual thermal gradients and often find their way to the Pt wire.

Before a measurement, the D_2 solid is evaluated visually as shown in Fig. 129.60. Figure 129.60(a) shows the interface between liquid and solid as the solid grows, and the resulting solid is shown in Fig. 129.60(b). Upon lowering the temperature of clear solid D_2 as seen in Fig. 129.60(b), many visual features appear, such as cracks and regions where the solid has apparently pulled slightly away from a window or the wire supports, as seen in Fig. 129.60(c). After remaining at a constant temperature for a period of several hours to a day, cracks and other features appear to heal, the solid again becomes visually clear, and a repeatable measurement of thermal conductivity can be made. The crystallinity of the solid is examined by viewing it in polarized light as shown in Figs. 129.60(d) and

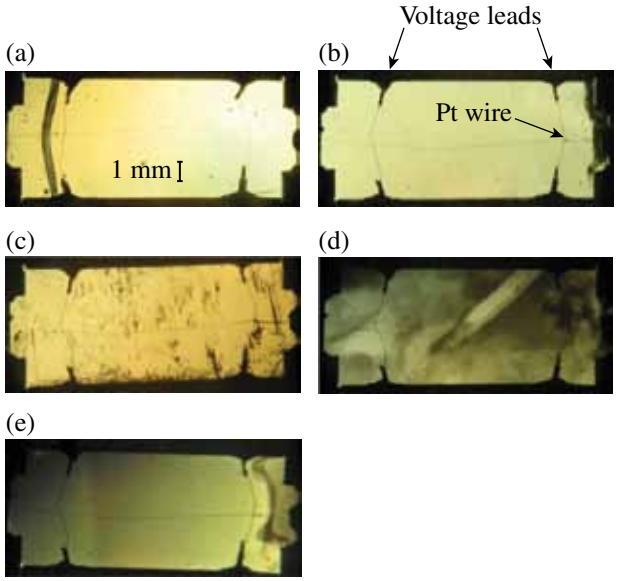

Figure 129.60
Various views of solid D_2 formed around the Pt wire and the voltage leads. (a) Solid forming on the left side with liquid on the right, in the presence of a thermal gradient. The dark line is caused by refraction at the interface between solid and liquid. (b) Solid successfully formed, free of apparent flaws. (c) Solid with cracks after suddenly lowering the temperature by 2 K. [(d) and (e)] Two examples of solid in polarized light revealing features of the crystallinity.

129.60(e). In both cases the solid was visually clear when viewed without polarizers and provided repeatable thermal conductivity data. Typically, several domains are seen, random in shape, with dimensions in the range of 1 to 8 mm. These domains are revealed by variations in color and shading as the polarizers are slowly rotated. It appears that the Pt wire passes through several large crystallites. If a single crystal could be grown around the Pt wire, conductivity might be measured as a function of crystal orientation.

To obtain a value of thermal conductivity at a particular temperature, temperatures are allowed to stabilize for 20 min or more. Using a constant current, $\tilde{V}_{3\omega}$ is measured at a series of frequencies and converted to temperature amplitude $\tilde{T}$ using Eq. (1). Typical results are shown in Fig. 129.61(a) for solid D_2, in Fig. 129.61(b) for liquid D_2, and in Fig. 129.61(c) for D_2 gas. Each pair of data points requires 20 to 60 s of averaging, which is performed by a LabVIEW[28] program. The variance in a typical averaged data point is usually consistent with the noise figure (4 nV/Hz$^{1/2}$) of the first stage of amplification.[19] The data in Fig. 129.61 are fitted, using the numerical model, varying only the thermal conductivity of the D_2. It is verified experimentally that the temperature amplitude is proportional to the power dissipated in the Pt wire, so the drive current is maximized (but without noticeably raising the ambient temperature measured on the chamber) to reduce the relative importance of amplifier noise.

For Figs. 129.61(a) and 129.61(b), the numerical model fits the in-phase data very closely from 1 Hz to >1000 Hz, while fitting the out-of-phase data over a smaller frequency range, ~8 Hz to ≥300 Hz. This is typical of many data sets. The reasons for the departures from the fit outside these frequency ranges are not known. Several authors[8,9] use the fitting process to also obtain the specific heat of the medium. This does not work for solid D_2 since varying the specific heat from the literature value simply requires a different value of thermal conductivity to fit the data. This is confirmed by the discussion in Ref. 9 that gives the range of parameters required for sensitivity to specific heat. The data obtained in this study are at frequencies too low to obtain specific heat values.

Data for D_2 gas around the Pt wire show acceptable qualitative fits, as seen in Fig. 129.61(c). As expected, the smaller thermal conductivity of the gas yields much greater thermal amplitudes and the curves differ in shape from those of liquid and solid. In this case, much of the heat dissipated in the Pt wire is conducted along the wire to the ends. To use this method to measure the thermal conductivity of a gas would require extra care in establishing the temperature of the Cu blocks at the ends of the Pt wire, and a greater distance from the wire to other parts of the apparatus would be helpful. Additional discussion of the data for D_2 gas and similar data for vacuum, including temperature profiles along the wire and in the gas, is presented in Ref. 27.

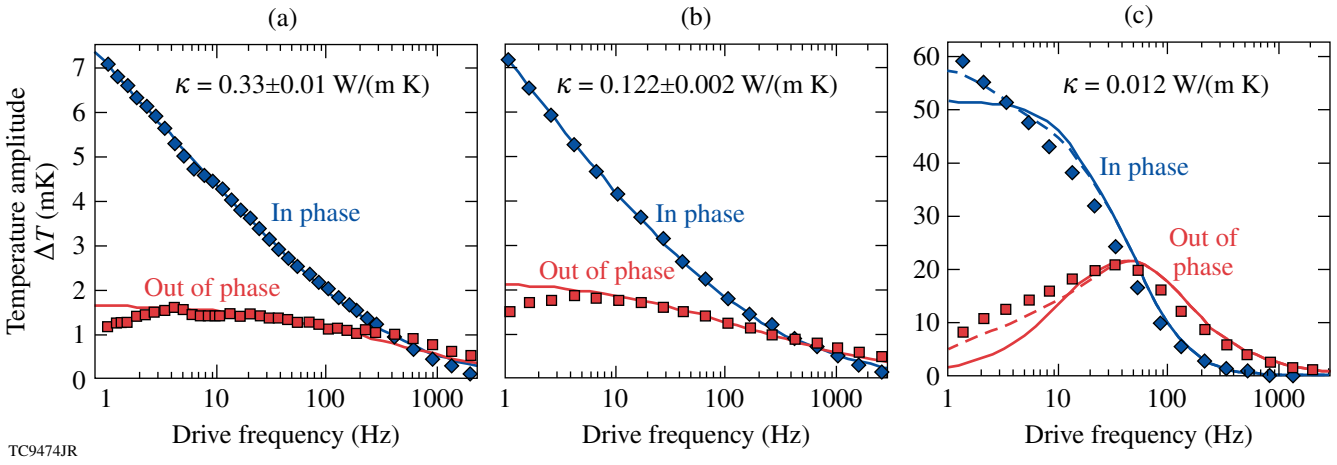

Figure 129.61
Measured (points) and calculated (lines) in-phase and out-of-phase temperature amplitudes of the wire as a function of drive frequency for (a) solid D_2 at 18.2 K with a power dissipation of 45 μW, (b) liquid D_2 at 26 K with a power dissipation of 10 μW, and (c) D_2 gas at 21 K with a pressure of 21 Torr and a power dissipation of 10 μW. (The negative of out-of-phase values is shown.) Fits were obtained by treating only the thermal conductivity κ as a variable. In (c) the fit is qualitative. The effect of choosing the distance to the simulation boundary to be 1 mm (solid lines) or 3 mm (dashed lines) is seen to be significant at low frequencies.

A summary of results for solid D_2 is shown in Fig. 129.62 (solid points). These include data taken for ortho D_2 and instances in which the growth direction of the solid was aligned either with the Pt wire or perpendicular to it. These data are fitted with a second-order polynomial $\kappa = (6.168 - 0.0635\,T + 0.0173\,T^2)$ W/(m K), where T is in units of K. No difference is seen among these data sets. This partially addresses a concern that directionality of crystal growth in the ICF fuel layer could affect the thermal conductivity across the layer and, therefore, the final profile of the layer. The data indicate that ortho-conversion would be an ineffective method, at temperatures between 14 K and the triple point, for altering the conductivity of a fuel layer. The data obtained here are consistent with the published data from Daney[14] and Gorodilov[29] (open symbols), but with the conductivities on average 5% larger than those of Daney. Some data are obtained at lower temperatures than is possible using Daney's method. At the lower temperatures shown in Fig. 129.62, increased thermal conductivity along with reduced resistance of the Pt wire results in lower voltages and the increasing importance of amplifier noise. At these lower temperatures, a longer time is required for the solid D_2 to recover from the stresses that result from shrinkage caused by temperature change. As a result, data are increasingly more difficult to obtain as the temperature is lowered.

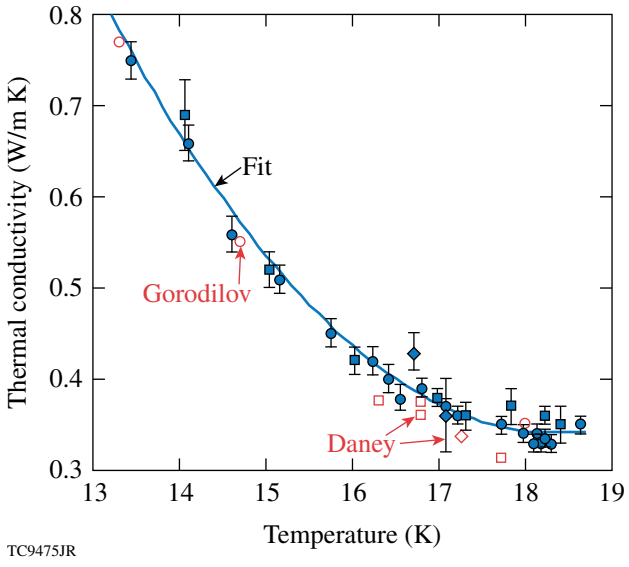

Figure 129.62
Measured values of thermal conductivity of solid D_2 as a function of temperature (solid blue data points). Solid circles are for normal D_2 with the wire parallel to the direction of ice growth. Solid squares (diamonds) are for ortho D_2 with the wire parallel (perpendicular) to the direction of ice growth. The curve is a second-order polynomial fit to the data. Shown for comparison are the data of Daney (open squares for normal D_2 and open diamonds for ortho D_2) and the data of Gorodilov (open circles).

Conclusions

The 3ω method has obtained accurate values of thermal conductivity for solid D_2 in a temperature range lower than any for which it has previously been used. The method operates on a small distance scale appropriate for ICF fuel layers and is somewhat less susceptible to concerns about thermal contraction and formation of cavities than conventional methods of measuring thermal conductivity. Values of thermal conductivity are slightly higher (5%) than those obtained by Daney. The results are all from "good" ice that is free of visible features like cracks and that shows large single crystals when viewed in polarized light. Normal D_2 and ortho D_2 show the same values of thermal conductivity over the temperature range examined. This confirms that ortho-conversion cannot be used at these temperatures as a tool for altering fuel-layer formation. No dependence of thermal conductivity on the direction of solid growth was detected.

ACKNOWLEDGMENT

This work was supported by the U.S. Department of Energy Office of Inertial Confinement Fusion under Cooperative Agreement No. DE-FC52-08NA28302, the University of Rochester, and the New York State Energy Research and Development Authority. The support of DOE does not constitute an endorsement by DOE of the views expressed in this article.

REFERENCES

1. D. R. Harding, D. D. Meyerhofer, S. J. Loucks, L. D. Lund, R. Janezic, L. M. Elasky, T. H. Hinterman, D. H. Edgell, W. Seka, M. D. Wittman, R. Q. Gram, D. Jacobs-Perkins, R. Early, T. Duffy, and M. J. Bonino, Phys. Plasmas **13**, 056316 (2006).
2. J. K. Hoffer and L. R. Foreman, Phys. Rev. Lett. **60**, 1310 (1988).
3. P. S. Ebey, J. M. Dole, D. A. Geller, J. K. Hoffer, J. Morris, A. Nobile, J. R. Schoonover, D. Wilson, M. Bonino, D. Harding, C. Sangster, W. Shmayda, A. Nikroo, J. D. Sheliak, J. Burmann, B. Cook, S. Letts, and J. Sanchez, Fusion Sci. Technol. **54**, 375 (2008); A. S. Bozek *et al.*, Fusion Eng. Des. **82**, 2171 (2007).
4. E. L. Alfonso, I. Anteby, and D. R. Harding, Fusion Technol. **38**, 149 (2000).
5. B. J. Kozioziemski *et al.*, Fusion Sci. Technol. **59**, 14 (2011).
6. B. J. Kozioziemski *et al.*, J. Appl. Phys. **105**, 093512 (2009).
7. D. G. Cahill, Rev. Sci. Instrum. **61**, 802 (1990); erratum **73**, 3701 (2002).
8. N. O. Birge and S. R. Nagel, Rev. Sci. Instrum. **58**, 1464 (1987).
9. F. Chen *et al.*, Rev. Sci. Instrum. **75**, 4578 (2004).
10. L. Lu, W. Yi, and D. L. Zhang, Rev. Sci. Instrum. **72**, 2996 (2001).
11. C. Dames and G. Chen, Rev. Sci. Instrum. **76**, 124902 (2005).

12. G. W. Collins *et al.*, Phys. Rev. B **41**, 1816 (1990).

13. P. C. Souers, *Hydrogen Properties for Fusion Energy* (University of California Press, Berkeley, CA, 1986), pp. 78–80.

14. D. E. Daney, Cryogenics **11**, 290 (1971); D. E. Daney, W. G. Steward, and R. O. Voth, National Bureau of Standards, Washington, DC, NBSIR 73-339 (October 1973).

15. T. Norimatsu *et al.*, J. Vac. Sci. Technol. A **6**, 3144 (1988).

16. D. E. Daney and E. Mapoles, Cryogenics **27**, 427 (1987).

17. Goodfellow Corporation, Berwyn, PA 19312-1780.

18. V. Arp, METALPAK™ software version 1.10, Horizon Technologies, Littleton, CO, 80128; using data from R. J. Corruccini and J. J. Gniewek, *Specific Heats and Enthalpies of Technical Solids at Low Temperatures*, National Bureau of Standards, Monograph 21 (U.S. Government Printing Office, Washington, DC, 1960).

19. Stanford Research Systems, Inc., Sunnyvale, CA 94089.

20. P. C. Souers, *Hydrogen Properties for Fusion Energy* (University of California Press, Berkeley, CA, 1986), p. 79.

21. *ibid.*, 68 and 96.

22. K. Clusius and E. Bartholomé, Z. Phys. Chem. Abt. B **30**, 237 (1935).

23. Sigma-Aldrich, St. Louis, MO 63178.

24. P. C. Souers, *Hydrogen Properties for Fusion Energy* (University of California Press, Berkeley, CA, 1986), pp. 315–316.

25. A. Jacquot *et al.*, J. Appl. Phys. **91**, 4733 (2002).

26. D. S. Kershaw, J. Comput. Phys. **26**, 43 (1978).

27. A. She, *2007 Summer Research Program for High School Juniors at the University of Rochester's Laboratory for Laser Energetics*, University of Rochester, Rochester, NY, LLE Report No. 353, LLE Document No. DOE/SF/19460-809 (2008).

28. National Instruments Corporation, Austin, TX 78759-3504.

29. B. Ya. Gorodilov *et al.*, Sov. J. Low Temp. Phys. **7**, 208 (1981).

Publications and Conference Presentations

Publications

S. H. Chen and S. K.-H. Wei, "Modification of the Stokes–Einstein Equation with a Semiempirical Microfriction Factor for Correlation of Tracer Diffusivities in Organic Solvents," Ind. Eng. Chem. Res. **50**, 12,304 (2011).

C. Dorrer, S. K.-H. Wei, P. Leung, M. Vargas, K. Wegman, J. Boulé, Z. Zhao, K. L. Marshall, and S. H. Chen, "High-Damage-Threshold Static Laser Beam Shaping Using Optically Patterned Liquid-Crystal Devices," Opt. Lett. **36**, 4035 (2011).

D. E. Fratanduono, J. H. Eggert, T. R. Boehly, M. A. Barrios, D. D. Meyerhofer, B. J. Jensen, and G. W. Collins, "Index of Refraction of Shock-Released Materials," J. Appl. Phys. **110**, 083509 (2011).

S. X. Hu, B. Militzer, V. N. Goncharov, and S. Skupsky, "First-Principles Equation-of-State Table of Deuterium for Inertial Confinement Fusion Applications," Phys. Rev. B **84**, 224109 (2011).

I. Íñiguez-de-la-Torre, S. Purohit, V. Kaushal, M. Margala, M. Gong, R. Sobolewski, D. Wolpert, P. Ampadu, T. González, and J. Mateos, "Exploring Digital Logic Design Using Ballistic Deflection Transistors Through Monte Carlo Simulations," IEEE Trans. Nanotech. **10**, 1337 (2011).

K. A. Marsh, C. E. Clayton, C. Joshi, W. Lu, W. B. Mori, A. Pak, L. O. Silva, N. Lemos, R. A. Fonseca, S. de Freitas Martins, F. Albert, T. Doeppner, C. Filip, D. Froula, S. H. Glenzer, D. Price, J. Ralph, and B. B. Pollock, "Laser Wakefield Accelerator Beyond 1 GeV Using Ionization Induced Injection," in the *Proceedings of the Particle Acceleration Conference* (IEEE, New York, 2011), pp. 707–711.

K. Mehrotra, H. P. Howard, S. D. Jacobs, and J. C. Lambropoulos, "Nanoindentation of High-Aspect Ratio Pillar Structures on Optical Multilayer Dielectric Diffraction Gratings," AIP Advances **1**, 042179 (2011).

B. B. Pollock, G. R. Tynan, F. Albert, C. Filip, S. H. Glenzer, J. Meinecke, A. Pak, J. E. Ralph, C. E. Clayton, C. Joshi, K. A. Marsh, J. Shaw, K. L. Herpoldt, and D. H. Froula, "The Effects of a Density Mismatch in a Two-Stage LWFA," in the *Proceedings of the Particle Acceleration Conference* (IEEE, New York, 2011), pp. 1421–1423.

L. Willingale, P. M. Nilson, A. G. R. Thomas, J. Cobble, R. S. Craxton, A. Maksimchuk, P. A. Norreys, T. C. Sangster, R. H. H. Scott, C. Stoeckl, C. Zulick, and K. Krushelnick, "Proton Probe Imaging of Fields Within a Laser-Generated Plasma Channel," IEEE Trans. Plasma Sci. **39**, 2616 (2011).

J.-H. Yang, R. S. Craxton, and M. G. Haines, "Explicit General Solutions to Relativistic Electron Dynamics in Plane-Wave Electromagnetic Fields and Simulations of Ponderomotive Acceleration," Plasma Phys. Control. Fusion **53**, 125006 (2011).

J. Zhang, A. Belousov, J. Karpiński, B. Batlogg, and R. Sobolewski, "Time-Resolved Femtosecond Optical Characterization of Multi-Photon Absorption in High-Pressure-Grown $Al_{0.86}Ga_{0.14}N$ Single Crystals," J. Appl. Phys. **110**, 113112 (2011).

Forthcoming Publications

J. Bromage, C. Dorrer, and R. K. Jungquist, "Temporal Contrast Degradation at the Focus of Ultrafast Pulses from High-Frequency Spectral Phase Modulation," to be published in the Journal of the Optical Society of America B.

D. H. Froula, I. V. Igumenshchev, D. T. Michel, D. H. Edgell, R. Follett, V. Yu. Glebov, V. N. Goncharov, J. Kwiatkowski, F. J. Marshall, P. B. Radha, W. Seka, C. Sorce, S. Stagnitto, C. Stoeckl, and T. C. Sangster, "Increasing Hydrodynamic Efficiency by Reducing Cross-Beam Energy Transfer in Direct-Drive Implosion Experiments," to be published in Physical Review Letters.

J. F. Myatt, J. Zhang, J. A. Delettrez, A. V. Maximov, R. W. Short, W. Seka, D. H. Edgell, D. F. DuBois, D. A. Russell, and H. X. Vu, "The Dynamics of Hot-Electron Heating in Direct-Drive Implosion Experiments Due to the Two-Plasmon-Decay Instability," to be published in Physics of Plasmas.

P. M. Nilson, J. R. Davies, W. Theobald, P. A. Jaanimagi, C. Mileham, R. Jungquist, C. Stoeckl, I. A. Begishev, A. A. Solodov, J. F. Myatt, J. D. Zuegel, T. C. Sangster, R. Betti, and D. D. Meyerhofer, "Time-Resolved Measurements of Hot-Electron Equilibration Dynamics in High-Intensity Laser Interactions with Thin-Foil Solid Targets," to be published in Physical Review Letters.

A. V. Okishev, C. Dorrer, Y. Fisher, and M. Pavia, "A Multiwavelength, Variable-Pulse-Width, Diode-Pumped Laser System," to be published in the Proceedings of SPIE.

A. Trajkovska-Petkoska and S. D. Jacobs, "The Manufacture, Characterization, and Manipulation of Polymer Cholesteric Liquid Crystal Flakes and Their Possible Applications," to be published in the Journal of Materials Science and Engineering.

A. Visco, M. J. Grosskopf, S. H. Glenzer, D. H. Froula, G. Gregori, T. Döppner, F. W. Doss, and R. P. Drake, Measurement of Radiative Shock Properties by X-Ray Thomson Scattering," to be published in Physical Review Letters.

S. K.-H. Wei, S. H. Chen, K. L. Marshall, C. Dorrer, and S. D. Jacobs, "Azimuthal Anchoring Energy and Pixel Resolution in a Photopatterned Liquid Crystal Cell Using Coumarin-Based Photoalignment Layers," to be published in the Japanese Journal of Applied Physics.

B. Yaakobi, P.-Y. Chang, A. A. Solodov, C. Stoeckl, D. H. Edgell, R. S. Craxton, S. X. Hu, J. F. Myatt, F. J. Marshall, W. Seka, and D. H. Froula, "Fast-Electron Generation in Long-Scale-Length Plasmas," to be published in Physics of Plasmas.

Conference Presentations

The following presentations were made at the 8th International Laser Operations Workshop, Aldermaston, U.K., 4–6 October 2011:

D. Canning, S. F. B. Morse, J. Qiao, T. Nguyen, B. E. Kruschwitz, and A. Kalb, "OMEGA EP Grating Compressor Chamber Operations."

B. E. Kruschwitz, M. D. Moore, and R. Jungquist, "OMEGA EP Focal-Spot Improvement Activities."

S. F. B. Morse, "A Polar-Drive-Irradiation Platform for NIF is Being Developed Using OMEGA."

J. Puth, "Omega Facility Status and Performance."

S. J. Stagnitto, J. Kwiatkowski, S. F. B. Morse, M. Labuzeta, and V. Guiliano, "Characterizing Debris-Shield Transmission Degradation and Estimating On-Target Energy."

G. Fiksel, A. Bhattacharjee, W. Fox, R. Betti, P.-Y. Chang, M. Hohenberger, and P. M. Nilson, "Studies of Magnetized and HED Plasmas—Recent Results and Future Plans," presented at the Center for Magnetized Self-Organization Meeting, Durham, NH, 17–20 October 2011.

S. Friedrich, T. J. Clancy, M. J. Eckart, M. J. Shoup III, T. Buczek, and V. Yu. Glebov, "High-Speed Diamond Detectors for Fast-Neutron Analysis of Inertial Confinement Fusion," presented at the IEEE Nuclear Science Symposium, Valencia, Spain, 23–29 October 2011.

J. H. Kelly, "The Optics of Inertial Confinement Fusion," presented at The Institute of Optics Colloquium, Rochester, NY, 31 October 2011.

J. Bromage, C. Dorrer, M. Millecchia, J. Bunkenburg, R. K. Jungquist, and J. D. Zuegel, "A Front End for Ultra-Intense OPCPA," presented at Light at Extreme Intensities, Szeged, Hungary, 14–18 November 2011.

The following presentations were made at the 53rd Annual Meeting of the APS Division of Plasma Physics, Salt Lake City, UT, 14–18 November 2011:

K. S. Anderson, R. Betti, P. W. McKenty, T. J. B. Collins, R. S. Craxton, J. A. Marozas, R. Nora, S. Skupsky, and L. J. Perkins, "Simulations of Shock-Ignition Targets for the NIF."

T. R. Boehly, V. N. Goncharov, W. Seka, S. X. Hu, J. A. Marozas, D. D. Meyerhofer, P. M. Celliers, D. G. Hicks, M. A. Barrios, D. E. Fratanduono, G. W. Collins, "Multiple Spherically Converging Shock Waves in Liquid Deuterium."

P.-Y. Chang, G. Fiksel, M. Hohenberger, J. P. Knauer, R. Betti, F. H. Séguin, C. K. Li, M. E. Manuel, and R. D. Petrasso, "Experiments and Simulations of Laser-Driven Magnetized ICF Targets on OMEGA."

T. J. B. Collins, J. A. Marozas, K. S. Anderson, R. Betti, R. S. Craxton, J. A. Delettrez, V. N. Goncharov, D. R. Harding, F. J. Marshall, R. L. McCrory, D. D. Meyerhofer, P. W. McKenty, P. B. Radha, A. Shvydky, S. Skupsky, J. D. Zuegel, "A Polar-Drive–Ignition Design for the National Ignition Facility" (invited).

R. S. Craxton, P. W. McKenty, E. J. Bond, S. Le Pape, A. J. MacKinnon, P. A. Michel, and J. D. Moody, "Three-Dimensional Distributions of Scattered Light in NIF 'Exploding-Pusher' Polar-Drive Experiments."

J. A. Delettrez, W. Seka, D. H. Froula, and T. J. B. Collins, "Three-Dimensional Numerical Investigation of Oblique Laser Irradiation of Planar Targets."

D. H. Edgell, J. Magoon, T. C. Sangster, M. J. Shoup III, F. J. Marshall, C. Stoeckl, V. Yu. Glebov, A. MacPhee, G. Krauter, S. Burns, J. Celeste, M. J. Eckart, J. R. Kimbrough, J. D. Kilkenny, G. Lacaille, N. B. Meezan, J. Parker, Z. Sober, and M. Thayne, "First Results from the South Pole Bang Time (SPBT) Diagnostic on the NIF."

R. Epstein, S. P. Regan, F. J. Marshall, T. C. Sangster, S. W. Hamlin, R. L. McCrory, D. D. Meyerhofer, B. A. Hammel, L. J. Suter, H. Scott, M. A. Barrios, D. A. Callahan, N. Izumi, N. B. Meezan, I. E. Golovkin, J. J. MacFarlane, R. C. Mancini, and K. J. Peterson, "Analysis of Diagnostic X-Ray Spectra of Implosions at the National Ignition Facility."

G. Fiksel, P.-Y. Chang, M. Hohenberger, J. P. Knauer, F. J. Marshall, D. D. Meyerhofer, R. Betti, F. H. Séguin, and R. D. Petrasso, "Fusion-Yield Enhancement in Magnetized Laser-Driven Implosions."

C. J. Forrest, V. Yu. Glebov, V. N. Goncharov, J. P. Knauer, D. D. Meyerhofer, P. B. Radha, T. C. Sangster, and C. Stoeckl, "Measurement of the Areal Density (ρR) Using nT Elastic Backscattering on OMEGA."

D. E. Fratanduono, M. A. Barrios, T. R. Boehly, D. D. Meyerhofer, J. H. Eggert, D. G. Hicks, R. F. Smith, D. Braun, P. M. Celliers, and G. W. Collins, "Refractive Index of Lithium Fluoride Ramp Compressed to 800 GPa" (invited).

D. H. Froula, I. V. Igumenshchev, D. T. Michel, C. Sorce, R. Follett, D. H. Edgell, W. Seka, and V. N. Goncharov, "Measurements of an Increased Neutron Yield with Reduced CBET."

L. Gao, P. M. Nilson, I. V. Igumenshchev, S. X. Hu, C. Stoeckl, D. H. Froula, and D. D. Meyerhofer, "Magnetic-Field Generation in Planar Plastic Targets on OMEGA EP."

V. Yu. Glebov, C. Stoeckl, T. C. Sangster, C. Forrest, J. P. Knauer, V. N. Goncharov, and P. B. Radha, "Measurements of DD Neutron Yield and Ion Temperature in DT Implosions on OMEGA."

V. N. Goncharov, T. C. Sangster, R. Epstein, S. X. Hu, I. V. Igumenshchev, D. H. Froula, R. L. McCrory, D. D. Meyerhofer, P. B. Radha, W. Seka, S. Skupsky, and C. Stoeckl, "Cryogenic Deuterium–Tritium Implosions on OMEGA."

M. Hohenberger, P.-Y. Chang, G. Fiksel, J. P. Knauer, D. D. Meyerhofer, R. Betti, F. J. Marshall, F. H. Séguin, and R. D. Petrasso, "Inertial Confinement Fusion Implosions with Seeded Magnetic Fields on OMEGA" (invited).

S. X. Hu, G. Fiksel, V. N. Goncharov, S. Skupsky, and V. A. Smalyuk, "Analysis of Laser-Imprinting Reduction in Spherical-RT Experiments with Si-/Ge-Doped Plastic Targets."

I. V. Igumenshchev, W. Seka, D. H. Edgell, D. H. Froula, V. N. Goncharov, R. S. Craxton, L. Divol, R. Follett, J. H. Kelly, T. Z. Kosc, D. T. Michel, P. Michel, R. L. McCrory, A. V. Maximov, D. D. Meyerhofer, J. F. Myatt, T. C. Sangster, A. Shvydky, S. Skupsky, and C. Stoeckl, "Crossed-Beam Energy Transfer in Direct-Drive Implosions" (invited).

S. Ivancic, W. Theobald, C. Stoeckl, P. M. Nilson, T. C. Sangster, D. D. Meyerhofer, S. X. Hu, and L. Willingale, "Initial Channeling of a Kilojoule-Class Laser in Long-Scale-Length Plasmas."

J. P. Knauer, V. Yu. Glebov, D. D. Meyerhofer, T. C. Sangster, C. Stoeckl, E. J. Bond, J. A. Caggiano, T. J. Clancy, M. J. Eckart, S. Friedrich, R. Hatarik, R. A. Lerche, A. J. Mackinnon, J. M. McNaney, M. J. Moran, D. H. Munro, S. J. Padalino, and J. D. Kilkenny, "Neutron Spectra Measured with Time-of-Flight Detectors on the National Ignition Facility."

J. A. Marozas, T. J. B. Collins, D. H. Edgell, I. V. Igumenshchev, and J. F. Myatt, "Two-Dimensional Analysis of Crossed-Beam Energy Transfer (CBET) in Direct-Drive ICF Target Implosions."

F. J. Marshall, P. B. Radha, R. Epstein, V. Yu. Glebov, J. A. Frenje, C. K. Li, R. D. Petrasso, and F. H. Séguin, "High-Convergence-Ratio Polar-Drive Experiments on OMEGA."

A. V. Maximov, J. F. Myatt, R. W. Short, I. V. Igumenshchev, D. H. Edgell, and W. Seka, "Energy Transfer Between Crossing Laser Beams in the Plasmas of Direct-Drive ICF."

P. W. McKenty, R. S. Craxton, F. J. Marshall, A. Shvydky, R. Epstein, A. M. Cok, J. A. Marozas, T. J. B. Collins, S. Skupsky, C. Stoeckl, T. C. Sangster, M. J. Bonino, R. Janezic, D. R. Harding, W. T. Shmayda, S. F. B. Morse, D. D. Meyerhofer, and R. L. McCrory, "Numerical Evaluation of Subtangential Focusing in OMEGA Target Implosions."

D. D. Meyerhofer, S.-W. Bahk, J. Bromage, C. Dorrer, J. H. Kelly, B. E. Kruschwitz, S. J. Loucks, R. L. McCrory, S. F. B. Morse, J. Qiao, C. Stoeckl, L. J. Waxer, and J. D. Zuegel, "Status of the OMEGA EP Laser System."

D. T. Michel, B. Yaakobi, S. X. Hu, R. W. Short, J. F. Myatt, C. Stoeckl, D. H. Edgell, W. Seka, V. N. Goncharov, and D. H. Froula, "Measurements of Hot Electrons Produced by Two-Plasmon Decay in Near Direct-Drive–Ignition Plasma Conditions."

J. F. Myatt, J. Zhang, A. V. Maximov, R. W. Short, D. F. DuBois, D. A. Russell, and H. X. Vu, "A Self-Consistent Quasilinear Model for the Two-Plasmon-Decay Instability in Inhomogeneous Plasmas."

R. Nora, R. Betti, K. S. Anderson, W. Theobald, A. Casner, M. Lafon, X. Ribeyre, and G. Schurtz, "Cryogenic Shock-Ignition Target Designs for OMEGA."

P. B. Radha, F. J. Marshall, T. R. Boehly, T. J. B. Collins, R. S. Craxton, R. Epstein, V. N. Goncharov, J. A. Marozas, R. L. McCrory, D. D. Meyerhofer, A. Shvydky, S. Skupsky, J. A. Frenje, and R. D. Petrasso, "Polar-Drive Designs for OMEGA."

S. P. Regan, R. Epstein, B. A. Hammel, L. J. Suter, J. Ralph, H. Scott, M. A. Barrios, D. K. Bradley, D. A. Callahan, C. J. Cerjan, G. W. Collins, S. N. Dixit, T. Doeppner, M. J. Edwards, D. R. Farley, S. Glenn, S. H. Glenzer, I. E. Golovkin, S. W. Haan, A. Hamza, D. G. Hicks, N. Izumi, J. D. Kilkenny, J. L. Kline, G. A. Kyrala, O. L. Landen, T. Ma, J. J. MacFarlane, R. C. Mancini, R. L. McCrory, N. B. Meezan, D. D. Meyerhofer, A. Nikroo, K. J. Peterson, T. C. Sangster, P. Springer, and R. P. J. Town, "Hot-Spot Mix in Ignition-Scale Implosions at the National Ignition Facility" (invited).

T. C. Sangster, W. T. Shmayda, V. Versteeg, D. R. Harding, R. Janezic, V. N. Goncharov, D. H. Edgell, D. H. Froula, V. Yu. Glebov, S. X. Hu, F. J. Marshall, R. L. McCrory, P. W. McKenty, D. D. Meyerhofer, J. F. Myatt, P. B. Radha, W. Seka, C. Stoeckl, B. Yaakobi, J. A. Frenje, M. Gatu-Johnson, and R. D. Petrasso, "Cryogenic-DT-Implosion Performance with Improved Target-Surface Quality."

W. Seka, I. V. Igumenshchev, D. H. Froula, D. H. Edgell, J. F. Myatt, R. W. Short, V. N. Goncharov, and A. V. Maximov, "Absorption by the Two-Plasmon-Decay Instability in Direct-Drive Implosions."

R. W. Short and J. F. Myatt, "Convective Multibeam Two-Plasmon Decay for Spherical and Planar Irradiation Geometries."

A. Shvydky, P. W. McKenty, M. Hohenberger, G. Fiksel, T. J. B. Collins, J. A. Marozas, J. D. Zuegel, and T. C. Sangster, "Preparing for OMEGA EP Validation of 1-D Multi-FM SSD for the NIF."

A. A. Solodov, K. S. Anderson, A. Shvydky, W. Theobald, R. Betti, J. F. Myatt, and C. Stoeckl, "Simulations of Implosion Core Heating for Integrated Cone-in-Shell Fast-Ignition Experiments on OMEGA."

A. Sorokovikova, M. S. Wei, R. B. Stephens, J. Jaquez, R. Nishra, H. Sawada, W. Theobald, P. Patel, H. McLean, Y. Sentoku, and F. N. Beg, "Study of Dependence of Fast Electron Transport on Target Material Using the 10 ps, 1.5 kJ Omega EP Laser."

C. Stoeckl, P. B. Radha, R. E. Bahr, J. A. Delettrez, D. H. Edgell, V. Yu. Glebov, V. N. Goncharov, I. V. Igumenshchev, T. C. Sangster, W. Seka, J. A. Frenje, and R. D. Petrasso, "Preheat Studies Using Low-Adiabat Plastic-Shell Implosions with Triple-Picket Pulses on OMEGA."

W. Theobald, M. Hohenberger, S. X. Hu, K. S. Anderson, R. Betti, T. R. Boehly, A. Casner, D. H. Edgell, D. E. Fratanduono, M. Lafon, D. D. Meyerhofer, R. Nora, X. Ribeyre, T. C. Sangster, G. Schurtz, W. Seka, C. Stoeckl, B. Yaakobi, "High-Intensity Shock-Ignition Experiments in Planar Geometry."

R. Yan, A. V. Maximov, C. Ren, and F. S. Tsung, "Energetic-Electron Generation in Two-Plasmon-Decay Instabilities in Inertial Confinement Fusion."

The following presentations were made at the International Collaboration on High Energy Density Science Workshop, Kanazawa, Japan, 25–29 November 2011:

T. R. Boehly, D. E. Fratanduono, M. A. Barrios, D. D. Meyerhofer, J. H. Eggert, D. G. Hicks, R. F. Smith, D. Braun, P. M. Celliers, and G. W. Collins, "Refractive-Index Measurements of LiF Ramp Compressed to 800 GPa."

T. R. Boehly, V. N. Goncharov, W. Seka, S. X. Hu, J. A. Marozas, D. D. Meyerhofer, P. M. Celliers, D. G. Hicks, M. A. Barrios, D. E. Fratanduono, and G. W. Collins, "Radiative Precursors and Temperature Measurements in Shock Deuterium."


1850
MELIORA
UNIVERSITY of
ROCHESTER